ICMRM 2019

15th International Conference on Magnetic Resonance Microscopy

CONFERENCE PROGRAMME

August 18 – 22, PARIS

Institut du Cerveau et de la Moelle Epinière

SPONSORS AND EXHIBITORS

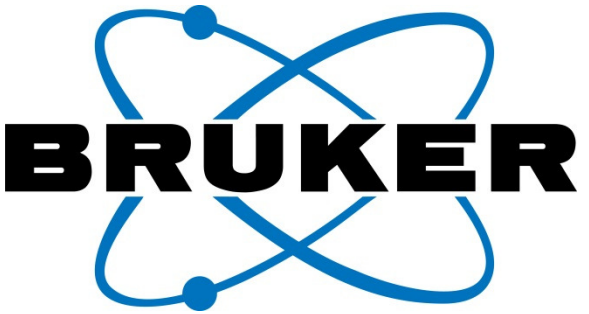

TABLE OF CONTENT

WELCOME LETTER	4
COMMITTEES	5
CONFERENCE VENUE	6
PROGRAMME OVERVIEW	8
DETAILED PROGRAMME	10
ABSTRACTS OF ORAL PRESENTATIONS	18
LIST OF POSTERS	мл6
LIST OF PARTICIPANTS	мм6

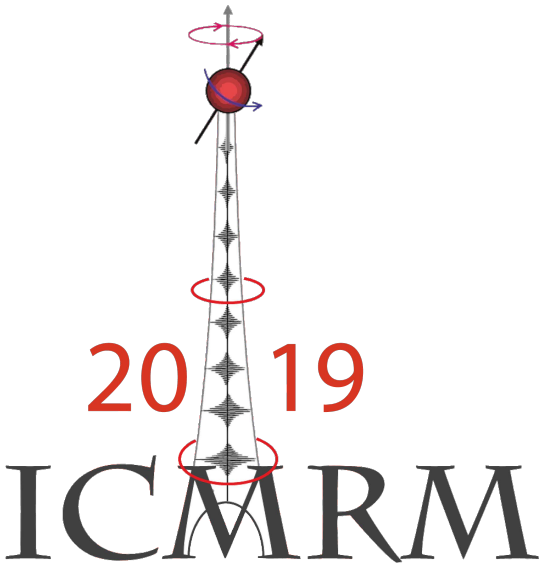

https://icmrm2019.sciencesconf.org

WELCOME LETTER

Dear colleagues,

On behalf of the Local Organizing Committee we are delighted to welcome you to the 15th International Conference on Magnetic Resonance Microscopy (ICMRM) in Paris, France. ICMRM is held under the auspices of the Spatially Resolved Magnetic Resonance (SRMRM) Division of the AMPERE (Atomes et Molécules Par Etude Radio - électrique) Society and started in 1991 in Heidelberg, Germany. For the first time this conference is held in France this year.

We are fortunate to assemble an outstanding and diverse speaker panel, which includes experts in the field. Continuing the successful tradition of past ICMRMs, in 2019, the conference will start with a half-day session of educational lectures. We feel very privileged to have extraordinary scientists such as D. Budker (Helmholtz Institute, Germany), N. Kolmosh (NIH, USA), B. Newling (U. of New Brunswick, Canada), L. Wald (Harvard MGH, USA) offer their time and expertise for the benefit of the younger researchers in the field.

Dr. David Hoult, whose pioneering contributions in MRI technology are well renowned, will give the opening talk of the conference. We are certain that it will provide a source of inspiration for all participants. We have also two additional special lectures: the Erwin Hahn lecture given by Bernhard Blumich and the Stimulated Hahn lecture provided by Eiichi Fukushima. Both Bernhard and Eiichi have made seminal contributions to this field and have been faithful attendees of ICMRM over the years.

As in previous conferences, we have scheduled the Paul Callaghan Young Investigator Competition, aimed to reward outstanding PhD thesis works. Six finalists have been chosen to present their projects. The winner will be announced during the banquet dinner while cruising the Seine river, and will receive the “Sir Paul Callaghan Young Investigator Award”.

We thank all of you for submitting numerous high quality abstracts. With the help of the members of the Scientific Committee we believe that a remarkable scientific program was put together.

We would also like to thank our sponsors. Without their generosity, ICMRM could not exist. Please take moment to visit their stands and look over the material they provided.
We are delighted and honored to host the ICMRM in 2019 in Paris. Paris is the city of love, inspiration, art and fashion. Its nickname “the City of Light” reminds of its importance as a center for education and intellectual pursuits. We hope that our conference will add a few more photons to the light of the city and will offer you all unforgettable magnetic moments.

Thank you for joining us for the 15th ICMRM!

Luisa Ciobanu & Dimitrios Sakellariou

COMMITTEES

Committees of the Division of Spatially Resolved Magnetic Resonance of the Groupement AMPERE

ICMRM 2019 Conference Chairs:

Luisa Ciobanu CEA-Saclay
Dimitrios Sakellariou KU Leuven

ICMRM Local Organizing Committee:

Patrick Berthault, Celine Boutin CEA/CNRS-Saclay
Solène Bardin, Luisa Ciobanu, Gabrielle Fournet CEA-Saclay
Alexandra Petiet ICM - Paris
Vincent Sarou-Kanian CNRS - Orleans

Executive Committee:

Chair: Melanie Britton
Vice Chair: Daniel Topgaard
Treasurer: Andy Sederman
Secretary General: Sarah Codd
Vice Secretary General: Volker Behr
Conference co-Chairs: Luisa Ciobanu & Dimitrios Sakellariou
Past Conference co-Chairs: Bruce Balcom & Stephen Beyea
Past Chair: Mike Johns (Past Chair)
Advisors: Eiichi Fukushima, Bernhard Blümich, Lizhi Xiao, Igor Koptyug, Henk Van As

Division Committee:

Tomoyuki Haishi, Yasuhiko Terada, Yang Xia, Petrik Galvosas, Nikolaus Nestle, Daniel Alexander, Thomas Meersman, Peter Blümler, Dean Kuethe, Igor Mastikhin, Matthias Appel, Carel Windt, Warren Warren, Jeffrey Reimer, Lawrence Wald, Dieter Gross, Alexej Jerschow, Kazuyuki Takeda, Galina Pavlovskaya, Uri Nevo, Joseph Seymour, Ben Newling, Meghan Halse, Gisela Guthausen, Robin Dykstra, Miki Komlosh, Louis Bouchard, Bernard Siow, Katsumi Kose, Andreas Pohlmeier

Scientific Committee: The Scientific Committee includes all members of the Executive Committee and the Division Committee.

GROUPE HOSPITALIER UNIVERSITAIRE
LA PITIÉ SALPÊTRIÈRE - CHARLES FOIX

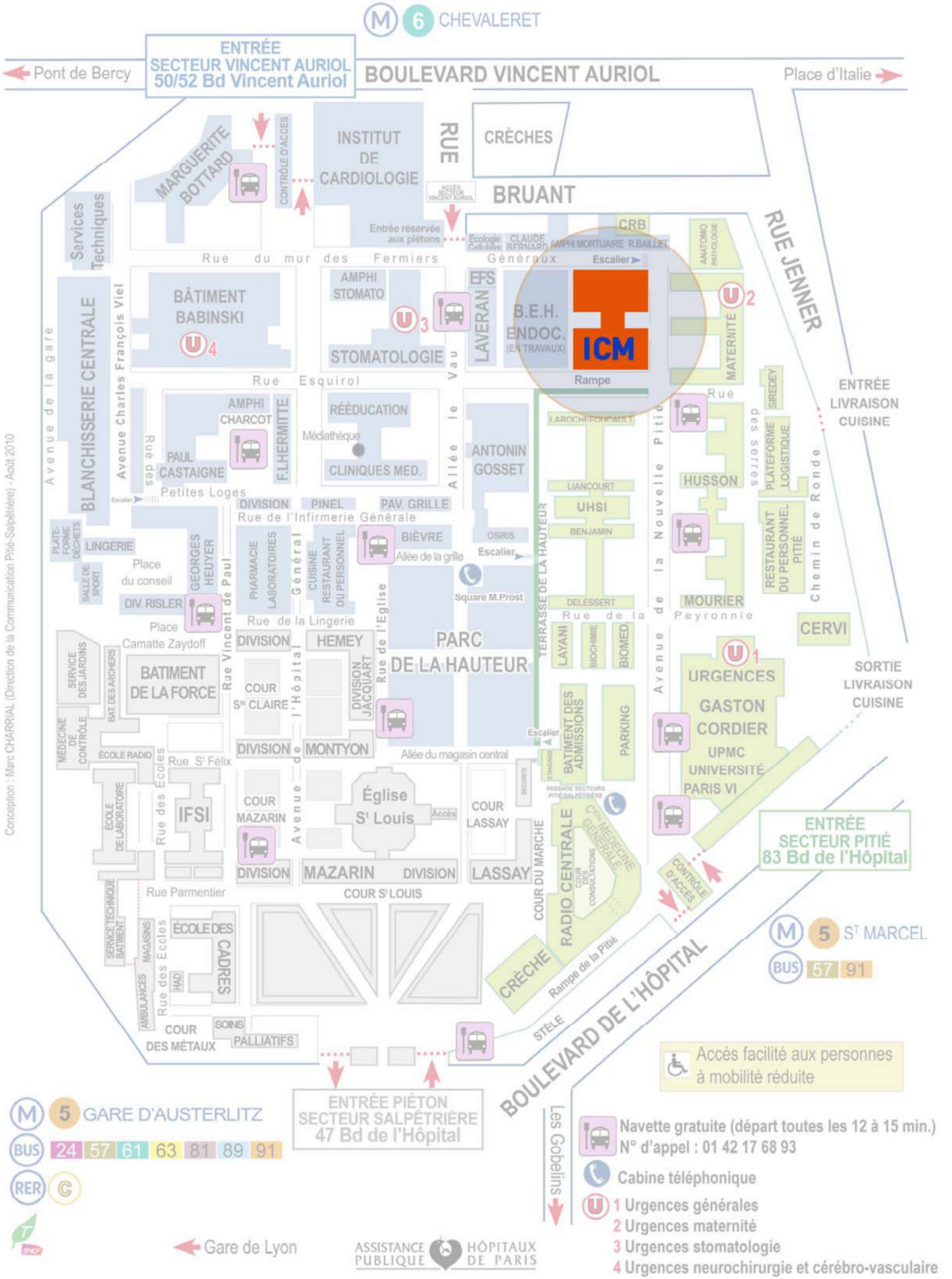

PROGRAMME OVERVIEW

	Sun. 18	Mon. 19	Tue. 20	Wed. 21	Thu. 22
8h45		Opening	Hardware	Erwin Hahn Lecture: Echoes: A Circle From the Past to the Future	Engineering & Materials
9h00	Arrivals and registration	MR Microscopy		Paul Callaghan Young Investigator Competition	
10h00		Coffee break	Coffee break	Coffee break	Coffee break
11h00		Mobile & Low Field	Biomedical	Paul Callaghan Young Investigator Competition	Flow & diffusion
12h00				Stimulated Hahn Talk: Pre Silicon-age NMR: a Look Back in Time	
13h00	Educational 1: MRI Hardware	Lunch	Lunch	Lunch	Lunch
14h00	Educational 2: Zero- and Ultra-Low Field NMR	Porous media	Hyperpolarization	Free afternoon or visit to NeuroSpin	General Meeting
15h00	Coffee break		Cellular & Molecular		Electrochemical
16h00	Educational 3: Relaxometry in Porous Media	Coffee break + Posters A	Coffee break + Posters B		Closing
17h00	Educational 4: Flow & Diffusion				
	Break				
18h00	Plenary Lecture: Abragam to Zeugmatography: A Physicist's Fascination with Fields				
	Break				
19h00	Opening reception			Banquet - Bateaux parisiens	
night					

DETAILED PROGRAMME

SUNDAY 18TH	
10h30	Arrivals and registrations
13h00	Educational 1: MRI Hardware - *Lawrence Wald*
14h00	Educational 2: Zero- and Ultra- Low Field NMR - *Dmitry Budker*
15h00	Break
15h30	Educational 3: Relaxometry in Porous Media - *Ben Newling*
16h30	Educational 4: Flow & Diffusion - *Miki Komlosh*
17h30	Break
17h45	Plenary Lecture: Abragam to Zeugmatography: A Physicist's Fascination with Fields - *David Hoult*
18h45	Break
19h00	Opening reception

MONDAY 19TH	
8h45	Opening
MR Microscopy - *Chair: Luisa Ciobanu*	
9h00	Magnetic Resonance Microscopy Provides Multiple Biomarkers in Animal Models of Neurological Diseases - *Alexandra Badea, Duke University Medical Center*
9h30	Suppressing chemical-shift artefacts in rheo-microMRI measurements of dense oil -in- water emulsions - *Maria Raquel Serial, Wageningen University and Research*
9h45	Identification of Optimal Sampling Patterns for Compressed Sensing RARE MRI in Porous Media - *Kaspars Karlsons, Magnetic Resonance Research Centre, Department of Chemical Engineering and Biotechnology, University of Cambridge*
10h00	Compensating Diffusion Bias of Quantitative T2 on High-Field MRI Scanners - *Natalie Bnaiahu, Department of Biomedical Engineering*
10h15	Selective excitation with colored Frank sequences - *Markus Küppers, ITMC, RWTH Aachen University*
10h30	Splitting one dimension into four: progressing from diffusion distributions into diffusion tensor distributions - *João Pedro de Almeida Martins, Lund University*
10h45	Coffee Break

Mobile & Low Field – *Chair: Dimitrios Sakellariou*	
11h15	The Recent Development of a Low-field Permanent-magnet-based MRI Head Imager - *Shaoying Huang, Singapore university of technology and design, Singapore University of Technology and Design*
11h45	CPMG with Time-Dependent Fields: Observation of Adiabatic and Non-Adiabatic Behavior - *Martin Hürlimann, Schlumberger-Doll Research*
12h00	Matrix Pencil Method for High Resolution Data Processing in Low-Field NMR - *Sophia Fricke, University of California*
12h15	Imaging sorghum roots in natural soil - *Dean Kuethe, ABQMR*
12h30	Multi-coils Design of Downhole NMR Azimuthal Imaging Probe - *Sihui Luo, China University of Petroleum-Beijing*
12h45	Multi-phase flow measurement using an Earth's field NMR flow meter - *Michael Johns, University of Western Australia*
13h00	Lunch
Porous Media – *Chair: Bruce Balcom*	
14h00	Porous Media and Rethinking Assumptions - *Kate Washburn, Nofima*
14h30	Probing pore connectivity of rock cores by PcT2 correlation spectroscopy - *Ray Tang, Schlumberger-Doll Research*
14h45	Unsteady State Relative Permeability Curves Derived from Saturation Data Spatially and Temporally Resolved Using Magnetic Resonance Imaging - *Mohammad Sadegh Zamiri, University of New Brunswick*
15h00	Investigating liquid displacement in porous media using spatially resolved NMR spectroscopy - *John Georg Seland, The University of Bergen*
15h15	Probing the adsorption in microporous materials by hyphenated NMR and physorption - *Rodrigo de Oliveira-Silva, Centre for Membrane Separations, Adsorption, Catalysis and Spectroscopy for Sustainable Solutions*
15h30	Mapping pore-scale flow heterogeneity in rock with 3D spatially-resolved propagators acquired using compressed-sensing APGSTE-RARE MRI - *Daan de Kort, University of Cambridge*
15h45	Pore Size from Multimodal Features of Relaxation Times - *Armin Afrough, MRI Centre, University of New Brunswick*
16h00	**Coffee Break and Poster Session A**

Tuesday 20TH	
Hardware – *Chair: Eiichi Fukushima*	
8h45	The Iseult 11.75T Whole-body MRI magnet - *Lionel Quettier, Institut de Recherches sur les lois Fondamentales de l'Univers*
9h15	MRI at 2.15 MHz in a large-bore Halbach Array - *Thomas O'Reilly, Leiden University Medical Center*
9h30	Parallel-Plate Resonator for MRI studies of lithium ion batteries. - *Andrés Ramírez Aguilera, MRI Centre, Department of Physics, University of New Brunswick, Centro de Biofísica Médica, Universidad de Oriente*
9h45	Continuously Adjustable Passive Shims - *Andrew McDowell, NuevoMR, LLC*
10h00	Magnetic Particle Imaging using Toroidal Vortex Rotation of Halbach Rings - *Patrick Vogel, Experimental Physics 5 (Biophysics), University of Würzburg*
10h15	NMR with a fast-moving coil array - *Yi-Qiao Song, Schlumberger-Doll Research*
10h30	Coffee Break
Biomedical – *Chair: Alexandra Petiet*	
11h00	Mapping hydration water structure and dynamics by Overhauser DNP relaxometry - *Song-I Han, University of California, Santa Barbara*
11h30	Metabolic assessment of stroked rats using $^{17}O_2$ gas - *Victor Rodin, Glasgow Experimental MRI Centre, Institute of Neuroscience and Psychology, College of Medicine, Veterinary and Life Sciences, University of Glasgow*
11h45	Creation of a hemodynamic response function for BOLD fMRI in the rat brain - *Henriette Lambers, University Hospital Münster*
12h00	Diffusion correlation imaging (DCI) reveals microscopic anisotropy following traumatic brain injury - *Dan Benjamini, Eunice Kennedy Shriver National Institute of Child Health and Human Development, Center for Neuroscience and Regenerative Medicine*
12h15	Metabolic rates in red blood cells under shear studied by Rheo-NMR - *Petrik Galvosas, Victoria University of Wellington*
12h30	Quantitative Mapping of Fatty Acid Composition using Free-Breathing Spectroscopic Imaging with Compressed Sensing - *Steven Beyea, Dalhousie University, Biomedical Translational Imaging Centre (BIOTIC)*
12h45	Lunch
Hyperpolarization – *Chair: Patrick Berthault*	
13h45	Progress towards molecular-MRI with Signal Amplification by

	Reversible Exchange (SABRE) Hyperpolarisation - *Simon Duckett, University of York*
14h15	Hyperpolarized parahydrogen based MRI: SLIC-SABRE and catalytic reactors imaging - *Alexandra Svyatova, International Tomography Center SB RAS, Novosibirsk State University*
14h30	GammaMRI: towards high-resolution single photon imaging using highly-polarized gamma-emitting nuclei - *Karolina Kulesz, CERN, Experimental Physics Department, Geneva, Switzerland*
Cellular & Molecular – *Chair: Patrick Berthault*	
14h45	Real-time in vivo MRI tracking of single cells and nanoparticles - *Cornelius Faber, Clinical Radiology, University Hospital Münster*
15h15	A Novel MRI Technique for Quantifying Myelin in Mice Brain White Matter - *Ella Wilczynski, Department of Biomedical Engineering*
15h30	Metabolic specificity analysis of CEST techniques at high and ultra-high magnetic fields - *Julia Krug, Laboratory of BioNanoTechnology, Wageningen University & Research, Laboratory of Biophysics, Wageningen University & Research*
15h45	Probing displacements within and exchange among tissue microenvironments using static gradient spin echo diffusion and DEXSY NMR - *Nathan Williamson, Eunice Kennedy Shriver National Institute of Child Health and Human Development*
16h00	**Coffee Break and Poster Session B**

Wednesday 21TH	
8h45	Erwin Hahn Lecture: Echoes: A Circle From the Past to the Future - *Bernhard Blümich*
Paul Callaghan Young Investigator Competition – *Chair: Melanie Britton*	
9h30	Para-Hydrogen Induced Polarization – Production of highly concentrated metabolite precursors and long polarization storage over 10s of minutes - *Stefan Glöggler, Max Planck Institute for Biophysical Chemistry*
9h55	Ferroelectric Composite Ceramic Probe for MRM - *Marine Moussu, Multiwave Innovation, Institut FRESNEL*
10h20	NMR Relaxation Measurements of Solid-Solid Phase Transitions in Complex Lipid Systems - *Madison Nelson, Montana State University*
10h45	Coffee Break
11h15	Real-time imaging of granular dynamics - *Alexander Penn, Institute of*

	Biomedical Engineering, ETH Zurich and University of Zurich, Department of Mechanical and Process Engineering, ETH Zurich
11h40	MRI of the Interplay between Fluid Dynamics and Heat Transfer - *Matt Skuntz, Montana State University*
12h05	SPatiotemporal ENcoding (SPEN) 3D Diffusion Tensor Imaging of in vivo mouse brain at ultra-high fields and ≤ 100µm isotropic resolutions - *Maxime Yon, Weizmann Institute of Science*
12h30	Stimulated Hahn Talk: Pre Silicon-age NMR: a Look Back in Time - Eiichi Fukushima
13h15	Lunch
14h00	Free afternoon or visit to NeuroSpin
19h30	Banquet - Bateaux Parisiens

Thursday 22TH	
Engineering & Materials – *Chair: Vincent Sarou-Kanian*	
8h45	LAOS Rheo-NMR - *Joseph Seymour, Chemical and Biological Engineering, Montana State University*
9h15	Fast ultrafiltration characterization by compressed sensing MRI - *Sebastian Schuhmann, Institute of Mechanical Process Engineering and Mechanics, KIT*
9h30	Opencage: RF coil with an adjusted current distribution - *Anton Nikulin, Institut Langevin, ESPCI Paris, CNRS, PSL University*
9h45	Rheological NMR to study polymer dynamics and protein aggregation - *Ulrich Scheler, Leibniz Institute for Polymer Research*
10h00	Magnetic resonance imaging to assess transport properties of porous media due to dissolution and precipitation processes - *Andreas Pohlmeier, Research Center Jülich*
10h15	Development of a versatile fluidic 3D printed device for NMR and MRI studies: application on hyperpolarized xenon studies - *Guillaume Carret, CortecNet*
10h30	T_1-T_2* Relaxation Correlation - *Speciation in Solid-like Materials - Bruce Balcom, University of New Brunswick*
10h45	Coffee Break
Flow & diffusion – *Chair: Sarah Codd*	
11h15	Magnetic resonance methods for studying reactions in trickle bed reactors at operando conditions - *Andy Sederman, Magnetic Resonance Research Centre, Department of Chemical Engineering and Biotechnology, University of Cambridge*
11h45	Measuring the velocity of gas and particles in and around a single

	bubble in a 3D fluidised bed - *Nick Rice, Magnetic Resonance Research Centre, Department of Chemical Engineering and Biotechnology, University of Cambridge*
12h00	Impact of Fluctuation Induced Asymmetric Propagators on the Accuracy of Phase Contrast Velocimetry - *William Holmes, University of Glasgow*
12h15	Localization regime in diffusion MRI: theory and experiments - *Denis Grebenkov, Laboratory of Condensed Matter Physics, CNRS*
12h30	Phase error correction to velocity-encoded single-point-imaging measurements using a sawtooth gradient waveform - *Ben Newling, University of New Brunswick*
12h45	Intact Plant MRI: up and down during 40 years - *Henk Van As, Lab of Biophysics, Wageningen University*
13h00	Lunch
14h00	General Meeting
Electrochemical – *Chair: Michael Johns*	
14h30	In situ nuclear magnetic resonance microscopy of batteries and supercapacitors - *Elodie Salager, CNRS, CEMHTI UPR3079, Université d'Orléans*
15h00	Quantitative T_1 Imaging for Battery Characterisation - *Claire Doswell, University of Birmingham*
15h15	Current Density Imaging in Lithium-Ion Batteries - *Igor Sersa, Jozef Stefan Institute*
15h30	In Operando Visualization of Sodium Battery Chemistry by Magnetic Resonance Imaging - *Melanie Britton, School of Chemistry, University of Birmingham*
15h45	Cell Casing Design for in situ Nuclear Magnetic Resonance Imaging on Electrochemical Systems - *Roland Balbierer, Institute of Mechanical Process Engineering and Mechanics, KIT*
16h00	Closing

What to do in Paris?

Suggestions for the free afternoon:

- *La Tour Eiffel*
- *Musée du Louvre*
- *Musée d'Orsay*
- *Musée du Quai Branly*
- *Musée Rodin*
- *Jardin du Luxembourg*
- *Jardin des Plantes*
- *Panthéon*
- *Sacré-Cœur Montmartre*
- *Arc de Triomphe*
- *Centre Georges Pompidou*

Enjoy!

ABSTRACTS OF ORAL PRESENTATIONS

Educational 1:

MRI Hardware

Lawrence L. Wald

A.A. Martinos Center for Biomedical Imaging
Massachusetts General Hospital,
Harvard-MIT Division of Health Sciences Technology

The textbook formulation of MRI is typically framed with uniform fields, well-controlled linear gradients and stationary objects. Modern model-based iterative image reconstruction methods perhaps with prior knowledge to guide unstable inversion problems, provides new-found power to the hardware engineer who can now rest-easy knowing that the images can be reconstructed under nearly any circumstance. Relaxing the hardware requirements, in turn, has the potential to reduce cost, siting and operational burdens. This directly benefits healthcare by increasing the number of patients with access to MRI examinations and tilting its cost-benefit equation to allow more frequent and varied use. The introduction of low-cost, and/or truly portable scanners could also enable new point-of-care and monitoring applications not feasible for today's scanners in centralized settings.

This talk examines the technical forces and tradeoffs that might facilitate a large step forward in the push to "jail-break" MRI from its centralized location in healthcare and allow it to reach larger patient populations and achieve new uses. We examine hardware costs and potential alternative approaches to hardware design and image encoding, especially with a view toward truly portable or point of care (POC) MRI. We also examine some of the biological constraints holding back high-end gradient design, such as Peripheral Nerve Stimulation (PNS). As biology becomes firmly entrenched in the engineering, the creation and exploitation of new degrees of freedom is needed to navigate these biological constraints. In this case, the hardware must be guided by a solid biological model, which we only recently have for PNS in gradient coil design.

Educational 2:

Zero- and Ultra- Low Field NMR

Dmitry Budker
Johannes Gutenberg University Mainz, GermanyZero- and Ultra- Low Field NMR

In this lecture, I will discuss the unusual but truly fascinating regime of NMR, where the experiment is carried out at such a low magnetic field that that the interactions that a usually the weakest in the hierarchy of interactions in high-field NMR become the dominant ones. Such experiments require unusual for NMR instrumentation (such as efficient magnetic shielding rather than strong magnets) and allow one to do things that are difficult to do otherwise. This includes measuring interactions normally truncated in a high field and imaging things inside metal.

This lecture will be based on the work of our group and numerous collaborators described in publications (including review and tutorial papers) that can be found at:

https://budker.uni-mainz.de/ and http://budker.berkeley.edu/ .

Educational 3:

Relaxometry in porous media

B. Newling
University of New Brunswick, Fredericton, NB, Canada

The magnetic resonance behaviour of nuclear spins turns out to be pleasingly sensitive to their confinement in porous media. Relaxation properties have therefore been measured under all manner of circumstances in rocks, cements, woods, foams, coral and bone, for example.

In this introductory survey, we will discuss the relative importance of various relaxation mechanisms in porous media [1] and their influence on spin-spin and spin-lattice relaxation time constants.

We will compare a range of magnetic resonance methods that may be used to measure relaxation time constants in porous media, including the measurements of correlations between two different relaxation time constants [2]. We will also discuss some approaches for achieving various degrees of spatial resolution of relaxation behaviours.

We will discuss the interpretation of measured relaxation time constants in terms of properties of the porous medium, in the light of the underlying relaxation mechanisms [3].

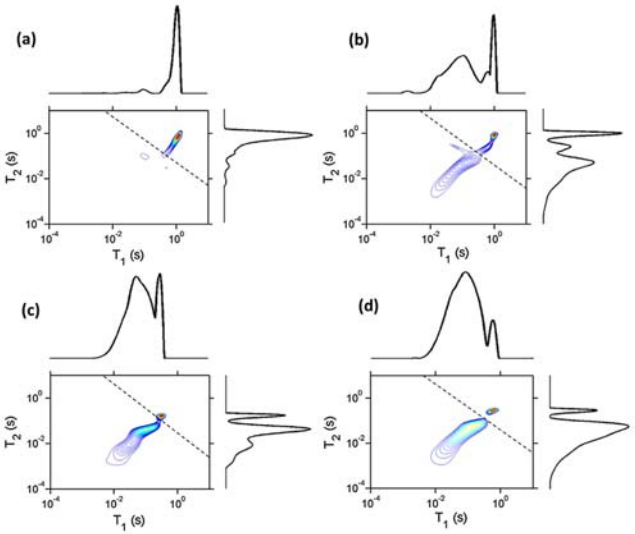

Slice-selective T_1–T_2 contour plots for fluids in a Bentheimer sandstone core plug at different crude oil saturation stages: (a) no crude oil (100% brine saturated), (b) 31% crude oil, (c) 53% crude oil, (d) 68% crude oil. The dashed line indicates the T_1-T_2 "cut-off". Peaks to the left of the cut-off are associated with oil and also brine in small pores. Peaks to the right side of the dashed line arise from the brine in partially oil- and brine-saturated portions of the slice and/or the signal from brine in the fully brine-saturated part of the slice. Reprinted from [2] J. Magn. Reson., 287, Vashaee *et al.*, "Local T_1-T_2 distribution measurements in porous media" pp. 113-122, Copyright 2018, with permission from Elsevier.

References: [1] Barrie, Ann. Rep. NMR Spect. **41** 265 (2000). [2] Vashaee et al. J. Magn. Reson. **287** 113 (2018). [3] Afrough et al. Phys. Rev. Appl. **11** 041002 (2019).

Educational 4:

Diffusion and Flow

M. E. Komlosh

Eunice Kennedy Shriver National Institute of Child Health and Human Development, National Institutes of Health, Bethesda, MD, USA; The Henry M. Jackson Foundation for the Advancement of Military Medicine, Inc., Bethesda, MD, USA;

Magnetic resonance measurements of Molecular translation have improved dramatically since first introduced by Carr and Purcell in the 50's[1] . Today, diffusion, dispersion, advection and flow measurements are a fundamental tool, used routinely in a wide range of applications ranging from investigating chemical reactions[2] to in vivo characterization brain pathology[3]. At the core of most of these methods stands the Pulsed Field Gradient sequence that was introduced by Stejskal and Tanner in 1965[4].
In this talk we will cover the basic principles of diffusion and flow measurements using the classic PFG sequence, review the extension of the pulse sequence into 2D and other variants of the sequence [5][6]. We will also review some applications relevant to the microscopy community.

References

[1] H. Y. Carr and E. M. Purcell, "Effects of diffusion on free precession in nuclear magnetic resonance experiments," *Phys. Rev.*, vol. 94, pp. 630–638, 1954.
[2] M. M. Britton, "MRI of chemical reactions and processes," *Prog. Nucl. Magn. Reson. Spectrosc.*, vol. 101, pp. 51–70, 2017.
[3] P. C. Sundgren, Q. Dong, D. Gómez-Hassan, S. K. Mukherji, P. Maly, and R. Welsh, "Diffusion tensor imaging of the brain: Review of clinical applications," *Neuroradiology*, vol. 46, pp. 339–350, 2004.
[4] E. O. Stejskal and J. E. Tanner, "Spin diffusion measurements: Spin echoes in the presence of a time-dependent field gradient," *J. Chem. Phys.*, vol. 42, no. 1, pp. 288–292, 1965.
[5] P. T. Callaghan, *Translational Dynamics and Magnetic Resonance: Principles of Pulsed Gradient Spin Echo NMR*. New York: Oxford University Press, 2011.
[6] W. S. Price, *NMR studies of translational motion*. Cambridge University Press, 2009.

Plenary Lecture:

Abragam to Zeugmatography: A Physicist's Fascination with Fields

D. I. Hoult
David Hoult Consulting Ltd., Winnipeg, Canada

Why does a person become a research scientist, and why does a particular area enthral so? Children are intensely curious, and as a boy, I witnessed the power of the rare and mysterious phenomenon of ball lightning. It rolled across a field and punched a hole in the wall of a local hospital. I was immediately enthralled, and soon very curious about all things electric. Before long, I was picking up paper clips armed with only old tobacco tins, some wire and a steady supply of batteries. But how on earth was it possible to have such "action at a distance"?

Not surprisingly, when I studied physics at Oxford, classical electromagnetism and electronics were my best subjects. Despite excellent tutoring, however, I still didn't (and don't even now) completely understand electromagnetic fields *de profundis*, and it was a constant annoyance, a nagging need that extended to many other areas and made rote learning a terrible chore. I know I drove at least one of my tutors mad by asking utterly fundamental questions he couldn't answer. I was predestined to be a researcher, thanks to genes and a large and lethal glowing ball.

This attitude (pathological need/perfectionism?) has been with me all my life, and with it has come both triumph and trouble. An utterly fundamental understanding enriches confidence and intuition, and whilst the popular vision of a scientist is someone who "stares with self-conceit through horn-rimmed glasses and destroys poetry" (Einstein), scientists who neither listen to their intuition nor let it fuel their imagination are foregoing a major asset.

In the first days of my graduate career with Rex Richards in the Department of Physical Chemistry, I was given the "NMR bible" – Anatole Abragam's *The Principles of Nuclear Magnetism.* I soon intuited that the chapter on signal detection was vague and inapplicable to the newly invented Fourier transform NMR. I suspect the post-doctoral fellows did not know what to make of me! Who was this kid to challenge Abragam? Of course, I was forced to give a very rigorous justification of my views. Then, a few years later, my intuition kicked in again when I read a couple of early zeugmatography (imaging) papers and knew immediately they were wrong. That got me into some trouble, but nowhere near as much as later in my career when I found I was disagreeing with Nobel prize winners! So what do you do when you "just know" papers by very senior scientists are wrong?

Then Rex resigned and moved our research group to the Biochemistry Department. What a shock! *Terra incognita* and about 30% women researchers as opposed to 2% in physics. Why the different demographics? (I think I found a few answers later in my career, when the best physics student I ever had was a woman.) Apart from designing and building a spectrometer, what could I contribute? Again, fundamental understanding of physics (and surprisingly of electronics) came to the rescue once I had learnt a few basic things about muscles. The result was an important paper on examination of muscle metabolism by NMR.

Science and its public perception have changed, particularly in N. America where there is a revolt against rationalism fuelled by fundamentalist religion and complacency on the part of science. Nevertheless, scientific research remains important for the benefit of society, and now my career has ended, I hope I can pass on some of the lessons I have learnt.

MR Microscopy

Chair: Luisa Ciobanu

Magnetic Resonance Microscopy Provides Multiple Biomarkers in Animal Models of Neurological Diseases

Alexandra Badea, PhD

Department of Radiology, Department of Neurology, Center for In Vivo Microscopy, Brain Imaging and Analysis Center; Duke University Medical Center, Durham, NC 27710

Network approaches provide sensitive biomarkers for neurological conditions such as Alzheimer's disease (AD). Mouse models provide tools to dissect vulnerable circuits, and to assess the effects of interventions. We hypothesized that magnetic resonance microscopy applied in mouse models is a suitable approach for understanding multifactorial diseases such as AD. This is because it provides sensitive contrast in brain tissue, high resolution, and multivariate biomarkers. We show that MRM based approaches using multiple biomarkers help identify vulnerable circuits in normal aging, and in mouse models of AD.

We used *in vivo* manganese enhanced MRI at 7.1T, at 100 μm isotropic resolution, followed by traditional voxel based analyses to reveal regional differences in volume (morphometry), signal intensity (activity), and magnetic susceptibility (iron deposition, demyelination). These regions included the hippocampus, olfactory areas, entorhinal cortex and cerebellum, as well as the frontal association area. The properties of these regions, extracted from each of the imaging markers, were used to predict spatial memory. We used eigenanatomy, which reduces dimensionality to identify sets of regions that explain the variance in the data. For each imaging marker, eigenanatomy revealed networks underpinning a range of cognitive functions including memory, motor function, and associative learning. The integration of multivariate markers in a supervised sparse canonical correlation approach outperformed single predictor models and had significant correlates to spatial memory (1).

Diffusion tensor imaging is particularly well suited for examining brain networks, and how their properties change with aging, or in AD. But connectomic studies in mouse models require long times for *in vivo* acquisitions. We have thus used DTI in *ex vivo* specimens at 9.4T to examine in detail vulnerable brain networks, with reduced time constraints. Based on a data set (2) acquired over 10 days using 120 diffusion directions, and 43 um resolution we have produced simulated connectomes, aiming to balance angular, spatial resolution and scan time. We evaluated protocols with 6, 12, 15, 20, 30, 45, 60 and 120 angles; and voxel sizes of 43, 86 and 172 μm. Our results indicate that a scheme using 46-60 directions, and 86 μm resolution retrieve similar connectomes to a high spatial, high angular resolution sampling scheme, while increasing efficiency. Using compressed sensing has allowed us to accelerate imaging protocols, allowing us to efficiently acquire 51 directions (46 diffusion weighted, interspersed with 5 non diffusion weighted scans), and reconstruct these at and 55 μm resolution in a high performance computing cluster environment (3). The tracts connecting pairs of atlas regions (4) were used to build connectomes based on a constant solid angle implemented in DIPY (5). Tracts were visualized using MI brain (imeka.ca), and statistically analyzed to reveal network changes. We analyzed network changes based on a recently proposed method for dimensionality reduction (6), called tensor network factorization, which relies on a generalization of principal component analysis (6). Our results indicated that even though qualitatively differences were subtle between representative animals of the two age groups/and genotypes, we could separate the groups based on a tensor network decomposition. We identified the top ranked pairs of regions (out of 54780 connections) in terms of changes in connectivity with age. Our top 30 ranked results pointed to a role for the hippocampus, entorhinal and piriform cortex, and the cerebellum, as well as

for the cerebellar white matter and corpus callosum. Extending the list to the top 100 ranked regions helped identify an extended network comprised of 13 gray matter regions, and 4 white matter regions which contributed to distinguishing between the old and young groups. The gray matter regions included: accumbens, amygdala, caudomedial entorhinal cortex, cerebellar cortex, globus pallidus, hippocampus, hypothalamus, piriform cortex, preoptic telencephalon, septum, striatum, superior colliculus, and rest of thalamus. The white matter regions included the fimbrian, corpus callosum, but also the cerebellar white matter, the inferior cerebellar peduncle. We found an overlap between these regions and those distinguishing mouse models of AD from their age matched controls, in particular for the piriform cortex, hippocampus and cerebellum. Advanced bundle analytics improved the sensitivity and resolution to changes in specific connections. Our results suggest that regions commonly involved in age related neurodegeneration, as well as the cerebellum may play a role in age related vulnerability.

References

1. Badea A, Delpratt NA, Anderson RJ, Dibb R, Qi Y, Wei H, et al. Multivariate MR biomarkers better predict cognitive dysfunction in mouse models of Alzheimer's disease. Magn Reson Imaging. 2019;60:52-67.
2. Calabrese E, Badea A, Cofer G, Qi Y, Johnson GA. A diffusion MRI tractography connectome of the mouse brain and comparison with neuronal tracer data. Cerebral Cortex. 2015:bhv121.
3. Wang N, Anderson RJ, Badea A, Cofer G, Dibb R, Qi Y, et al. Whole mouse brain structural connectomics using magnetic resonance histology. Brain Struct Funct. 2018.
4. Anderson RJC, James J; Delpratt, Natalie A; Nouls, John C; Gu, Bin; McNamara, James O; Avants, Brian B; Johnson, G Allan; Badea, Alexandra. Small Animal Multivariate Brain Analysis
(SAMBA): A High Throughput Pipeline with a Validation Framework. rXiv e-prints. 2017.
5. Garyfallidis E, Brett M, Amirbekian B, Rokem A, van der Walt S, Descoteaux M, et al. Dipy, a library for the analysis of diffusion MRI data. Front Neuroinform. 2014;8:8.
6. Zhang Z, Allen GI, Hongtu Zhu H, Dunson D. Tensor network factorizations: Relationships between brain structural connectomes and traits. arXiv preprint arXiv:180602905. 2018.

Suppressing chemical-shift artefacts in rheo-*micro*MRI measurements of dense oil -in- water emulsions

M.R. Serial[1], T. Nikolaeva[1], F.J. Vergeldt[1], L.N. Arnaudov[2], S. Stoyanov[2], J.A. Dijksman[1], C. Terenzi[1], J. van Duynhoven[1,2], H. Van As[1]

[1]Wageningen University, Wageningen, The Netherlands, [2]Unilever, Vlaardingen, The Netherlands

Introduction: The well-known advantages of rheo-MRI velocimetry make it suitable to quantitatively characterize complex fluids under shear in terms of their time-dependent physico-chemical structure formation/degradation and spatial flow-heterogeneities, that all remain inaccessible by conventional rheometry only [1-3]. Yet, when using the rheo-*micro*MRI setup for high-field spectrometers, in combination with strong PFG gradients with the aim to achieve microscopic spatial resolution, several artefacts are encountered that arise from the strong field gradients, the mechanical instabilities of the sample during shear, and/or from the chemical complexity of the investigated material itself. The latter, known as chemical-shift artefact, may (i) affect the measured velocities, thus leading to significant errors in the estimated local shear rates propagated by the *derivative* of the velocity, and (ii) even prevent the use of simple rheological fitting models, that are ultimately needed to extract relevant structural parameters, such as local yield stress and viscosity (red points in Fig. 1). Hence, minimizing artefacts in rheo-*micro*MRI is a necessary pre-requisite for obtaining a quantitative and accurate characterization of local flow behavior in complex fluids.

In this work, we focus on minimizing chemical-shift artefacts observed in rheo-*micro*MRI measurements of high oil volume fraction oil -in- water emulsions. To this goal, we propose a chemical-shift selective (CSS) method that fully suppresses the water signal, and uses the remaining signals from the oil phase to acquire an artefact-free flow-encoded profile.[4]

Methods: ^{1}H CSS rheo-*micro*MRI one-dimensional (1-D) velocimetry measurements [4] at 7 T using a commercial rheo-MRI accessory. Standard strain-controlled rheology measurements.

Results and discussion: By combining the CSS 1-D rheo-*micro*MRI method with standard torque measurements, it is possible to construct reliable local flow curves that can be successfully modelled (blue points in Fig. 1), from which even subtle effects, such as wall-slip, can be disentangled from changes in the constitutive material properties during time-dependent rheological measurements. The validity of the proposed approach is here demonstrated on a model high oil volume fraction oil -in- water emulsion to quantify the impact of emulsifiers and depletants on the spatially heterogeneous flow behaviour.

Conclusions: The proposed CSS rheo-*micro*MRI approach is shown to successfully eliminate chemical-shift artefacts in velocimetry measurements of high oil volume fraction oil -in- water emulsions, in turn enabling a quantitative determination of local viscosities that otherwise would not be feasible. This approach opens a new way towards aiding the rational design of formulations and processing routes for oil -in- water emulsions, where well controlled flow properties of either water or oil are desirable.

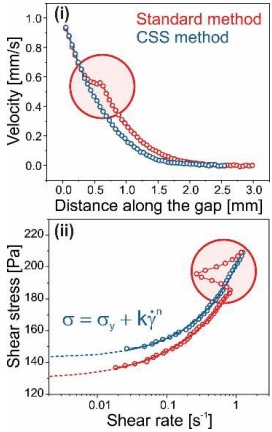

Fig. 1: 1-D velocity profiles (i) and local flow curves (ii) for a commercial mayonnaise at a constant shear rate of 0.62 s^{-1}, employing the standard (red) or the proposed CSS (blue) rheo-*micro*MRI method. All experiments were performed in a 2.5-mm gap Couette cell

References: [1] de Kort et al, Modern Magnetic Resonance (2017). [2] Nikolaeva et al, Langmuir (2019). [3] Nikolaeva et al, Food & Function (2018). [4] Serial et al, Magn. Reson. Chem. (2019).

Identification of Optimal Sampling Patterns for Compressed Sensing RARE MRI in Porous Media

K. Karlsons[a], D.W. de Kort[a], A.J. Sederman[a], M.D. Mantle[a], H. de Jong[b], M. Appel[c], and L.F. Gladden[a]

[a]University of Cambridge, Cambridge, UK, [b]Shell Technology Center Houston, Houston, USA, [c]Shell Technology Centre Amsterdam, Amsterdam, The Netherlands

Introduction: The aim of this work is to acquire pore-scale MRI images and flow velocity maps within porous rocks to better understand structure-flow relationships and to aid the development of so-called digital rock (DR) flow simulators. Given the long acquisition times of such high-resolution images, compressed sensing (CS) is used for the MRI data acquisitions. Optimal **k**-space sampling pattern design is a critical aspect of compressed sensing MRI (CS-MRI). Although various **k**-space sampling strategies have been developed, they often require parameter optimisation to obtain optimal **k**-space sampling patterns [1]. We developed a new, parameter-free **k**-space sampling approach using input from high-resolution 3D X-ray micro-computed tomography (μCT) data sets to derive optimal **k**-space sampling patterns for acquiring high spatial resolution 3D MRI images of rocks.

Methods: μCT images (grain space) of 4 mm diameter rock core plugs, routinely acquired as part of a DR workflow, were inverted to obtain pore space images. These were then Fourier transformed into the expected **k**-space for these rocks. From these **k**-space signatures, optimal CS variable-density sampling patterns [1] were generated for each rock type, spatial resolution, and sampling fraction. CS-RARE [2] in combination with the new **k**-space sampling strategy was used to acquire pore-scale structural CS-MRI images of rocks at (isotropic) resolutions as high as 17.6 μm. Pore size analysis in Avizo was used to benchmark the quality of the MRI images relative to a 5 μm μCT image.

Results and discussion: The μCT-based sampling strategy delivers a bespoke **k**-space sampling pattern for each rock type (Fig. 1) according to the morphology of the rock, which was shown to give an optimal CS reconstruction quality for a range of different sampling fractions (0.125–0.375). The pore space analysis revealed excellent agreement between the pore size distributions of the acquired MRI data of Ketton rock using the μCT-based sampling approach and the 5 μm resolution μCT images. These results highlight the advantage of using the μCT-based approach to deliver accurate pore space reconstructions at spatial resolutions for which a fully-sampled acquisition at those resolutions would be prohibitively long to acquire.

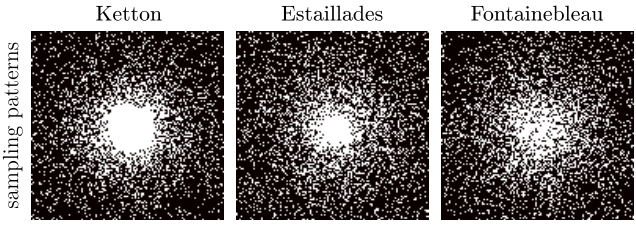

Fig. 1: Sampling patterns of Ketton limestone, Estaillades limestone, and Fontainebleau sandstone as generated by the new, μCT-based sampling approach for a **k**-space sampling fraction of 0.25. The white pixels in the sampling patterns represent the points sampled in both phase-encoding directions. For a 3D CS-RARE experiment, a line in the frequency-encoding direction, orthogonal to both phase-encoding directions, is fully sampled for each of these points.

Conclusion: A novel, robust **k**-space sampling strategy has been demonstrated to generate optimised **k**-space sampling patterns for 3D high spatial resolution microstructural MRI acquisitions from 3D μCT data. This approach can be used to accelerate other MRI acquisitions relevant for DR applications, such as spatially-resolved propagators, fluid velocity maps, and relaxation time maps.

References: [1] Lustig, Magn. Reson. Med. (2007). [2] Ramskill, J. Magn. Reson. (2016).

Compensating Diffusion Bias of Quantitative T_2 on High-Field MRI Scanners

N. Bnaiahu[1], E. Wilczynski[1], N. Omer[1], T. Blumenfeld-Katzir[1], S. Levy[1], N. Ben-Eliezer[1,2]
[1]Tel Aviv University, Tel Aviv, Israel
[2] Center for Advanced Imaging Innovation and Research, NY, USA

Introduction: In high-field scanners imaging gradients (RO, PE and SS) are significant, leading to amplification of diffusion weighting and spurious attenuation of the signal, especially in spin-echo (**SE**) based acquisitions where the effect of diffusion accumulates along the echo train. Thus, T_2 mapping on preclinical scanners is challenged by both diffusion and stimulated echoes. Furthermore, different parameter sets will produce different diffusion and stimulated-echoes signal bias, impairing reproducibility of measured values. In this work we implement diffusion correction of SE and multi echo SE (**MESE**) protocol data in the echo modulation curve (**EMC**) algorithm [1] to unravel the unbiased T2 values of the tissue.

Methods: Effective b-value [2,3] is developed according to the applied **MSME** sequence gradients, it is evaluated per echo based on the subset of coherence pathways that contributed to the signal [4], thus incorporating the effects of stimulated echoes in the diffusion attenuation assessment.

$$effective\ b-value = \gamma^2 I = \gamma^2 \int_0^t \left(\int_0^{t'} g^*(t'')dt'' \right)^2 dt' \qquad \text{Eq.1}$$

A phantom containing concentrations of $MnCl_2$ was imaged on a 9.4T Bruker Biospin. Spectroscopy was performed to achieve unbiased T_2 values. **SSE** and **MSME** imaging sequences were applied with varied parameters. ADC: 2.29 x 10^{-5} cm^2/s. **MSME** data was fitted using the **EMC** algorithm after the diffusion attenuation was corrected. An in-vivo scan was conducted on a 7T Bruker Biospec with **MSME** protocol and high-resolution scan parameters.

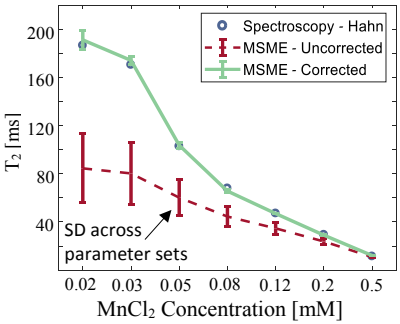

Fig. 1: qT2 from MSME scans of $MnCl_2$ phantom. The green line shows the results after correction of diffusion bias. The bars show the SD over the different parameter sets (varied resolution, slice thickness and BW).

Results: For the 0.02 mM tube, uncorrected results were up to 76% lower than spectroscopy results, after correction max deviation was lowered to 4%; CV value was reduced from 24% to 4% (see Fig. 1 for all concentrations). In-vivo results: corrected T_2 values were raised by 20% in the hippocampus, and by 11% in the cortex and corpus callosum.

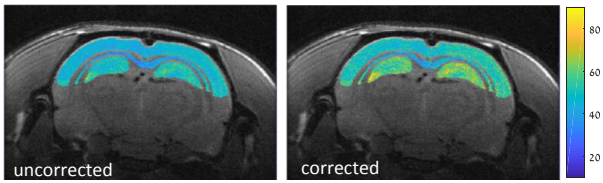

Fig. 2: High resolution in-vivo rat's brain. The segmented areas show T_2 maps [ms] of the cortex, corpus callosum and the hippocampus.

Conclusion: Correction is necessary for high-field / high-resolution qMRI since diffusion effect intensifies as resolution increases. The suggested solution improves accuracy, eliminates the variability observed at different resolutions and slice thicknesses and provides reproducible, steady T2 values.

References: [1] Shepherd, NeuroImage: Clinical. (2017). [2] Abragam, Oxford (1961). [3] Torrey, Phys. Rev. (1956). [4] Hennig, Magn. Reson. (1988).

Selective excitation with colored Frank sequences

A. Görges[a], S. Benders[b], M. Küppers[a], M. Adams[a], B. Blümich[a]
[a] ITMC, RWTH Aachen University, Aachen, Germany, [b] Department of Chemistry, NYU, New York, NY USA

Introduction: Inspired by the development of miniaturized NMR devices and the growing interest in their use in material science as well as for chemical and biological research, low-power rf excitation is explored to eliminate the transmitter amplifier. The lowest excitation power is achieved with sequences of phase-modulated, constant-amplitude rf pulses, whereby one pulse is applied each sampling interval. The earlier realizations such as maximum-length binary sequences rely on the Hadamard transformation [1-2] and hamper selective excitation for solvent signal suppression and slice-selective imaging [3]. Frank sequences [4] promise a new way out. They can be understood as being composed of packets of discrete phase wavelets arranged in such a way that one scan with a Frank sequence corresponds to a rapid frequency sweep through the spectral excitation window. This suggests that individual wavelets could be omitted to skip a narrow frequency region in the excitation spectrum. It could be shown that selective signal suppression in the low power regime is possible for NMR spectroscopy and imaging without resorting to more demanding schemes like SPREAD [3] or WURST [5].

Methods: Frank sequence excitation with 3.8 µW and 16 k pulses was realized on a Bruker AV 300 MHz spectrometer. Data acquired with conventional pulse excitation are compared to those acquired with µW Frank excitation. Different approaches for selective signal suppression are tested in terms of applicability, spectral quality and efficiency. Additionally, imaging experiments with Frank excitation were tested, as the low-power excitation promises short dead time.

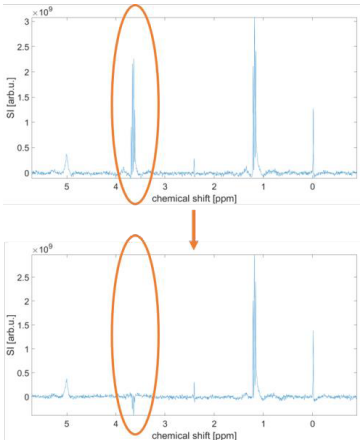

Figure 1: Selective signal suppression by colored Frank-excitation. Here the CH_2 signal of ethanol is suppressed by replacing an excitation wavelet with zero-amplitude pulses. The remaining spectrum is largely unaffected.

Results and Discussion: Figure 1 depicts ethanol spectra obtained with Frank excitation as mentioned above. The top one has been acquired with non-selective excitation, while the bottom one has been acquired with colored Frank excitation to suppress the signal of the CH_2 group. Figure 2 illustrates the application of Frank excitation in MRI.

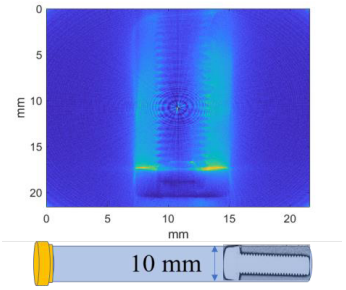

Figure 2: 2D image of a screw in a 10 mm water filled sample tube obtained with Frank excitation at 5 mW peak amplitude power.

References: [1] Ziessow, Ber. Bunsenges. Phys. Chem. (1974). [2] Kaiser, J. Magn. Reson. (1973). [3] Nielsen, Magn. Reson. Imaging (1996). [4] Blümich, J. Magn. Reson. (2009). [5] Laustsen, J. Magn. Reson. (2014).

Splitting one dimension into four: progressing from diffusion distributions into diffusion tensor distributions

J. P. de Almeida Martins[a], *D. Topgaard*[a]
[a]Lund University, Lund, Sweden

Introduction: To this date, relaxation-diffusion correlation studies have relied on the Stejskal-Tanner experiment [1] where the signal is encoded for diffusion using a pair of collinear gradient pulses. Diffusion-encoding along a single direction convolves the contributions of isotropic and anisotropic diffusivities into a single 1D distribution of effective diffusivities, thus preventing the unambiguous quantification of microscopic environments within heterogeneous anisotropic materials. To overcome this difficulty, we translated data acquisition and processing schemes from multidimensional solid-state NMR into the field of diffusion NMR [2-4], and devised a new framework wherein microscopic heterogeneity is resolved with 4D diffusion tensor **D** distributions rather than 1D scalar diffusion distributions. Here, we demonstrate our novel framework with an MRI protocol that quantifies the microscopic heterogeneity of the living human brain in a 5D space of R_2 and axisymmetric **D**.

Methods: Data was acquired at multiple echo-times and axisymmetric diffusion-encoding tensors, parameterized by four independent dimensions: size, orientation, and normalized anisotropy. This yields 5D datasets that are converted to spatially resolved 5D R_2-**D** nonparametric distributions using an unconstrained Monte Carlo approach. Different acquisition protocols were tested on healthy volunteers using a custom spin-echo diffusion-weighted EPI sequence. The shortest protocol resulted in a scan time of 15 min.

Results and discussion: Pure component voxels containing either white matter WM, gray matter GM, or cerebrospinal fluid CSF give rise to clearly distinctive R_2-**D** distributions that accurately capture the main microscopic features of the various tissues (CSF: high isotropic diffusivity D_{iso}, low normalized diffusion anisotropy D_Δ, low R_2; WM: low D_{iso}, high D_Δ, high R_2; GM: low D_{iso}, low D_Δ, high R_2). As shown in Fig. 1, voxels comprising mixtures of GM, WM, and GM are characterized by multimodal distributions wherein the contributions from distinct tissue environments can be easily discerned. The rich information contained within the voxel-wise R_2-**D** distributions is visualized as sets of statistical parameter maps, or arrays of smooth Orientation Distribution Functions.

Conclusion: We demonstrate a protocol to resolve broad 1D diffusion distributions into four distinct dimensions of D_{iso}, D_Δ, and diffusion tensor orientation. In the context of *in vivo* brain studies, 5D R_2-**D** distributions can separate and characterize sub-voxel tissue environments without assumptions on the number or properties of the individual environments. Good quality data can be acquired within a scan time of 15 min, meaning that the proposed protocol displays great potential for clinical studies dealing with tissue heterogeneity (*e.g.* tumor infiltration in healthy tissue).

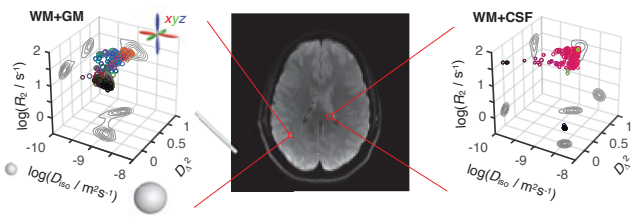

Fig.1: 5D R_2-**D** distributions shown as logarithmic plots of the isotropic diffusivity D_{iso}, squared normalized diffusion anisotropy D_Δ^2, and R_2, with circle area proportional to the weight of the corresponding $P(R_2,\mathbf{D})$ coordinates. Here, we display the distribution from two voxels; one containing a mixture of white matter WM and gray matter GM, and another containing both WM and cerebrospinal fluid CSF.

References: [1] Stejskal, J. Chem. Phys. (1965). [2] de Almeida Martins, Phys. Rev. Lett. (2016). [3] de Almeida Martins, Sci. Rep. (2018). [4] Topgaard, NMR Biomed. (2019).

Mobile & Low Field

Chair: Dimitrios Sakellariou

The Recent Development of a Low-field Permanent-magnet-based MRI Head Imager

Shao Ying HUANG[1], Zhi Hua REN[1], Jia GONG[1], Wen Chuan MU[1], Wenwei YU[2]

[1]Singapore University of Technology and Design, Singapore, [2]Chiba University, Chiba, Japan

Introduction: A portable magnetic resonance imaging (MRI) imager may help this medical imaging modality to reach out areas that are remote or/and hard to access, and situations that the environment is dynamic, for example, in an ambulance. This talk reports the recent progress of the development of a low-field permanent-magnet-based MRI head imager in Singapore University of Technology and Design (SUTD). It includes the latest design of an inward-outward (IO) ring-pair magnet array, which supplies a strong longitudinal magnetic field with a monotonical pattern, and an investigation of the encoding field in general that is supplied by a permanent magnet array, in terms of its effects on image quality.

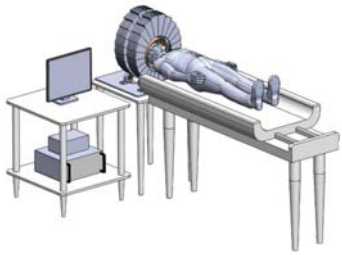

Fig. 1: An illustration of a low-field permanent-magnet-based MRI head imager.

Method, Results & Discussions: IO ring-pair arrays (Fig. 2 (b) and (c)) were proposed that supply a relatively strong magnet field along a longitudinal direction for signal encoding for MRI. They are based on an IO ring pair which has one ring that has the magnetization pointing radially inward and the other pointing radially outward [1]. The IO ring-pair aggregate and the irregular array supply a concentric (average field (B_{0avg}) of 170mT, homogeneity (ΔB_0) of 24,786ppm) and a nearly monotonic field patter (B_{0avg} = 133mT, ΔB_0 = 151,840ppm), respectively. They both do not have linear gradients. Compared to a short Halbach sparse array (Fig. 2 (a), B_{0avg} = 68mT, ΔB_0 = 42,000ppm) [2-3], they both have much stronger magnetic field. The uniqueness of the field patterns they generate are identified. They are further compared in terms of the image quality numerically when they are rotated and used to encode signals in an MRI system. Local k-space and point spread function are used to analyze the relation between the field patterns and the image quality.

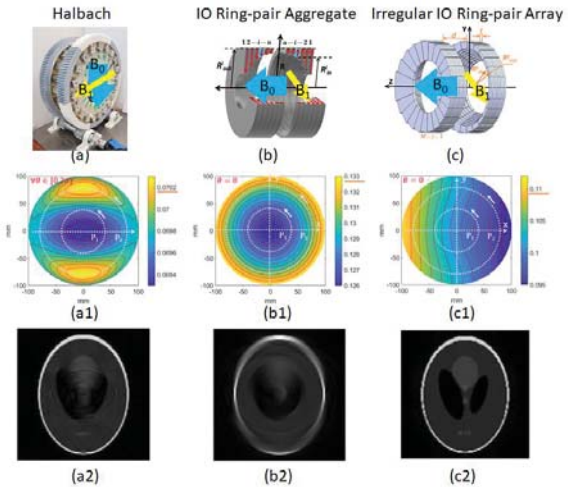

Fig. 2 Different magnet arrays (row one), their magnetic fields (row two, and the numerical reconstructed images (row three) when they rotate.

Conclusion: The IO ring-pair magnet arrays can be good candidates for low-field permanent-magnet-based MRI systems. The method for analyzing the relation between a permanent-magnet-generated magnetic field with a non-linear gradient, and the quality of the corresponding reconstructed image can be used to guide the design of permanent magnet arrays to improve quality of MRI of this type.

References: [1] G. Miyajima, Japanese Patent JPS60210804A (1985) [2] C. Z. Cooley et al., Magn. Reson. Med., (2015) [3] Z. H. Ren, et al, IEEE MTT-S Int. Microw. Symp. Dig., (2015)

CPMG with Time-Dependent Fields: Observation of Adiabatic and Non-Adiabatic Behavior

M. D. Hürlimann, S. Utsuzawa, C.-Y. Hou
Schlumberger – Doll Research, Cambridge MA, USA

We present experimental results and a new theoretical framework to analyze the effects of time dependent magnetic and RF fields on the spin dynamics of the Carr-Purcell-Meiboom-Gill (CPMG) sequence. The theoretical analysis is based on the decomposition of the magnetization into the eigenmodes of the propagator of a single refocusing cycle. For sufficiently slow changes in the external fields, the magnetization follows the changing eigenmodes adiabatically. This results in echo amplitudes that show regular modulations with time. Faster field changes can induce transitions between the eigenmodes. Such non-adiabatic behavior occurs preferentially at particular offsets of the Larmor frequency from the RF frequency where the eigenmodes become nearly degenerate. We introduce the instantaneous adiabaticity parameter $\mathcal{A}(t)$ that accurately predicts the crossover from the adiabatic to the non-adiabatic regime and allows the classification of field fluctuations. $\mathcal{A}(t)$ is determined solely by the properties of a single refocusing cycle under static conditions and the instantaneous value of the field offset and its temporal derivative.

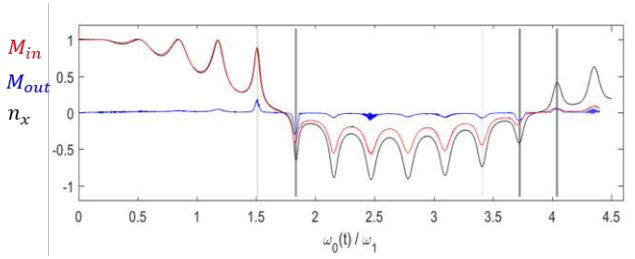

Fig. 1: Experimental CPMG results for in- and out-of-phase echo amplitudes in an increasing magnetic field versus normalized offset of the Larmor frequency. Theory for adiabatic limit is shown in black. Non-adiabatic events occur when the adiabatic condition $\mathcal{A}(t) \gg 1$ is not fulfilled (gray shading).

In the adiabatic regime when $\mathcal{A} \gg 1$, the impact of field variations is fully reversible. This is demonstrated experimentally in Fig. 2 for the case when the field is ramped up and down. When the conditions for the field sweep is entirely in the adiabatic regime, the final magnetization fully recovers the value that is observed in a stationary field. When the ramp includes non-adiabatic regions (shown as black bands), the magnetization at the end of the ramp is reduced. The locations of the non-adiabatic regions occur precisely at the anticipated offset fields when the eigenmodes become nearly degenerate.

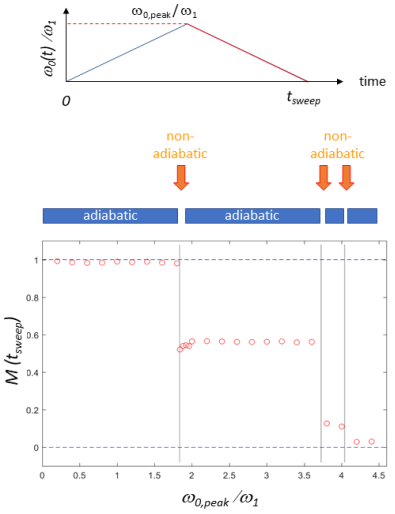

Fig. 2: Experimental CPMG results of the magnetization at the end of the sweep, t_{sweep}, versus the amplitude of the field sweep. The location of the non-adiabatic regions are clearly evident and coincide with the theoretically prediced locations, shown as gray shading, where the eigenmodes become nearly degenerate.

Matrix Pencil Method for High Resolution Data Processing in Low-Field NMR

S. N. Fricke, M. P. Augustine
University of California, Davis, CA 95616, USA

Introduction: Recent advances have made portable nuclear magnetic resonance (NMR) spectroscopy economically and practically feasible. The ease with which it can be customized makes portable NMR an extremely desirable analytical technique. However, portable NMR obtains a weaker signal with decreased resolution compared to traditional NMR. As such, one typically measures exponential decay constants at low field rather than frequencies.[1] Here, the matrix pencil method (MPM)[2,3] is explored for stable, reproducible data processing in low field NMR. Currently, the inverse Laplace transform (ILT) is the conventional method for processing data in low field NMR. However, the ILT is hindered by sensitivity to noise, poor resolution, and high computational requirements that make it difficult to apply in non-laboratory environments. Improving the efficiency of data processing could expand the applications of portable NMR and enhance the quality of information gained from correlation experiments. The MPM fits in a broad category of filter diagonalization methods for digital signal analysis, and was developed for use in radar, antenna, and acoustics technologies. The success of the MPM in other areas of signal processing makes its application to low field NMR promising.

Methods: The MPM is developed as an alternative to the ILT for data processing, due to its low noise sensitivity, high resolution, and minimal computational requirements. This advantage is gained primarily by exploiting the eigenstructure of a matrix pencil, which can be formulated directly from discretely sampled data, thereby avoiding integral transforms. Applications to both real and simulated data are shown, and the respective errors of the MPM and ILT are evaluated with Monte Carlo simulations as well as with a combinatorics-based bootstrap resampling approach.

Results and Discussion: In the cases presented here, the MPM performs better than the ILT from the standpoints of speed, resolution, and accuracy. Moreover, in the limit of zero noise, the MPM provides an analytically exact, closed-form solution to the problem of multi-exponential decomposition.

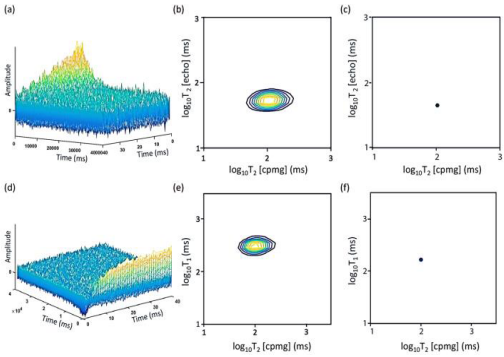

Fig. 1: Polydimethylsiloxane at 100 MPa. The raw data surface in a) is from a T_2/T_2 correlation experiment, with the corresponding spectrum processed by b) ILT and c) MPM. The raw data surface in d) is from a T_1/T_2 correlation experiment, with the corresponding spectrum processed by e) ILT and f) MPM.

Conclusion: The key for widespread future implementation and automation of the MPM is to combine it with effective noise filters, such as singular value decomposition, multi-point moving averaging, integration smoothing methods, wavelet transforms, and sliding Fourier transform apodization. This will ultimately enable measurements of systems that have previously been inaccessible with portable NMR.

References: [1] Blumich, B., Perlo, J., & Casanova, F., *Prog. Nucl. Mag. Res. Sp.*, *52*(4), 197–269. (2008). [2] Hua, Y., & Sarkar, T. K., *IEEE Trans. Sig. Proc.*, *38*(5), 814–824. (1990). [3] Lin, Y. Y., Hodgkinson, P., Ernst, M., & Pines, A., *J. Mag. Res.*, *128*(1), 30–41. (1997).

Imaging sorghum roots in natural soil

Dean O. Kuethe[1], Stephen A. Altobelli[1], Mark S. Conradi[1], G. Cody Bagnall[2], Eiichi Fukushima[1], Cristine L. S. Morgan[2]

[1]ABQMR, Albuquerque, NM, USA; [2]Texas A&M University, College Station, TX, USA

Introduction: It is relatively easy to measure the parts of crop plants that are above ground to improve agricultural procedures and plant genetics. Nonetheless, the roots are important parts and the world lacks a good way to measure their configuration *in situ*. One typically digs the roots up and washes off the soil. Then, they are not as they were in the ground. This project endeavors to image the roots of energy sorghum (*Sorghum bicolor*) in natural soils. Previous plant-root MRI pursuits were complicated by the fact that almost all natural soils have high magnetic susceptibility and researchers used their existing high-field laboratory MRI systems [1-5]. Either high-susceptibility soils distorted the images or the water in special synthetic or low-susceptibility soils had similar relaxation to the water in roots and the two were difficult to separate.

Methods: We constructed a prototype 47 mT (2 MHz proton resonance) electromagnet, magnetic-field-gradient coils, and a quadrature, double-saddle RF coil to image 250 ml samples. At this lower field, water in roots in natural soils has T_2*>3 ms, T_1 about 1 s, and T_2 about 300 ms. Water in natural soils has T_1 about 4 ms and T_2 about 1 ms. By using a 16-echo, spin-warp sequence with 7 ms echo spacing, we avoid signal from soil water and make images of roots alone.

Results and Discussion: The signal-to-noise ratio (SNR) is expectedly low compared to higher-field systems. It currently takes about 9 hours to make a 3D image. Alternatively, we take 8 or 10 2D spin-warp images (third dimension is unresolved) with equally-spaced view angles that rotate 180 degrees around the vertical axis. When the images are played as frames if a video, the roots appear to rotate about the vertical axis. The mind's eye constructs a 3D image of the roots. One can stop the video at appropriate views to measure branching angles and one can extract root diameters. Thus, we gain the necessary biological information without a full 3D image in about 20% of the scan time. We also take advantage of the fact that the roots are sparse and appear as light streaks in a dark background. We can detect roots smaller than the voxel size and ascertain the partial volume they fill by pixel brightness. Thus, we can use coarse-resolution images that deliver relatively high SNR in short scan times.

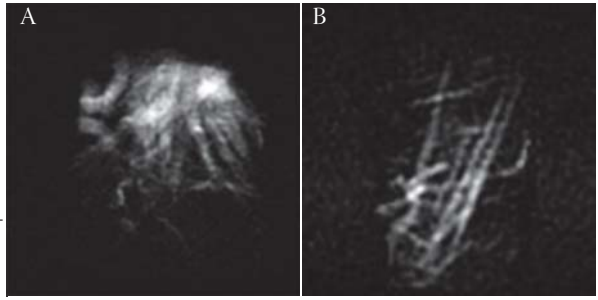

A shows a single frame of sorghum crown roots grown in Houston Black soil in a greenhouse; **B** shows field-grown roots in a clay loam.

We are currently assembling a full-size, field-deployable system. The roots will remain *in situ* but soil around them will be excavated to make room for the MRI system. A 244 mm ID, 267 OD PVC pipe will be pressed into the ground around the chosen plant roots to maintain them in their natural configuration. An approximately 0.7 m diameter annular hole will be excavated around the sample and the MRI system with 620 mm OD and 279 mm clear bore will be lowered in place for imaging.

References:

[1] P. A. Bottomley, H. H. Rogers, T. H. Foster. Proc. Natl. Acad. Sci. 83:87-89 (1986).
[2] H. H. Rogers, P. A. Bottomley. Agron. J. 79:957-965 (1987).
[3] J. Votrubova, M. Sanda, M. Cislerova, M. H. G. Amin, L. D. Hall. Geoderma 95:267-282 (2000).
[4] L. D. Hall, M. H. G. Amin, E. Dougherty, M. Sanda, J. Votrubova, K. S. Richards, R. J. Chorley, M. Cislerova. Geoderma. 80:431-448 (1997).
[5] R. E. Prebble, J. A. Currie. J. Soil Sci., 21:273-288 (1970).

Multi-coils Design of Downhole NMR Azimuthal Imaging Probe

S.H. Luo[a], L.Z. Xiao[a,b], G.Z. Liao[a], Y. Zhang[a].
[a]China University of Petroleum, Beijing, China; [b]University of Harvard, Boston, USA

Introduction

During last decades, wireline NMR downhole tools and logging while drilling (LWD) NMR downhole tools were widely welcomed and applied in oil industry and the hardware was continued updating. However, the single coil configured in the probe combined with gradient magnetic field is only able to achieve radial profile imaging but not azimuthal imaging. In order to understand formation better, inhomogeneity for example, azimuthal imaging will provide more comprehensive data and visualized map around borehole. Recently, some progress about azimuthal imaging had been made [1,2].

Content

In this paper, we design and implement a multi-coils structure configured in the probe combined with quadruploar magnet [3] to achieve azimuthal imaging. The electromagnetic simulation was done with the help of commercial software ANSYS HFSS by using FEM. The magnet assembly is consisted of four bread-shaped magnets combined with additional small hexangular magnets to produce enough strength and high homogeneity of static field along with circumferential direction at deeper DOI This multi-coil is consisted of four saddle-shaped surface coil elements which are equally positioned at four different directions. Capacitive networks are used to eliminate the mutual effects and enhance the performance of the multi-coils.

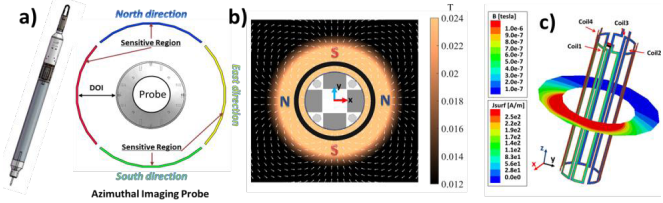

Fig. 1: a) is the illustration of azimuthal imaging probe; b) is the quadrupolar static field map; c) is the configuration of multi-coils and RF field map for one coil.

Results and Conclusion

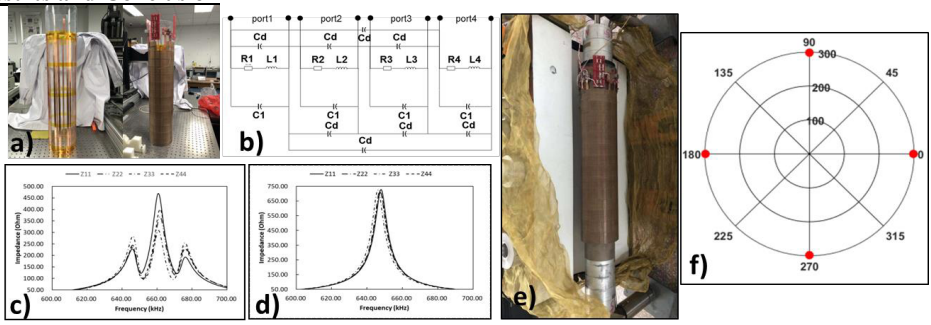

Fig. 2: The manufactured multi-coils and azimuthal measurement result. a) is the multi-coils; b) is the scheme of capacitive decoupling for multi-coils; c) is the coupling result of multi-coils; d) is the decoupling result of multi-coils; e) the illustration of test for multi-coils, the probe is put in a water tank which is splited into four sections; f) azimuthal measurement result, the solution is copper sulfate solution with the same concentration, and T_2 value is 298 ms corresponding to red dots. The circle lines are representing the isoline of T_2, polar coordinate is representing the azimuthal degree.

This probe can achieve azimuthal imaging measurement by using quadrupolar magnet and multi-coils array. However, this work is still faced with technical problems to be solved, such as the data post-processing and development of design of probe.

References: [1] W.Liu, Micro. Meso. Mater., vol. 269, pp. 97–102, 2018.
[2] S.H. Luo, IEEE TGRS, vol. 57, No.5, pp. 2939-2946, 2019.
[3] S.H. Luo, Magn. Reson. Imaging.. vol. 56. pp. 168-173, 2019.

Multi-phase flow measurement using an Earth's field NMR flow meter

Keelan O'Neill, Paul Stanwix, Einar Fridjonsson and **Michael Johns**
Department of Chemical Engineering, University of Western Australia, Crawley, Western Australia, Australia

We present a novel multiphase flow metering technique (photo of apparatus shown below) for simultaneous measurement of oil, gas and water volumetric flowrates. An Earth's field nuclear magnetic resonance (NMR) r.f. detection coil is applied to measure free induction decay (FID) signals of oil/water/gas flows. A dual polarisation technique is introduced utilising an upstream permanent magnet as well as an electromagnetic pre-polarising coil. FID signals with variable pre-polarising conditions are acquired and fit with a model for the NMR fluid signal using a 2D Tikhonov regularisation algorithm, allowing determination of a joint 2D velocity-T_1 probability distribution. Appropriate analysis of the measured velocity-T_1 distributions allows calculation of individual phase flowrates. The performance of the NMR flow measurement technique is examined for oil/water/gas flows which are visually observed to be in different flow regimes: stratified flow with mixing, dispersion of oil-in-water and water, and full oil-in-water emulsions – sample data is shown below for dispersed *oil-in-water + water* flow. Flow characteristic features such as velocity slip are examined for each flow regime. Finally the accuracy of the measurement system in each flow regime is validated against in-line rotameter measurements. Extensions to render a more robust instrument using a Q-switch, real time magnetic field mapping and multiple r.f. coils, as well as industrial validation using a large flow loop, will be briefly outlined.

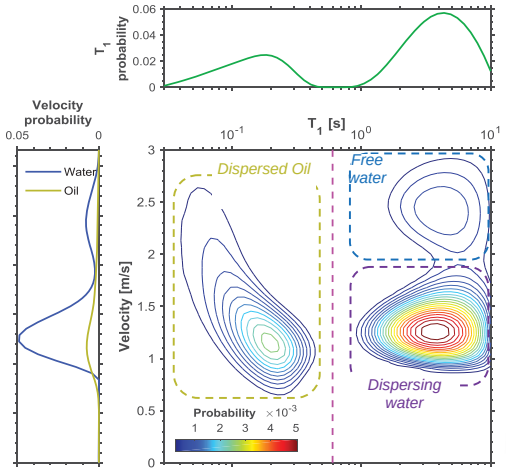

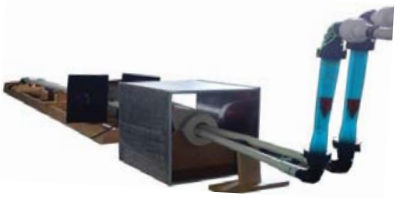

References:

[1] O'Neill, K.T., Brancato, L., Stanwix, P.S., Fridjonsson, E.O. and Johns, M.L. (2019) Two-phase oil/water flow measurement using an Earth's field nuclear magnetic resonance flow meter, ***in press***, *Chem. Eng. Sci.*
[2] O'Neill, K.T., Klotz, A., Stanwix, P.S., Fridjonsson, E.O. and Johns, M.L. (2017) Quantitative Multiphase Flow Characterisation using an Earth's Field NMR Flow Meter, *Flow Meas. & Instr.*, **58**, *104-111.*
[3] O'Neill, K.T., Fridjonsson, E.O, Stanwix, P.S. and Johns, M.L. (2016) Quantitative Velocity Distributions via Nuclear Magnetic Resonance Flow Metering, *J. Magn. Res.*, **269**, *179-185.*

Groupement
AMPERE

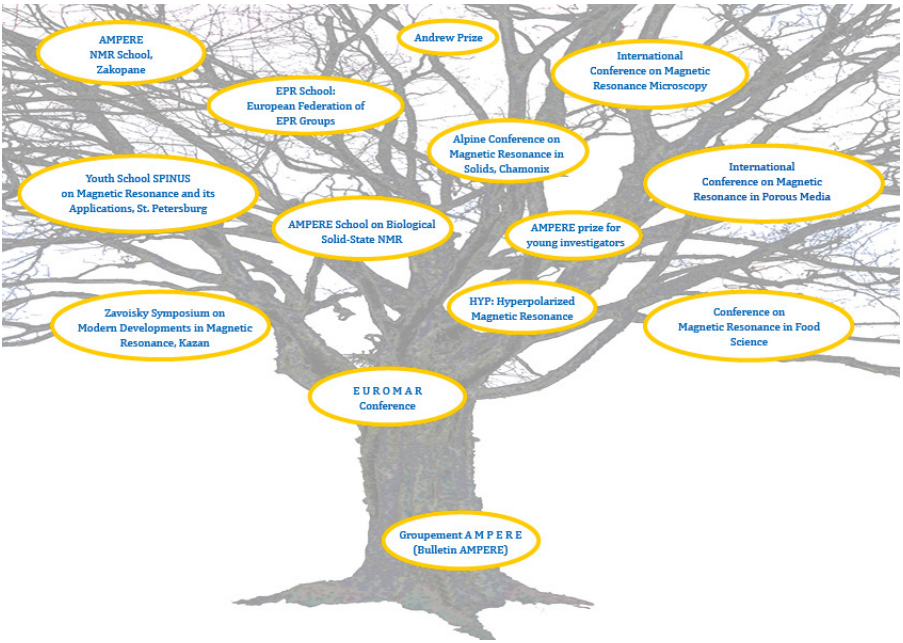

cea

Institut
des sciences du vivant
Frédéric Joliot

Frédéric Joliot Institute for life sciences, including Neurospin, is one of the nine institutes of the CEA Fundamental Research Division. Joliot Institute brings together research teams around three thematic axes dedicated respectively to integrative biology of the cell, biomedical imaging and diagnostic and therapeutic innovation. This research is fundamental, technological, methodological or applied. It gives the institute a very large positioning, from research to industry, to respond to societal issues related to health, energy and bio-defense. The Institute expertise covers a broad spectrum of skills, ranging from mathematics and computing to medicine, including physics, chemistry and biology. This multidisciplinarity enables to study life in all its complexity, from molecular mechanisms to whole organisms.

To know more about Frédéric Joliot Institute for Life Sciences:
http://joliot.cea.fr/drf/joliot/en

To know more about the CEA: http://www.cea.fr/english

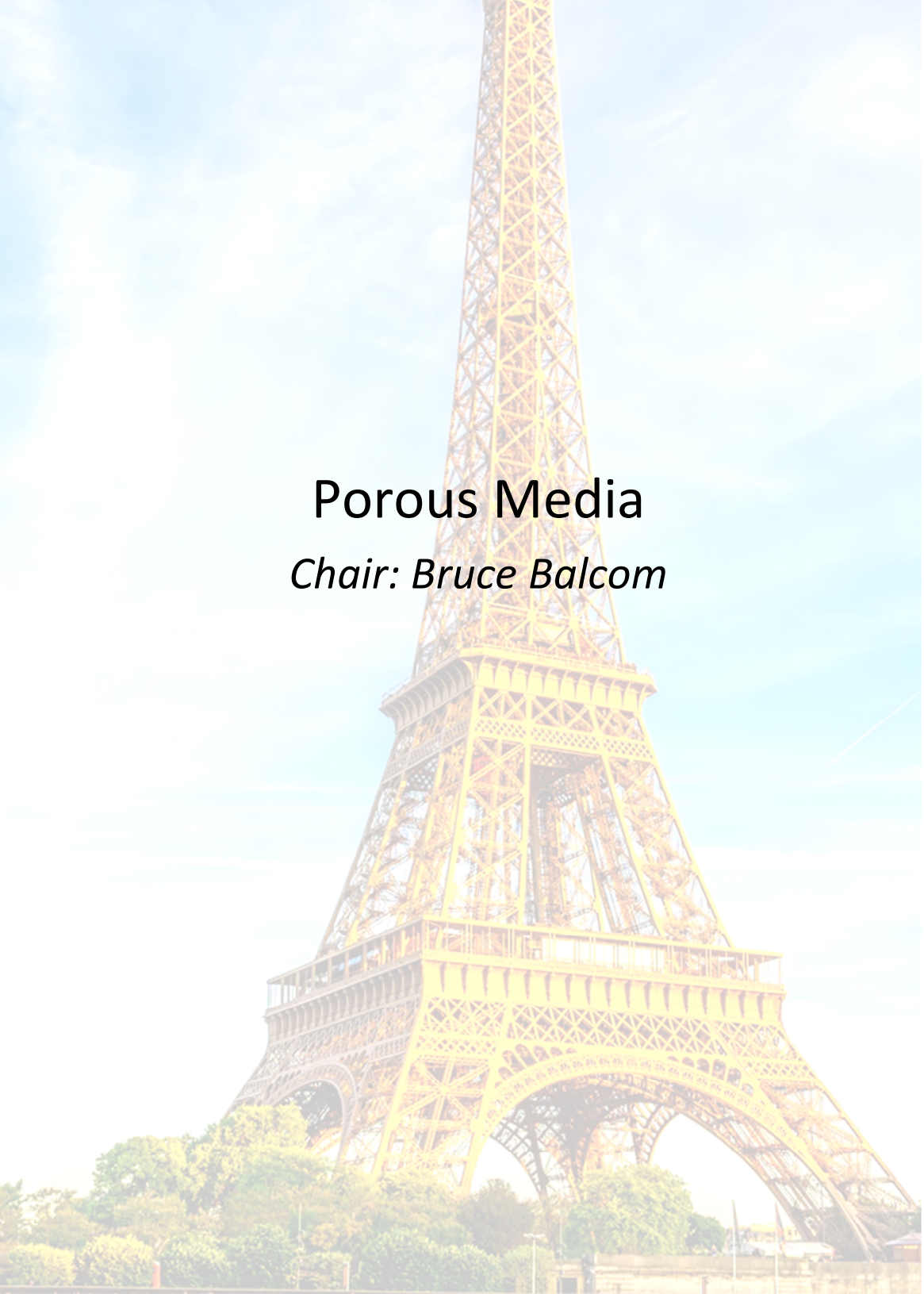

Porous Media

Chair: Bruce Balcom

Porous Media and Rethinking Assumptions

Kate Washburn, Evan McCarney, Yuesheng Cheng

Nuclear magnetic resonance has been used to characterize porous media for decades. Much of this research has been focused on a few types of materials, such as rocks or cement. As such, many standard analysis methods and interpretations in porous media were developed around these types of systems. In recent years, researchers are now starting to examine new types of materials, such as food or biological samples, through the lens of porous media. However, many of the assumptions and interpretations developed for geological samples break down when applied to different materials. In particular, the standard explanation of surface relaxivity does not appear to be valid in these systems. This talk will discuss challenges encountered as established NMR porous media methods are used to analyze a wider range of materials. Examples will range from oil bearing shale to hydrolysis of fish byproducts.

Probing pore connectivity of rock cores by PcT2 correlation spectroscopy

Yiqiao Tang[1], Yi-Qiao Song[1], Stacy Reeder[1], Andre Souza[1,2], Muthusamy Vembusubramanian[1], Kamilla Fellah[1], and Ling Feng[1]

1. Schlumberger-Doll Research
2. Schlumberger Brazil Research and Geoengineering Center

Petroleum reservoirs are complex bodies due to geological processes, such as sedimentation, cementation, dissolution, and dolomitization. These processes lead to complex systems of pore bodies and throats. Consequently, reservoir rocks embody tortuous pore structures with a wide range of pore sizes and connectivity. Characterization of the intricate pore networks are especially important in prolific carbonate systems, where diagenesis and secondary porosity can lead to low-resistivity pay or isolated pore systems with high porosity and low permeability. Properly characterizing these body-throat relationships can also help lead to more characteristic permeability calculations.

Although laboratory methods abound to probe pore body and pore throat sizes independently, it has not been possible to determine their correlations in a bulk sample. Without understanding the connections between the pore bodies and pore throats, it is possible to mis-characterize the complexity of a sample and reduce pore models to simple bundle-of-tubes.

In the oilfield, NMR relaxometry and capillary pressure measurements have been applied for decades in the study of pore configurations: while the NMR relaxation times of proton spins depend on the size of pores and are used to estimate pore size distribution, capillary pressure is a direct measure of pore throats. The two methods provide complementary information about a porous network yet are largely orthogonal techniques and have never been used together in a single experiment.

In this work, we combine the NMR and capillary pressure techniques on a rigorous theoretical footing and name the new method “PcT2 correlation spectroscopy”. This novel 2D approach, mathematically akin to conventional multidimensional NMR methods, provides pore-specific pore throat distribution, a critical insight on pore connectivity that are chiefly responsible for fluid transportation in a porous medium.

We performed PcT2 spectroscopy on several brine-saturated siliciclastic and carbonate samples, revealing a profound richness of their pore connectivity. For rocks that lack post-depositional modification, we observe a linear pore body-pore throat correlation, where pore size distribution reflects the variance of depositional porosity (Fig. 1A, B, C and Fig. 2A, B). However, post-depositional processes can alter the pore space and lead to highly complex pore body-throat dependences (Fig. 1D, E, F and Fig. 2C, D).

PcT2 is the prime example of combining distinctive physics in a single experiment, bringing in insights that neither technique alone nor a numerical combination of their independent probes could provide. It can be a valuable addition to the geoscientists’ toolkit for describing porosity and its classification, visualizing pore connectivity, and modeling multiphase flow and fluid drainage.

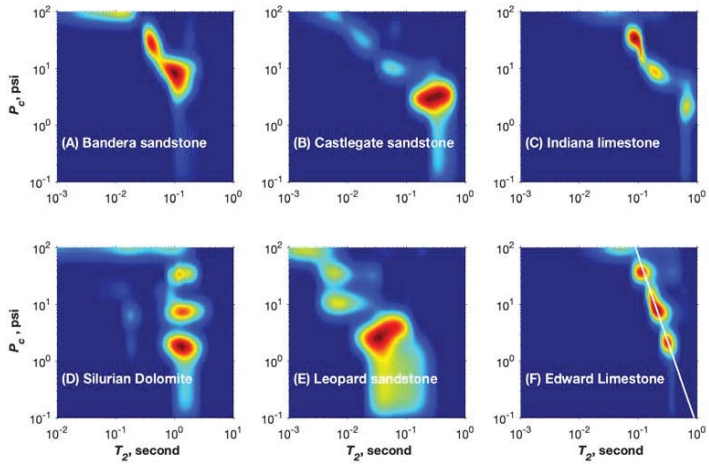

Figure 1. PcT2 maps for several sandstone and carbonate samples. Some sandstones and limestones show a strong PcT2 correlation (A-C), while others exhibit diverse signatures (D, E, F). In F, the white line denotes a correlation of $\alpha = 3$.

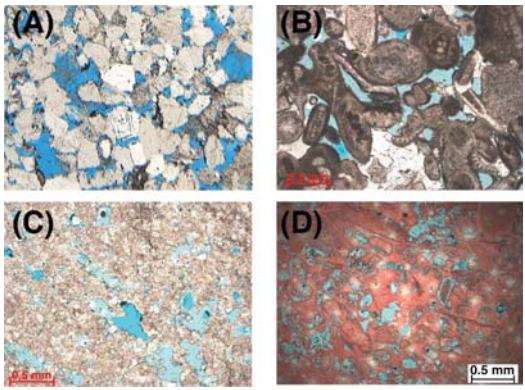

Figure 2. Micrographs of thin-sections of the Berea sandstone (A), Indiana limestone (B), Silurian dolomite (C), and Edwards limestone with red calcite staining (D). Signatures of substantial diagenesis, such as recrystallization, dolomitization and cementation, are observed in (C) and (D).

Unsteady State Relative Permeability Curves Derived from Saturation Data Spatially and Temporally Resolved Using Magnetic Resonance Imaging

M S Zamiri[1], A Afrough[1], F Marica[1], L Romero-Zerón[1] and B J Balcom[1]

[1]University of New Brunswick, Fredericton, Canada

Introduction: Relative permeability (RP) curves describe the displacement of immiscible fluids in rock samples. These curves, ordinarily time-consuming and difficult to measure, are critical for petroleum reservoir management. They help guide decision-making and permit optimal petroleum recovery. Spatial and temporal measurements of fluid content are essential for investigation of displacement phenomena. Pure phase-encoding with SE-SPI [1] provides spatial and temporal proton density of fluids sufficiently precise to permit evaluation of partial derivatives. This quantitative information can be introduced in governing equations for immiscible displacement of fluids to give important properties: capillary dispersion, D_c and oil fractional flow, f_o [2] which contain RP information.

$$\phi \frac{\partial S_o}{\partial t} + v_t \frac{\partial f_o}{\partial S_o} \frac{\partial S_o}{\partial y} = \frac{\partial}{\partial y}\left(D_c \frac{\partial S_o}{\partial y}\right) \quad \text{Eq. 1}$$

Where ϕ is porosity and v_t is total flow rate.

Methods: Displacement of water by oil in Bentheimer sandstones was monitored at 0.2 T with SE-SPI. The MRI profiles were processed to determine RP by: extracting the proton density, converting the data to saturation profiles, S_o (Fig. 1a), calculating saturation partial derivatives (Fig. 1b and 1c), determining flow rate profiles (Fig. 1d), stating all variables as functions of saturation, and finding RP curves by pointwise minimizing the discrepancy of D_c and f_o with the data points. Following this method, capillary dispersion, oil fractional flow, and RPs can be derived versus saturation.

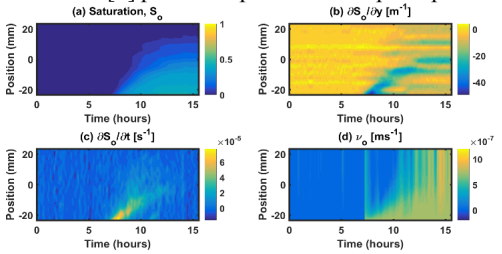

Fig. 1: (a) Oil saturation map and its partial derivatives with respect to (b) position and (c) time. (d) Oil flow rate map for volumetric flow rate, v_t of 0.250 mm^3/s.

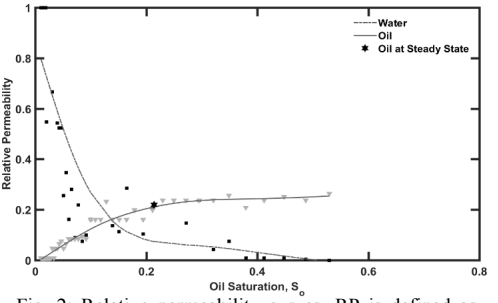

Fig. 2: Relative permeability curves. RP is defined as ratio of effective permeability of a phase in presence of another phase to absolute permeability of the rock.

Results and Discussion: The saturation map, Fig. 1a, shows the importance of capillary forces in retention of water in small pores at the end of the core plug. Derivatives, Fig. 1b and 1c show a slanted feature indicating the evolution of the front in time and space. The shape of the propagating front is influenced by capillary forces, whereas, its velocity is influenced by the mobility and RP of the two phases. The RPs are shown in Fig. 2. As oil saturation increases, the water RP decreases from 1 to zero at $S_o = 0.46$ and oil RP increases to a value notably less than 1, indicating the reduction of effective permeability as a result of presence of another phase. A steady state RP measurement at the end of displacement confirms the prediction of RP curves.

Conclusion: A method has been derived for calculating RP curves based on evolution of saturation profiles. Such curves are very valuable special core analysis measurements, difficult to measure by conventional methods.

References: [1] Petrov, J. Magn. Reason. (2011). [2] Goodfield. SPE. (2001). [3] Bacri, J. Phys. Lett-Paris. (1985).

Investigating liquid displacement in porous media using spatially resolved NMR spectroscopy

H. N. Sørgård, J. G. Seland
Department of Chemistry, University of Bergen, Allegaten 41, N-5007 Bergen, Norway.

Introduction: Paramagnetic impurities in rock materials are causing line broadening ($\Delta\nu$) that obscures the quality of data obtained in high field MRI and NMR [1]. We have created a core model system for spatially localized high field MRI/NMR measurements with high image quality and where liquid signals can be separated due to chemical shift differences. Recently, we showed that correlations between internal gradients (G_0) and differences in magnetic susceptibility ($\Delta\chi$) enable determination of pore size distributions [2, 3]. Furthermore, G_0-$\Delta\nu$ correlations can be used to determine grain size heterogeneities [3, 4]. Here we present results from spatially resolved G_0-$\Delta\chi$ and G_0-$\Delta\nu$ correlations obtained during liquid displacement in samples with varying properties.

Methods: The core model system consists of closely packed NC4X high purity quartz sand (The Quartz Corp). All experiments were conducted on a Bruker Ascend 500MHz vertical wide bore spectrometer equipped with a MicWB40 micro-imaging probe using methods presented in [2, 3].

Results and Discussion: Examples of spatially resolved NMR data obtained from liquids in areas of different grain sizes and wettability are shown in the figures below. The data reveals how these properties of the porous system influence the confinement and dynamic behavior of the liquids.

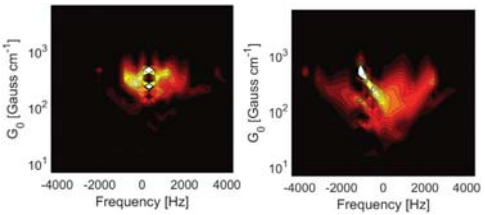

Fig. 1: Spatially resolved G_0–$\Delta\nu$ correlations from areas of different degrees of grain size heterogeneities.

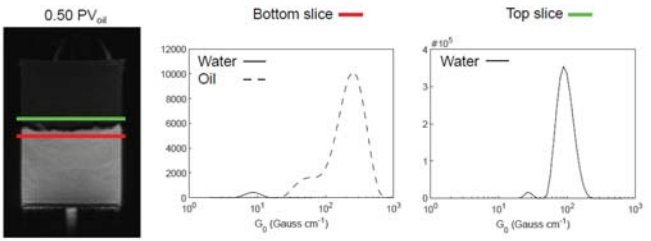

Fig. 2: Examples of spatially resolved G_0 distributions acquired from water and oil signals during oil imbibition in an oil-wet sample. Signals from water and oil are separated due to their differences in chemical shift.

Conclusions: The presented core model system and spatially resolved NMR methods presented reveals detailed information about local confinement during liquid displacement in porous systems.

References: [1] J. Mitchell et al., Phys. Rep, 526, (2013). [2] H. N. Sørgård, J.G. Seland, J. Magn. Reson, 301, (2019). [3] R.T. Lewis, J.G. Seland, Mic. Mes. Mater. 269, (2018). [4] L.M. Burcaw, P.T. Callaghan, J. Magn. Reson. 216 (2012).

Probing the adsorption in microporous materials by hyphenated NMR and physorption

R. Oliveira-Silva[a], *J. Marreiros*[a], *R. Ameloot*[a], *D. Sakellariou*[a]

[a]cMACS, Department of Microbial and Molecular Systems (M²S), KU Leuven, Leuven, Belgium

Abstract: Porosimetry is an important and recurrent analysis in material chemistry characterization. Materials such as metal-organic frameworks (MOFs), mesoporous silicas, and zeolites are typically characterized using gas/vapor adsorption and desorption isotherms.[1,2] Through the controlled partial pressure loading of an evacuated sample volume, this technique determines indirectly qualitative and quantitative properties of the pore environment, like BET surface area and pore volume, with limited insight into the quantifiable nature of guest/host interactions. Low-field Nuclear Magnetic Resonance relaxometry (LFNMR) is an experimental technique applied commonly to porous media analysis, able to directly measure the content and physicochemical properties of the porous environment through nuclear spin relaxation of the contained liquid.[3,4] In this work, we present a first account of simultaneous online physisorption and LFNMR for the study of microporous MOFs, with vapors of methanol, ethanol and water at 35 °C. A low cost home-made permanent magnet was designed to be integrated with a commercial physisorption analyzer, without interference. Results show the complementarity of LFNMR to the sorption isotherms by the D_0 and T_2 relaxation time distributions, which scope the nature and specificity of the interactions between different guest molecules and adsorbents. This low-field hyphenated NMR instrumentation demonstrates generality, practicality and versatility **without** the use of superconducting magnets, hyperpolarization techniques, isotopic labeling, nor high-pressure gas intrusion.

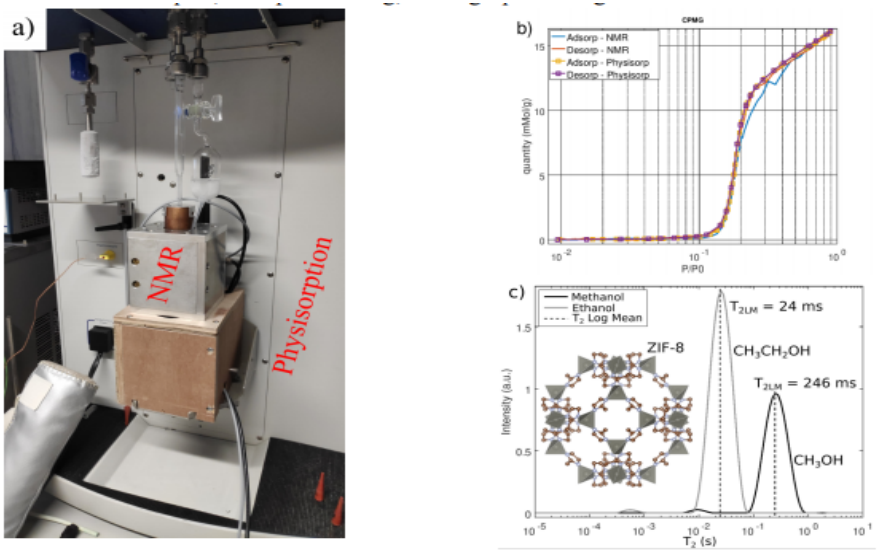

Figure 1 – a) NMR and physisorption hyphenated system. b) Superposition of the simultaneously acquired isotherms with both modalities. c) Different guest molecules present distinct relaxation time distributions when adsorbed by same material.

References: [1] Tu, Adv. Funct. Mater. (2015).[2] Marreiros, Chem. Mater. (2019). [3] Judeinstein, J. Mag. Reson. (2017). [4] D'Agostino, Chem. Eur. J. (2014).

Mapping pore-scale flow heterogeneity in rock with 3D spatially-resolved propagators acquired using compressed-sensing APGSTE-RARE MRI

D.W. de Kort[a], K. Karlsons[a], M. Appel[b], M.D. Mantle[a], A.J. Sederman[a], L.F. Gladden[a]
[a]Magnetic Resonance Research Centre, University of Cambridge, UK, [b]Shell Technology Centre Amsterdam, The Netherlands

Introduction: This work demonstrates the acquisition of spatially-resolved flow propagators in porous carbonate rocks at pore-scale spatial resolution (100 μm), and the way in which they can be used to look at flow and dispersion processes at a pore scale. Measurement of flow propagators is one of the most powerful and comprehensive tools for characterising these phenomena, as they contain information about self-diffusion, flow, and dispersion [1]. Carbonate rocks are typically structurally heterogeneous across a wide range of length scales, ranging from the micrometre (pore) scale through the centimetre (rock core plug) scale to the field scale. Understanding flow and dispersion processes in such rocks is critical for the improvement of enhanced oil recovery and carbon sequestration technology.

Methods: A novel under-sampling APGSTE-RARE MRI experiment for 3D spatial resolution of flow propagators was implemented. [2,3] We have previously demonstrated that, from ~10% sampled data, spatially-resolved propagators can be recovered artefact-free [3–4] through a compressed sensing [5] approach that imposes sparsity in the reconstruction. In this work, the method was used to acquire propagators of creeping flow through 4-mm diameter rock plugs at an isotropic voxel resolution of 100 μm (acquisition time 2 days). 192,000 local propagators were obtained within each rock sample. The experiments were carried out on Ketton and Estaillades, both of which are carbonates, but with very different microstructures. The observation time (Δ) and flow rate were varied in order study local fluid mixing processes.

Results and discussion: At a spatial resolution of 100 μm, pore-scale features could be seen in the spatially-resolved propagator. This made it possible to co-align the data with X-ray μCT images of the same rocks, which visualise the pore and grain space at a much higher spatial resolution (~5 μm), thereby aiding in the interpretation of the MRI data in terms of the microstructural features of the pore space. The spatially-resolved propagators (Δ=150 ms) were then used to segment the pore space into stagnant and flow-carrying components. It could be seen that localised flow channels formed within the rocks, whilst the largest amount fluid was not associated with a significant flow rate. To observe mixing between the flowing and stagnant fluid components, additional spatially-resolved propagators were acquired at a longer observation time of 900 ms. By looking at individual propagators at the per-voxel level, the effect of mixing between the different components could be seen.

Conclusion: It was shown that 3D spatially-resolved propagators reveal significant heterogeneity of the flow field in carbonate rocks. At 100 μm spatial resolution, pore-scale features could be discerned in the spatially-resolved propagators, allowing co-registration of the MRI data with X-ray μCT images of the same rocks. A segmentation of the pore space then revealed which of the pores carry flow and in which pores the fluid is stagnant. An analysis of individual individual, per-voxel propagators revealed local mixing processes as a function of observation time Δ.

References: [1] Manz, AIChE J. (1999). [2] Scheenen, J. Magn. Reson. (2001). [3] de Kort, J. Magn. Reson. (2018). [4] Ramskill, Transp. Porous Med. (2018). [5] Lustig, Magn. Reson. Med. (2006).

Pore Size from Multimodal Features of Relaxation Times

A. Afrough[1,3], *S. Vashaee*[1], *L. Romero-Zerón*[2], *F. Marica*[1], *B.J. Balcom*[1]
[1]MRI Research Centre, University of New Brunswick, Fredericton, Canada,
[2]Department of Chemical Engineering, University of New Brunswick, Fredericton, Canada,
[3]Centre for Oil and Gas – DTU, Technical University of Denmark, Kgs. Lyngby 2800, Denmark

Introduction: T_1 and T_2 measurement methods cannot directly determine pore size. The exact relationship is problematic because of the sample-dependent proportionality constant between T_1 and T_2 and pore size. We establish that nonground eigenmodes contribute to relaxation in common measurements and exploit multimodal features of relaxation to extract average pore size in bulk and spatially-resolved magnetic resonance measurements.

Methods: $T_1 - T_2$ measurements [1] were undertaken for seven rock samples and four glass-bead packs. In addition to bulk measurements, 1D profiles were acquired by Inversion Recovery-prepared Spin Echo Single Point Imaging (IR-SESPI) as a new imaging method. IR-SESPI is composed of two encoding segments of (a) inversion recovery and (b) CPMG echo train, where phase-encoding gradients are applied between the 90° pulse and the first 180° radiofrequency pulse of the CPMG segment. The measured signal $m_+(\tau_1, \tau_2)$ was transformed into a relaxation correlation function $I\ T_{1,p}, T_{2,q}$ from which diffusion-relaxation modes were identified. The regularization parameter α in the inversion method of [2] was varied to aid the detection of nonground modes [3]. A direct search optimization method [4] found the average pore size l and surface relaxivities, ρ_1 and ρ_2, by reproducing eigenmodes detected in $I(T_{1,p}, T_{2,q})$ according to the Brownstein-Tarr solution [5].

Results and Discussion: By logarithmically reducing α, higher eigenmodes of large $L11$ and small $S11$ pores of Indiana limestone appear at $\alpha = 0.1$, as shown in Fig. 1.The estimated average pore size for large and small pores was respectively 39.6 μm and 10.0 μm versus SEM sizes of 50 μm and 10.1 μm.

Imbibition of NaCl solution in air-saturated Berea was measured by the IR-SESPI pulse sequence with 16 k-space points at $B_0 = 0.05$ T. Analysis for each point in the image space demonstrated a reduction in the pore size from 30 μm at the inlet end of the sample to 19 μm at the outlet end. The reduced apparent pore size is due to partially liquid-filled pores in the core plug. Similar analysis was successfully extended to bulk and spatially-resolved measurements in other samples and processes.

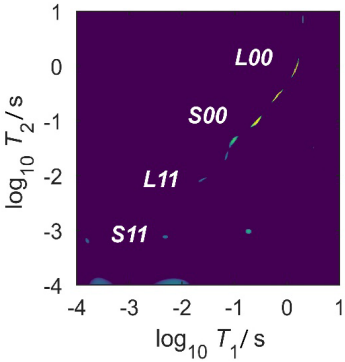

Fig. 1: Nonground relaxation eigenmodes for large $L11$ and small $S11$ pores appear by reducing the regularization parameter to 0.1.

Conclusion: Nonground eigenmodes are commonly disregarded in the data analysis of magnetic resonance in porous media, even though they have been described for decades. This work clearly demonstrates that nonground eigenmodes contribute to magnetic resonance relaxation measurements. Multimodal features of T_1 and T_2 were employed to estimate the average pore size. This finding enables reprocessing of a large body of extant experimental data and permits the development of new imaging methods that directly measure pore size.

References: [1] Song, Venkataramanan, Hürlimann, et al. J. Magn. Reson. (2002). [2] Venkataramanan, Song, Hürlimann, IEEE Trans. Signal Process (2002). [3] Afrough, Vashaee, Romero-Zerón, Balcom, Phys. Rev. Appl. (2019). [4] Kolda, Lewis, Torczon, SIAM Rev. (2003). [5] Brownstein, Tarr, Phys. Rev. A (1979).

Hardware

Chair: Eiichi Fukushima

The Iseult 11.75T whole-body MRI magnet

Lionel Quettier
Institut de recherche sur les lois fondamentales de l'univers (IRFU)
CEA, Saclay, France

An innovative Whole Body 11.7 T MRI magnet, as part of the Iseult/Inumac project, a French-German initiative focused on very high magnetic-field molecular imaging, is under commissioning at NeuroSpin.
The Iseult/Inumac magnet is an actively shielded magnet manufactured from NbTi superconductor. It will generate a homogeneous field of 11.75 T within a 90 cm warm bore and it is operated at a current of 1483 A, in driven mode, in a bath of superfluid helium at 1.8K. After 6 years of fabrication, the magnet was delivered at Neurospin in May 2018.
After an introduction of the magnet design, this talk will present the main steps of the fabrication, the preparation of the cryogenic and electrical facilities and it will finally present the commissioning status of the magnet and of the ancillary equipment.

MRI at 2.15 MHz in a large-bore Halbach Array

T. O'Reilly, W. Teeuwisse, K. Koolstra, A. Webb
Leiden University Medical Centre, Leiden, the Netherlands

Introduction: Halbach arrays can be used to generate very homogenous magnetic fields if the length-to-diameter ratio is high [1]. However, this presents challenges for their application to human imaging in which the ratio is typically 2:1 or less. In this work we present a new approach for improving the homogeneity of a Halbach array by varying the diameter of the array over its length and use this approach for designing a Halbach-array-based MRI scanner for paediatric neuroimaging.

Methods: The Halbach array is constructed from 23 layers of 12 mm cuboid N42 neodymium magnets, each layer consisting of 2 rings of magnets (see figure 1a) with a total magnet length of 50.6 cm. The radius of the rings in each layer was varied to optimise the homogeneity over a 20 cm diameter sphere using a genetic algorithm. B_0 maps were acquired using a Hall-probe attached to a measurement robot [2]. Shimming was performed using 3 mm cuboid magnets placed inside the bore using the acquired B0 map as input. Gradient coils were constructed using 1.5 mm diameter copper wire wound on cylindrical formers. A 15 cm diameter, 15 cm long solenoid was used as an RF transceive coil. A 1 kW RF amplifier was designed using MOSFET technology.

Results & discussion: The constructed magnet had a field strength of 50.4 mT and a homogeneity of 13000 ppm over a 20 cm diameter sphere. The homogeneity was improved to 2500 ppm after a single shimming iteration. Images were acquired from a 9×6×3.5 cm 3D printed Shepp-Logan-based phantom filled with aqueous gel. Data were acquired using a 2D spin-echo sequence without slice selection and an in-plane resolution of 1.2×1.2 mm with 8 signal averages and an acquisition time of 16 minutes.Figure 3b shows a reconstructed image of this phantom.

Conclusion: The homogeneity of a Halbach array based magnet can be improved by varying the ring diameter along its length. Initial 2D images have been acquired using this shimmed magnet design. Using custom-built open source hardware it should be feasible to produce a MR system for less than 30000 euros for paediatric neuroimaging in low-resource settings.

References: [1] Turek, J. Magn. Reson. (2014). [2] Han, Sci. Rep. (2017).

Acknowledgement: This work is supported by the following grants: ERC Advanced NOMA-MRI 670629, H2020 FET OPEN 6626550 and the Simon Stevin Meester 2017 award.

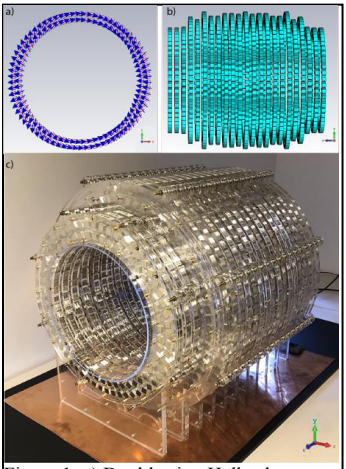

Figure 1. a) Double-ring Halbach configuration used to increase B_0 strength. b) Side-view of the Halbach array optimised for homogeneity. c) The constructed Halbach array with a bore diameter of 27 cm, wide enough to be used for paediatric neuroimaging. The cost of the magnet was 4000 euros.

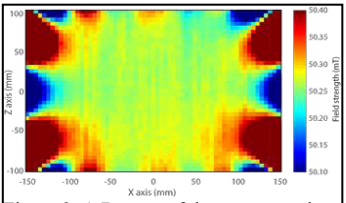

Figure 2. A B_0 map of the constructed magnet after shimming. Homogeneity over a 20 cm diameter spherical volume was 2500 ppm.

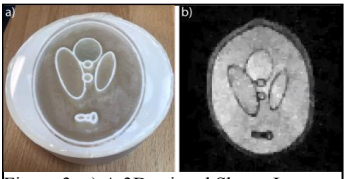

Figure 3. a) A 3D printed Shepp-Logan based phantom, the lines separating the compartments are 1 mm thick. b) Images acquired using a spin echo sequence and reconstructed using a standard Fourier transform.

Parallel-Plate Resonator for MRI studies of lithium ion batteries.

Andrés Ramírez Aguilera[1,2], *Bryce MacMillan*[1], *Sergey Krachkovskiy*[3], *Gillian R. Goward*[3] and *Bruce J. Balcom*[1]

[1]UNB MRI Centre, Department of Physics, University of New Brunswick, Fredericton, New Brunswick, Canada, [2]Centro de Biofísica Médica, Universidad de Oriente, Patricio Lumumba s/n, Santiago de Cuba, Cuba, [3]Department of Chemistry, McMaster University, Hamilton, Ontario, Canada.

Introduction: Magnetic Resonance Imaging studies of Lithium-ion batteries are challenging because metal structures of the battery assembly may shield the B_1 field and distort the static field B_o while the low sensitivity of lithium impairs SNR [1,2]. We present an optimized RF parallel-plate resonator [3] for MRI studies of lithium-ion batteries. The probe produces a $\mathbf{B_1}$ field parallel to the electrodes of the lithium ion cell avoiding RF shielding. The lithium ion battery may be introduced to the RF probe as a cartridge type cell, which is recognizable as a battery, unlike most cells employed for MR/MRI studies.

Fig. 1: Prototype of the parallel-plate resonator employed for MRI studies of lithium-ion cells. The B_1 field is oriented along x with B_o z directed. MRI profiles are generated along y.

Methods: The parallel-plate resonator was designed and optimized with CST MicroWave Studio. A pure phase encode $\mathbf{B_1}$ mapping method [4] was employed to evaluate the $\mathbf{B_1}$ homogeneity of the parallel-plate resonator. Double half k-space (DHK) spin echo (SE) [5] was employed to acquire 1D profiles of the electrolyte solution between the plates of lithium-ion batteries. All experiments were performed on a 2.4T horizontal bore superconducting magnet with a maximum gradient strength 27.6 G/cm

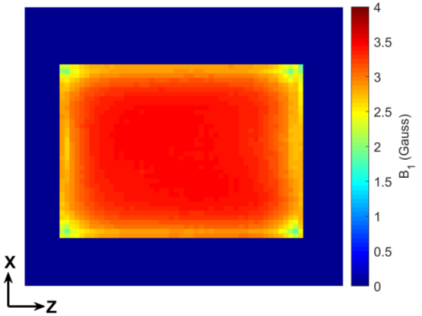

Fig. 2: $\mathbf{B_1}$ mapping of the parallel-plate resonator with distributed capacitance.

Results and discussion: The probe produce a strong and homogeneous $\mathbf{B_1}$ magnetic field parallel to the plates avoiding shielding of the RF signal due to the electrodes of the lithium-ion cell. All experimental results agreed within 20% with simulation results. The sample is sandwiched between the plates maximizing the sensitivity of the probe. 1D profiles of lithium ion concentration inside the cell shows that the parallel-plate probe can be used for *in situ* lithium ion cell studies.

Conclusion: A parallel-plate resonator design was optimized using distributed capacitance increasing the $\mathbf{B_1}$ homogeneity and increasing the $\mathbf{B_1}$ magnetic field strength. 2D images and $\mathbf{B_1}$ maps showed that the experimental results agree with the simulation. A prototype was built and tested to study a functional lithium ion battery.

References: [1] Krachkovskiy SA, *et al*. Journal of Physical Chemistry C (2018). [2] Klamor S, *et al*. *Phys Chem Chem Phys* (2015). [3] Ramírez Aguilera A, *et al.* Concepts Magn Reson Part A (2019). [4] Vashaee S, , *et al*. J Magn Reson (2013). [5] Ouriadov AV., *et al.* J Magn Reson (2004).

Continuously Adjustable Passive Shims

Andrew F. McDowell, Fred W. McDowell
NuevoMR, LLC, Albuquerque, NM, USA

Introduction: Traditional passive and active shims have complementary properties. Passives can create strong fields and operate without requiring power and dissipating heat, but their correction fields are fixed once they are constructed and installed. Actives provide continuous adjustability in situ, but their fields are weak. In many applications, the passive shims are intended to correct the majority of the field errors due to magnet imperfections and perhaps due to the probe structure. The actives are utilized for fine corrections of these errors, and to account for variations due to temperature changes, differences between samples, etc. We have developed an approach [1] to passive shimming in dipole magnets that allows the shims to have full, continuous adjustability, without removing the shims from the magnet.

Methods The new approach is possible because the passive shim structures that generate harmonic correction fields come in pairs, for example X and Y, YZ and YZ, XY and X^2-Y^2. The members of each pair are identical in structure and differ only in orientation (Fig. 1). To achieve adjustability, we build both members of a given pair using full-strength magnetic material, such a magnetic ink, and then manipulate the orientations of the pair members to achieve any value of the total correction field produced by the pair's members. For example, any linear field in the X-Y plane may be produced by reorienting the "X" and "Y" shim elements We have demonstrated the viability of this method by building shims for a 0.5 T magnet and mounting them so that they may be rotated around a fixed axis without removing them from the magnet. The fields produced by the shims were mapped using a computer-positioned NMR probe.

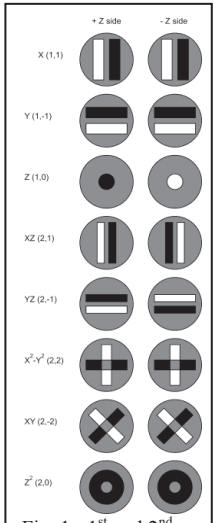

Fig. 1: 1st and 2nd order passive shim structures.

Results and discussion: Data demonstrate that, for each pair of harmonic fields, it is possible to produce any desired strength and orientation of the total correction field, up to the maximum field produced by the passive shim structures. We also demonstrate design control of the produced shim field by calculating orientations needed to produce particular results, for example, the spiral of Archimedes in the X-Y plane shown in Fig. 2. We have also used the adjustable shims to correct the magnet used for this work.

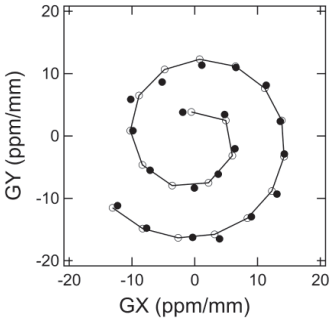

Fig. 2: Calculation and production of desired passive shim fields.

Conclusion: For applications using dipole magnets, we have demonstrated that it is possible to endow strong passive shims with the adjustability usually associated with active shims. The key is to construct passive shims that produce harmonic fields and then manipulate them in pairs by adjusting their orientations. It is possible to make the adjustments in situ, without removing the shims from the magnet. The method also allows the mass production of passive shims (as is currently possible with active shims), with the shims later being adjusted for the idiosyncrasies of individual magnets.

References: [1] McDowell, *J. Magn. Reson*. **296,** 143 (2018).

Magnetic Particle Imaging using Toroidal Vortex Rotation of Halbach Rings

P. Vogel [a], *M.A. Rückert* [a], *M. Dahsler* [a], *H. Brand* [a], *T. Kampf* [b], *V.C. Behr* [a]

[a] Experimental Physics 5 (Biophysics) Universität of Würzburg, Germany

[b] Diagnostic and Interventional Neuroradiology, University Hospital Würzburg, Germany

Abstract: Magnetic Particle Imaging (MPI) is a promising imaging technique utilizing time-varying magnetic fields to determine the distribution of superparamagnetic iron-oxide nanoparticles (SPIONs). Instead of using electrical coils for the generation of required magnetic fields, a novel approach with rotatable Halbach rings is introduced.

Introduction: MPI is a novel imaging modality for direct visualization of SPIONs. It relies on the nonlinear magnetization response of SPIONs on time-varying magnetic fields. For imaging and determining the SPION distribution, a field free point (FFP) created by a strong gradient is steered through the field of view (FOV) to scan the entire volume point-by-point for [1]. Multiple MPI scanner approaches were introduced, where most are using electrical coils for the generation of fast-moving gradient fields [2]. To reach a higher signal-to-noise ratio (SNR), MPI scanner concepts utilizing permanent magnets, such as Halbach rings [3, 4], has been demonstrated. Halbach rings are used in nuclear magnetic resonance (NMR) devices to generate strong and highly homogeneous magnetic fields without the need of electrical power [6]. To transfer the approach to MPI, configurations generating strong gradients have been found [4, 7].
In this abstract, a novel approach for Traveling Wave MPI scanners (TWMPI) [5] using mechanically rotating Halbach rings is shown.

Methods: For a mechanical TWMPI scanner, two coaxial Halbach rings (k=0 configuration) performing a synchronous vortex ring rotation with a phase shift of 90 degree are assembled in a distance d. This synchronous rotation with frequency f_1 generates an FFP moving along the symmetry axis of the scanner (see Fig. 1 top).
Two additional Halbach rings with k=1 configuration, which counter-rotate along the z-axis with frequencies f_2 and f_3, are utilized to move the FFP along a spiral trajectory through the FOV (see Fig. 1 bottom).

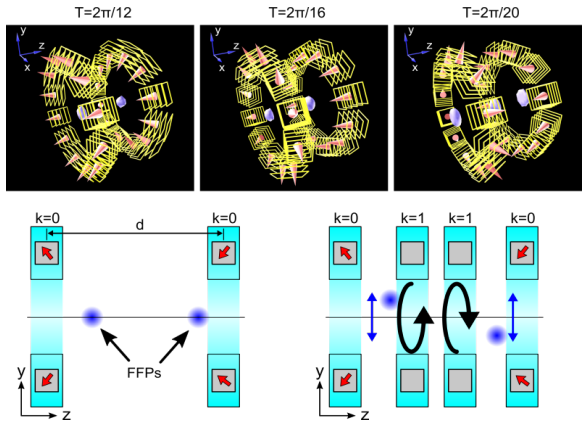

Figure 1: Top: The time series above shows the rotation of the Halbach rings at different times points. The red arrows indicate the direction of each magnet, the blue area represents the area with lower magnetic fields: field free points (FFP). **Bottom left:** cut through the rings (k=0) generating the traveling FFPs along the symmetry axis. **Bottom right:** additional Halbach rings (k=1) rotating around the z-axis steer the FFPs along a spiral trajectory through the FOV.

Discussion and Conclusion: A fully mechanically driven Traveling Wave MPI scanner approach covering a full 3D volume is presented. Building all gradients of the MPI system from permanent magnets allow for high gradient fields combined with low energy consumption.

References: [1] Gleich & Weizenecker, Nature (2005). [2] Knopp, PMB (2017). [3] Halbach, Nucl Instr Meth Phys Res (1980). [4] Bagheri, Appl Phys Lett (2018). [5] Vogel, IEEE TMI (2015). [6] Raich & Blümler, NMR Mandhalas (2004). [7] Vogel, Nature Sci Rep (2019).

NMR with a fast-moving coil array

Irfan Bulu, Shin Utsuzawa, Tancredi Botto, Jeffrey Paulsen, Lalitha Venkataramanan, Martin Hurlimann, Yi-Qiao Song
Schlumberger-Doll Research, Cambridge, MA 02139

NMR is typically performed with the detector and sample in a fixed relative position. In NMR well-logging, however, the tool detector is in constant motion relative to the rock formation sample. The conventional approach is to move the tool slowly. Fast movement causes the sample to move out of the detector coil during the CPMG acquisition and thus increase $1/T_2$. Thus, inclusion of more coils could capture the signal from the escaping portion of the sample. This paper shows a multiple-coil system in order to obtain high quality NMR data at high speeds.

The new system (Fig.1) is constructed with a long magnet array (brown blocks) and four RF coils (gray boxes within the magnet). NMR experiments were performed using a Redstone spectrometer (Tecmag Inc.) with four transmit and receive RF channels.

The 4 right panels show the signals from all coils at different speeds. For the static measurement, the majority of the signal appears at Coil 1 with a slight one from Coil 2. Coils 3 and 4 are too far away and thus no signal. At a 300 m/hr speed, the Coil 1 signal decays noticeably faster than the static case. The more interesting observation is the Coil 2 signal starts to rise, instead of decay. For higher speeds, for example 600 m/hr, the Coil 2 signal rises first and then falls as the sample moves further out of Coil 2. Also Coil 3 starts to observe signal after ~1 s when the sample enters it. For 900 m/hr, Coil 4 starts to observe signal after 1.5 s when the sample enters its area. Such complex signal behavior can be described by:

$$S^i(\tau) \sim \int dRdT_2\Phi(R,T_2)\exp[-\frac{\tau}{T_2}]G[R-r^i(\tau)],$$

where $G(R)$ is the coil sensitivity function and $r^i(\tau)$ is the position of Coil i at time τ. Using this equation, the multi-coil data can be analyzed to obtain accurate signal amplitude (Φ) as a 2D map of spatial coordinate and T_2. Results from samples of different amplitudes and T_2 obtained at speeds up to 900 m/hr will be discussed.

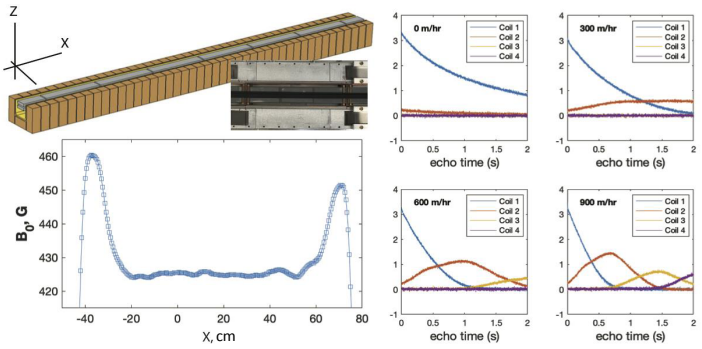

Fig. 1. Left: Magnet and coil arrays; the B_0 field at the sweet spot ~3.8 cm above the coil surface is uniform along the X direction within ± 1.2 G for 70-cm length. The B_1 field were adjusted to be uniform (± 10 %) over all 4 coils (each 17 cm long). **Right**: Signals from a 13-cm long sample starting from Coil 1.

The AVANCE NEO is the next generation of Bruker's successful AVANCE product line. Offering ultra-fast control, greater dynamic range and enhanced flexibility, the AVANCE NEO takes NMR research to an even higher performance level.

For more information please visit: www.bruker.com/neo

Biomedical

Chair: Alexandra Petiet

Mapping hydration water structure and dynamics by Overhauser DNP relaxometry

Song-I Han

University of California Santa Barbara, USA

What are the key surface metrics that control interfacial water dynamics, and thus what are the associated "rules" for programming surfaces to tune their properties? In order to answer these questions, we need to measure the operational surface hydrophilicity and hydration barrier. These are difficult to access metrics, especially on soft material and biomolecular surfaces, and hence are not established. My group introduced equilibrium, single particle, surface water diffusivity as empirical measures of surface hydrophilicity that can be conceptualized as a molecular level "contact angle". Such measurements are enabled by a nuclear magnetic resonance (NMR) relaxometry technique termed Overhauser dynamic nuclear polarization (ODNP) that is sensitive to the diffusivity of water within 1 nm of surfaces, marked by site-specific nitroxide radical spin labels. I will present our ODNP study of amorphous silica surfaces with systematically varying silanol coverage [1], globular protein surfaces with site-specific spin labels [2], and of polymer surfaces with systematically varying hydrophilicity and hydrophobicity, achieved by varying the surface chemistry patterns. The results show how essential it is to consider the impact of heterogeneities in surface chemistry and their spatial patterning on the hydration water structure and dynamics. The significance of understanding the surface programing of hydration water structure and dynamics is that this is expected to reflect on the hydration barrier that tune adsorption and transport properties near the hydrated surfaces. NMR relaxometry, especially in the form of ODNP, is turning out to be a key technique contributing to this important topic.

1. A. M. Schrader, J. I. Monroe, R. Sheil, H. A. Dobbs, T. J. Keller, Y. Li, S. Jain, M. S. Shell, J. V. Israelachvili, S. Han, "Surface Chemical Heterogeneity Modulates Silica Surface Hydration", Proc. Natl. Acad. Sci. U.S.A., (2018) DOI:10.1073/pnas.1722263115.

2. R. Barnes, S. Sun, Y. Fichou, F.W. Dahlquist, M. Heyden, S. Han, Spacially Heterogeneous Surface Water Diffusivity around Structured Protein Surfaces at Equilibrium, J. Am. Chem. Soc., 139 (49) (2017) 17890-17901.

Metabolic assessment of stroked rats using $^{17}O_2$ gas

V.V. Rodin, L. Gallagher, I.M. Macrae, W.M. Holmes
Glasgow Experimental MRI Centre, Institute of Neuroscience and Psychology, College of Medicine, Veterinary and Life Sciences, University of Glasgow, Glasgow, UK

Introduction: The identification of acute stroke patients who will benefit from recanalization treatments (thrombolysis or thrombectomy) remains one of the most challenging aspects for stroke neurologists. Due to the narrow therapeutic time window for recanalization many patients are ineligible for treatment. However, accurate imaging of metabolically viable brain tissue could identify patients that may benefit from these treatments outwith the current time window. The only available method for imaging aerobic metabolism is ^{15}O PET, which is simply not practical for routine clinical use. This work makes the first steps in developing a safe approach based on directly imaging aerobic metabolism using $^{17}O_2$ gas, detected via ^{1}H MRI combined with ^{17}O decoupling.

Methods: Fig.1 shows hardware and software development for ^{17}O metabolic MRI.

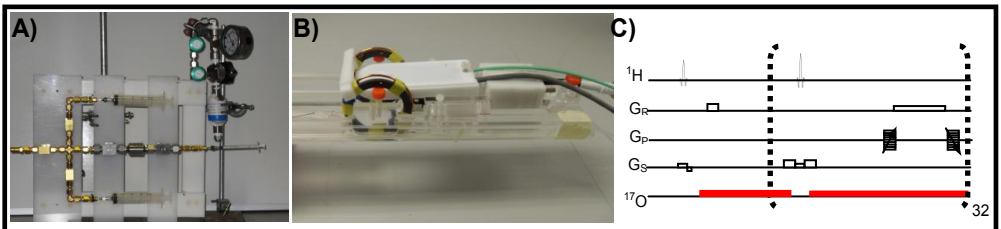

Figure 1. Development work for ^{17}O metabolic imaging. **A)** Gas-rig for saturating oxygen carriers with $^{17}O_2$ gas. **B)** Helmholtz coil for decoupling at ^{17}O resonance, built into the rat cradle and integrated into the MRI electronics. **C)** RARE pulse sequence modified to include ^{17}O decoupling during ^{1}H acquisition.

The metabolic production of $H_2{}^{17}O$ from intravenously delivered $^{17}O_2$ gas is used to directly detect metabolism. Further, the ^{17}O decoupling allows the ^{17}O quadrupole interaction with the bonded ^{1}H to be effectively "switched on" and "switched off" while acquiring the ^{1}H RARE signal using a 300MHz Bruker Biospec.

Results and discussion: MRI of a stroked rat following intravenous injection of $^{17}O_2$ saturated PFC nano-emulsion (Fig.2). (*left image*): T_2 image with decoupling (3 min). (*centre image*): T_2 image without decoupling (3min). (*right image*): Difference image (red overlay), where signal intensity is proportional to the metabolism of $^{17}O_2$ into $H_2{}^{17}O$. The metabolising hemisphere (right) is quite distinct from the non-metabolising stroked hemisphere (left).

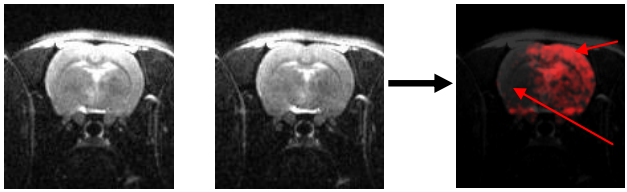

T_2 image, with ^{17}O decoupling

T_2 image, without ^{17}O decoupling

Difference image

Figure 2.

Conclusion:We have demonstrated in an in-vivo stroke model the ability to image the aerobic metabolism of $^{17}O_2$ gas, delivered intravenously via an oxygen carrier (PFC nano-emulsion). Further, we demonstrate the use of ^{17}O decoupling during ^{1}H acquisition.

Creation of a hemodynamic response function for BOLD fMRI in the rat brain

Henriette Lambers, Martin Segeroth, Franziska Albers, Lydia Wachsmuth, Timo Mauritz van Alst, and Cornelius Faber

University Hospital Münster, Münster, Germany

Introduction: A crucial part of functional neuroimaging in the rat is the statistical analysis of the data. For BOLD fMRI the general linear model (GLM) is commonly used with the canonical basis set, where the convolution of the hemodynamic response function (HRF) with the stimulation is included as a model. The software package Statistical Parametric Mapping (SPM) [1] has implemented a canonical HRF by default, which is based on human data (human HRF). Since application of this human HRF may not be appropriate for small animal data, we have determined a generic HRF of rats, based on BOLD responses of the primary somatosensory cortex (S1).

Methods: Data were derived from experiments with SD and Fischer rats under medetomidine or isoflurane anesthesia at 9.4 T with single-shot GE-EPI (TR/TE 1000/18ms, 350x325µm² or 375x375µm², 8-14 1.2 mm thick slices) upon electrical paw, mechanical paw or optogenetic stimulation (block design). Measurements were assigned to 13 different groups according to their experimental conditions (e.g. strain, anesthesia, stimulation). A U-test determined voxelwise whether the signal during stimulation and rest period differed significantly for the S1 region on the activated side of the brain. Signal of significant voxels was summed up. The convolution of the stimulation paradigm and the canonical HRF (eq. 1) was fitted to the resulting time courses.

$$A \cdot e^{-bt} \cdot \left(\frac{b^{p_1}}{\Gamma(p_1)} \cdot t^{p_1-1} - \frac{b^{p_2}}{\mathrm{V} \cdot \Gamma(p_2)} \cdot t^{p_2-1} \right) \qquad \text{eq.1}$$

Time courses of the normalized HRFs for the different groups were compared pairwise, using a customized functional t-test [2]. Resulting p-values were Bonferroni corrected. All HRFs were normalized and averaged across all groups that showed no differences. The canonical HRF (without amplitude *A*) was fitted to the resulting time course of the rat HRF. The resulting parameters can be implemented in SPM. To test the detection performance of the GLM, statistical analysis was performed on 20 datasets with the 1st order canonical basis set using the generic rat or, for comparison, the human HRF. Cluster sizes and t-values were compared using a U-test in SPSS.

Results: BOLD responses of 146 fMRI measurements were extracted and 71 % were fitted successfully. Due to differences between the HRFs of 1 s and 5 s stimulation duration (p=0.07), HRFs obtained from 1 s stimulation were excluded from the determination of a generic rat HRF. Averaging of the remaining HRFs delivered a generic rat HRF based on 98 BOLD measurements of 64 animals. This HRF deviated substantially from the human HRF (Fig. 1). Analysis of 20 additional datasets using the first order canonical model with the generic rat HRF instead of the human HRF revealed significantly larger BOLD clusters and t-values.

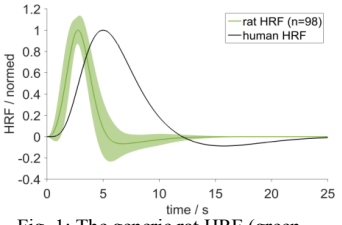

Fig. 1: The generic rat HRF (green, ± standard deviation) deviates from the human HRF (black).

Conclusion: With exception of the stimulation length, the HRF of rats is independent of the experimental conditions examined. Due to the differences between rat and human HRF, the GLM analysis of rodent data showed a significantly higher detection performance using the generic rat HRF. We therefore advise using this generic rat HRF for analysis of rat BOLD fMRI data.

References: [1] Friston, SPM12. Wellcome Trust Centre for Neuroimaging. (2017). [2] Ramsay, Functional Data Analysis with R and MATLAB. 1st ed. Springer. (2009).

Diffusion correlation imaging (DCI) reveals microscopic anisotropy following traumatic brain injury

Dan Benjamini[a,b], *Michal E Komlosh*[a,b], *Elizabeth B Hutchinson*[c], *Peter J Basser*[a]

[a]Section on Quantitative Imaging and Tissue Sciences, NICHD, Bethesda, MD; [b]Center for Neuroscience and Regenerative Medicine, USUHS, Bethesda, MD; [c]Quantitative Medical Imaging Section, NIBIB, Bethesda, MD

Introduction: Diffusion MRI (dMRI) can reveal nervous system pathology in the absence of other MRI signal changes by its sensitivity to the microscale tissue environment, although first-order models such as diffusion tensor imaging (DTI) [1] often cannot provide the specific origin of cellular changes. While conventional dMRI describes water mobility in tissue along different directions, Diffusion-Diffusion Correlation SpectroscopY (DDCOSY) is an MR method that provides correlations between water mobility along different directions [2]. DDCOSY can directly quantify microscopic anisotropy, making it a potentially powerful method to explore white matter (WM) injuries. Here we use the marginal distributions constrained optimization (MADCO) [3] framework to facilitate Diffusion Correlation Imaging (DCI) on healthy and injured ferret spinal cord specimens.

Methods: Two cervical cord sections were selected, one from an uninjured control and the other 1 week following closed head injury (CHI), which resulted in focal corticospinal tract (CST) hemorrhage. Wallerian degeneration was expected along the CST, but not along others. The two specimens were inserted into the same NMR tube, and data were collected using a 10mm coil with a 7T Bruker MRI. DCI data were collected using the double diffusion encoding (DDE) sequence [2]. The diffusion gradients were applied in parallel (z) and perpendicular (x) to the spinal cord axis of symmetry. The MADCO framework was used with a total of 66 acquisitions, and b_{max}=36,000 s/mm^2.

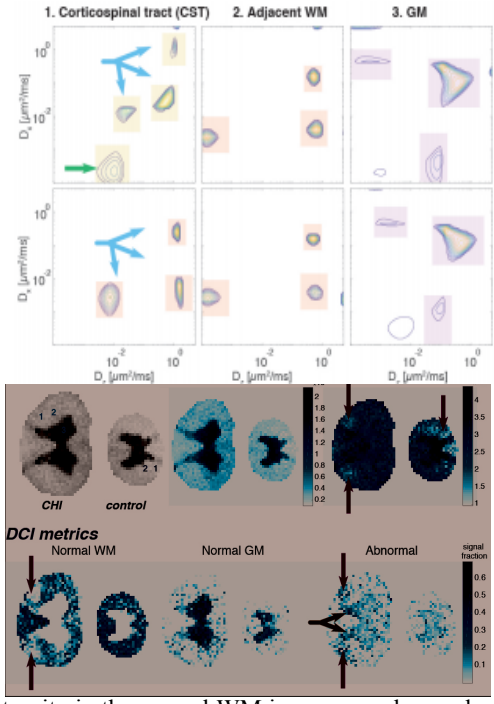

Results and Discussion: No apparent abnormalities were observed on the T_2W, radial diffusivity, or fractional anisotropy images. A reduction in axial diffusivity was observed at the lateral CST of the CHI sample, but also at regions of the control sample (green arrows). Representative diffusion correlation spectra (DCS) from the CST, adjacent WM (AWM), and gray matter (GM) are shown. Normal appearing WM tracts all had similar DCS signatures (red). GM DCS from both control and CHI samples were similar (purple). The DCS of the CHI CST region was unique (yellow); it revealed (1) decreased water mobility in both axial and radial directions (green arrow), along with a (2) shifted three-peak signature that was evident in the control sample (blue arrows). Voxelwise DCS can be used to generate images of specific diffusion components based on their mobility in the radial and axial directions. Normal WM and GM components were identified based on the above DCS signature, which was then used to generate the corresponding quantitative images. A complete absence of signal intensity in the normal WM image was observed at the lateral CST of the CHI sample (green arrows). Similarly, an abnormal component was identified and imaged, where hyperintensities of the CST were observed only in the CHI sample.

Conclusion: The ability of DCI to reveal distinct populations of axons at the site of injury, and in addition, to localize cellular alterations in the GM, suggests potential specificity for microscopic anisotropy caused by traumatic brain injury that led to axonal beading.

References: [1] Basser, Biophys. J. (1994). [2] Callaghan, J. Chem. Phys. (2004). [3] Benjamini, J. Magn. Reson. (2016).

Metabolic rates in red blood cells under shear studied by Rheo-NMR

J. Milius[1], P. W. Kuchel[2], D. Shishmarev[3], S. J. Stevenson[1], T. I. Brox[1] P. Galvosas[1]
[1]MacDiamid Institute for Advanced Materials and Nanotechnology, School of Chemical and Physical Sciences, Victoria University Wellington, Wellington, New Zealand
[2]School of Life and Environmental Sciences, University of Sydney, NSW, Australia
[3]John Curtin School of Medical Research, Australian National University, Canberra, ACT, Australia

Introduction: Red blood cells (RBCs) are responsible for oxygen transport in many living organisms including humans. RBCs experience very different environmental conditions in different parts of the cardiovascular system. In major vessels, blood flow rates are large and mechanical shear stress for RBCs is small to moderate. The opposite is true for blood flowing through arterioles and venules: flow rates drop significantly while shear rates increase and reach values of up to 2000 s^{-1} in healthy humans [1]. Even more mechanical stress and deformation is applied to RBCs in capillaries with diameters that are only half that of an RBC.
It has been shown that mechanical deformation modifies the conversion rate from glucose to lactate in the main metabolic pathway of RBCs [2]. Static compression of RBCs in gelatin gel resulted in an enhancement of the metabolic rate by ~80% [2]. Here we report for the first time that metabolic rate is also enhanced when mechanical stress is applied dynamically through continuous shear at physiological shear rates.
Methods: Rheo-NMR has been used over the last 3 decades as a complementary rheological tool for the study of non-Newtonian and complex fluids [3,4]. We use a cylindrical Taylor-Couette cell adapted for use in a liquid-state high resolution NMR probe in a 400 MHz Bruker Avance spectrometer. The RBC samples were prepared from fresh human blood, under Human Ethics Clearances, as in [2]. Time series of ^{13}C NMR spectra were continuously recorded over 12 h while applying a shear rate of 1005.3 s^{-1}. After 12 h, the shear was stopped while recording spectra continued for another 4 h. Spectra were processed using MestreNova software in which peak integral values were extracted for glucose and lactate plotted against time. Metabolic rates were estimated from the slopes of the progress curves.
Results and Discussion: The rate of conversion of glucose to lactate in the RBCs under shear was 2.1 ± 0.2 mmol [liter RBC]$^{-1}$ h^{-1} while this rate dropped to 0.8 ± 0.1 mmol [liter RBC]$^{-1}$ h^{-1} after shear was stopped. This corresponded to a 2.5-fold enhancement of the metabolic activity in the RBCs under shear, thus confirming that the cells not only respond to static shape distortion but also to mechanical stress imposed by shear flow, as would be present *in vivo*.
Conclusions: We have demonstrated that RBCs respond with changes in their metabolic activity to mechanical deformation caused by shear flow. Shear rates were chosen to be similar to the physiological shear rates that are present in the cardiovascular system of humans. The detected difference in the metabolic rate is consistent with the operation of the mechanosensitive non-selective cation channel PIEZO1 as first seen with static RBC compression in compressed gelatin gels. However, in the latter samples, the RBCs have random orientations with respect to the direction of the strain/stress field, whereas in the rheometer, the alignment is uniform. This accounts for the even greater enhancement (2.5-fold compared with ~0.8-fold) of the metabolic rate under our conditions of uniform shear. The experimental set-up paves the way for studies of cation transport ($^{23}Na^{+}$ and $^{133}Cs^{+}$) in normal RBCs under physiological shear stress conditions and abnormal RBCs such as in sickle cell anaemia and malaria. In turn, this will improve our understanding of the fundamental biophysics of shape and volume regulation by cells in normal and disease states.
References: [1] Sakariassen, *Future Sci*. OA **1** (2015). [2] Kuchel, *Sci. Adv*. **3**, eaao1016 (2017). [3] Callaghan, *Rep. Prog. Phys*. **62** , 599-670 (1999). [4] Galvosas, *Mag. Reson. Chem*. DOI: 10.1002/mrc.4861 (2019)
JM acknowledges financial assistance from Bruker. PWK, DS and PG are supported by ARC DP190100510

Quantitative Mapping of Fatty Acid Composition using Free-Breathing Spectroscopic Imaging with Compressed Sensing

M. Hewlett[1], *C. Davis*[2], *D.P. McAllindon*[2], *C.V. Bowen*[1,2], *K.D. Brewer*[1,2], *S. Clarke*[1,2], *S.D. Beyea*[1,2], and *J.A. Rioux*[1,2]

[1]Dalhousie University, Halifax, Canada, [2]Biomedical Translational Imaging Centre, Halifax, Canada

Introduction: Non-alcoholic fatty liver disease (NAFLD) is a common health concern. Research using single voxel MR spectroscopy has shown that fat composition in the liver may be important in characterizing NAFLD [1]. MR spectroscopic imaging (MRSI) approaches can provide a spatially resolved measure of this composition information with improved spatial coverage, but are limited by slow acquisition times. In this work, a free-breathing MRSI acquisition based on spin echo single point imaging (SE-SPI), accelerated using blind compressed sensing (CS), was used for quantitative mapping of fatty acid composition.

Methods: CS SE-SPI was validated using set of pure oil and oil/water mixture phantoms and evaluated in an *in vivo* mouse study (N=16), with PRESS voxels acquired for comparison in both cases. Mice were split into four groups; fatty livers were induced in half of the mice using a methionine choline deficient (MCD) diet, and iron overload simulated in half of the mice by iron injection. Three fatty acid composition metrics were considered; unsaturation index (UI), a surrogate unsaturation index (UIs), and polyunsaturation index (PUI), as described in [1].

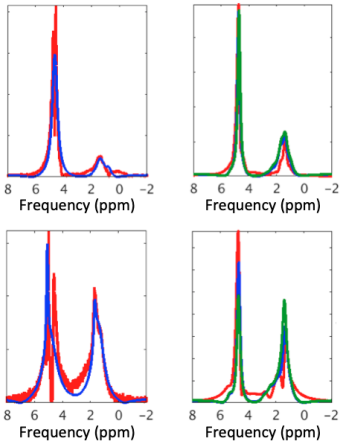

Fig. 1: Typical spectra in MCD mice, with (top row) and without (bottom row) iron injections. Left – spectra acquired with PRESS (shown in red is the raw spectrum, in blue the phased HSVD fit). Right – spectra acquired with CS SE-SPI (shown in red is the raw spectrum of a 3x3x3 sub-volume, in blue the phased HSVD fit of that sub-volume, in green the phased HSVD fits averaged over the entire liver).

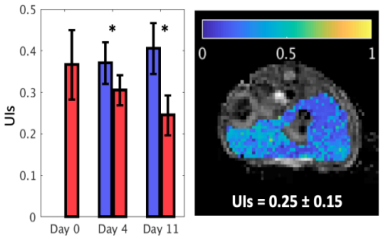

Fig. 2: Left – UIs as measured using CS SE-SPI showed a significant decrease ($p < 0.05$ using Welch's t-test) in the MCD group (red) as compared to the control group (blue) on days 4 and 11 following the start of the diet; error bars indicate 95% confidence intervals. Right – CS SE-SPI and corresponding map of UIs in the liver of one of the mice on day 11 of the MCD diet (value indicated is mean ± sd).

Results and Discussion: Phantom results showed good agreement between PRESS and CS SE-SPI. In the mouse study, PRESS measurements of fat composition were limited by increased line width and peak splitting (see Fig. 1), likely a result of large voxel size and lack of respiratory compensation; as such, no trends were observed. CS SE-SPI showed no significant trends in UI or PUI; however, a significant decrease in UIs was observed in MCD mice (see Fig. 2), in agreement with literature results [2].

Conclusion: This work demonstrates that CS SE-SPI can provide reliable maps of fatty acid composition. If accurate fatty acid profiles could be acquired clinically it would allow researchers to investigate the hypothesized role that differing profiles might play in liver disease.

References: [1] Johnson *et al.*, Hepatology (2008). [2] Li *et al.*, J. Biol. Chem. (2009).

80 MHz Benchtop NMR Spectroscopy

Never Wait for Your NMR Spectra

80 MHz **Spinsolve** yields high quality spectra in your lab & ensures immediate NMR results

Proton, Carbon, Phosphorus and Fluorine options. 1D & 2D sequences

+49 241 92787270

sales@magritek.com

go.magritek.com/80

magritek

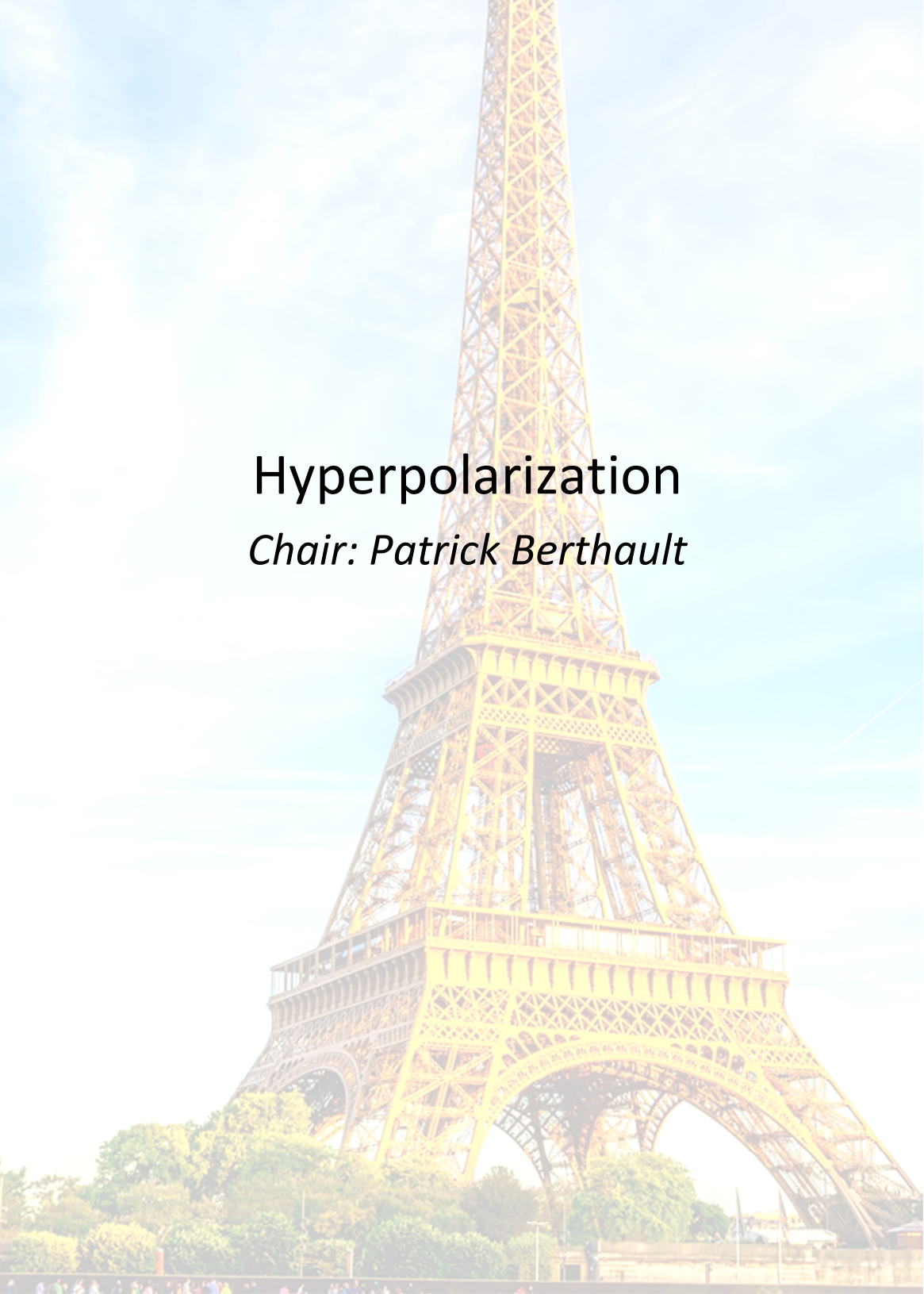

Hyperpolarization

Chair: Patrick Berthault

Progress towards molecular-MRI with Signal Amplification by Reversible Exchange (SABRE) Hyperpolarisation

W. Iali[1], S. S. Roy, F. Ahwal[1], B. J. Tickner[1], E. J. Fear[1], M-C. Labarthe[1], M. Kaestner[1], P. J. Rayner[1], P. M. Richardson[1], A. J. Kennerley[1], A. M. Olaru[2] and S. B. Duckett[1]

[1]Centre for Hyperpolarisation in Magnetic Resonance, University of York, York, YO10 5DD, UK, [2]Siemens Healthcare GmbH, Erlangen, Germany.

- **Introduction:** Magnetic Resonance Imaging (MRI) is a widely used non-invasive method that uses the water pool as a diagnostic indicator of anatomy and function. However, the small thermal population difference between the quantum spin/energy states (polarization) makes it inherently insensitive, relying on the high abundance of water. The comparative low abundance of bio-molecules involved in cellular biochemistry limits the functionalisation of this important imaging technique. Hyperpolarised MR is an emerging method which meets this demand, generating short term increases in polarization, to enable the monitoring of molecular metabolism in health and disease through previously-inaccessible biochemical pathways.

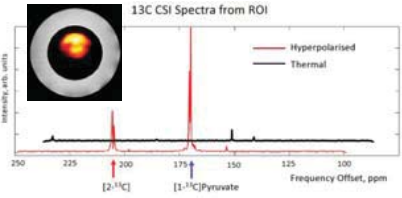

Fig. 1: Hyperpolarized pyruvate response taken from a ROI in a ^{13}C CSI image of a phantom recorded at 9.4 T

The most common of these hyperpolarization methods is Dynamic Nuclear Polarisation (DNP), which is taking pyruvate through clinical trials associated with the diagnosis and treatment of cancer.[1] Here, we communicate progress using Signal Amplification by Reversible Exchange (SABRE) towards MRI applications. SABRE increases measurable hyperpolarisation levels in a wide range of molecules in seconds *via* catalysis and without expensive hardware.

- **Methods:** Molecular targets are brought into indirect contact with *para*hydrogen[3] *via* an Iridium catalyst during hyperpolarization transfer over 10-30 seconds in an optimal field (e.g. 60 mT for ^{1}H nuclei) to create the improved NMR and MRI response. MRI measurements are made across a range of relevant field strengths (3 - 9.4T) using both clinical Siemens (Prisma) and high field Bruker (BioSpec) imaging hardware. Measurements utilize standard (RARE, FISP & FLASH) and spectroscopic (CSI & EPSI) imaging pulse sequences for ^{1}H and ^{13}C nuclei. *In-vivo* detection of SABRE polarized molecular agents is demonstrated at 7T (Bruker Biospec 70/30) in a rodent model where a 2.5 ml bolus (10 mg/ml) is infused into the sub-cutaneous space for detection.
- **Results and discussion:** Results are presented to show how SABRE can improve the MR detection of a variety of agents including nicotinamide, methyl-nicotinate, pyruvate, glucose and urea.[2,4] We also harness the power of SABRE to create a long lived spin isomer of pyruvate and show that its signals can be seen five minutes after the initial hyperpolarisation step (Fig. 1). These developments may lead to future applications where pyruvate hyperpolarisation can be used clinically in conjunction with this rapid and potentially low-cost delivery route. Although, functioanlisation has been proven, current key objectives to realize this technology *in-vivo* include increasing polarisation in bio-compatible solvents and complete de-gassing of hydrogen from the samples.
- **Conclusion:** This talk establishes that with further development SABRE could become a valuable weapon for metabolic monitoring, producing the hyperpolarized responses needed to enable *in vivo* MRI.

References: [1] Nelson, et. al. Sci. Trans. Med., (2013) 5, 10. [2] Adams, et al., Science, (2009) 323, 1708. [3] Bowers, et al., Phys. Rev. Lett., (1986), 57, 2645. [4] Iali, et al., *Sci. Adv.*, (2018), 4. eaao6250.

Hyperpolarized parahydrogen based MRI: SLIC-SABRE and catalytic reactors imaging

A. I. Svyatova[1, 2], E. V. Pokochueva[1, 2], E. S.Kononenko[1, 2], I. V. Skovpin[1, 2], N. V. Chukanov[1, 2], K. V. Kovtunov[1, 2], I. V. Koptyug[1,2]

[1]International Tomography Center SB RAS, Novosibirsk, Russia, [2]Novosibirsk State University, Novosibirsk, Russia

In Situ MRI of Heterogeneous Catalytic Hydrogenation with and without Hyperpolarization: Magnetic resonance imaging (MRI) is a powerful technique to characterize reactors in situ. However, low spin density for gas phase reactions and magnetic field inhomogeneity caused by the presence of a solid catalyst are challenging for MRI. Parahydrogen (p-H_2) induced polarization (PHIP) can significantly increase NMR signal. Here, we present a new type of catalytic reactors for MRI that allows to visualize distribution of gas flow utilizing PHIP, but also suitable for imaging of thermally polarized gases. MRI study of propene hydrogenation was done using FLASH (fast low angle shot) pulse sequence [1]. The stack of 2D slices obtained by MRI was transformed into 3D model (Fig. 1). However, catalyst is non-uniformly located on the reactors surface. Products formation occurs only near catalytically active regions. Therefore, MRI can be used for the characterization of the reactors structure. In addition, reactions of 1,3-butadiene and propyne hydrogenation were investigated. The 1D maps of reagents and products distribution along the system were imaged using spin-echo pulse sequence. In conclusion, the structure of the reactors and compounds distribution along the system were obtained due to the high stability and the fabrication simplicity of the reactors.

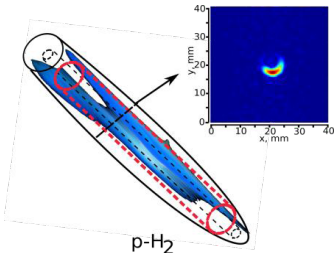

Fig. 1: 3D model of the gas flow. The black solid line shows the edges of the NMR tube, the red dashed line - the reactor, the black dashed line - the capillary.

^{15}N MRI of ^{15}N-labelled and non-labelled biomolecules using SLIC-SABRE: Signal amplification by reversible exchange (SABRE) is another hyperpolarization method based on p-H_2. It allows to obtain hyperpolarized substrate without any structural transformation. The use of ^{15}N nuclei for imaging can extend the application of MRI in biomedicine because of no background signal from ^{1}H nuclei during in vivo studies and longer T_1. For polarization transfer from ^{1}H to ^{15}N we used SLIC-SABRE pulse sequence. ^{15}N MRI of ^{15}N-pyridine (^{15}N-Py), ^{15}N-nicotinamide (^{15}N-NA, vitamin B_3), 4-aminopyridine (fampridine) and dimethylaminopyridine (DMAP) was done using single point imaging (SPI) or FLASH. It should be noted that fampridine is a drug, which cures the symptoms of multiple sclerosis. We compared the effectiveness of two imaging pulse sequences utilizing ^{15}N-Py and ^{15}N-NA [2]. FLASH pulse sequence provides the shorter imaging time, while SPI provides the higher spatial resolution. However, for the future applications, it is better to decrease imaging time, therefore, FLASH pulse sequence was chosen for MRI of non-labelled compounds (Fig. 2). The high level of ^{15}N polarization (≈8 %) allowed to do ^{15}N MRI of biomolecules with natural abundance of ^{15}N for the first time.

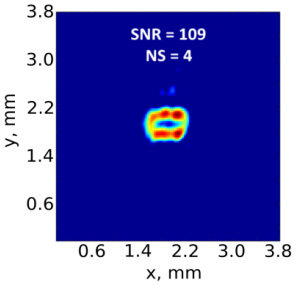

Fig. 2: ^{15}N FLASH MRI of fampridine. The void in the center corresponds to the presence of the capillary supplying p-H_2.

This work was supported by grant from RSF #17-73-20030.

References: [1] Kovtunov et al., ChemCatChem (2018). [2] Svyatova et al., Chem. Eur. J. (2019).

GammaMRI: towards high-resolution single photon imaging using highly-polarized gamma-emitting nuclei

K.Kulesz[1,2], S. Pallada[3], V. Sanchez-Tembleque[4], J. Benito[4], M. Bissell[1], B. Crepieux[1], J. Croese[1,2], T. Kanellakopoulos[1,5], U. Köster[6], E. Vinckenbosch[3], L.M. Fraile[4], J. M. Udias[4], J.N. Hyacinthe[3], R.B. Jolivet[1,2], M. Kowalska[2]

[1] CERN, Meyrin, Switzerland, [2] University of Geneva, Geneva, Switzerland,

[3] Haute école de santé de Genève, Switzerland, [4] Universidad Complutense de Madrid, Spain, [5] KU Leuven, Leuven, Belgium, [6] Institut Laue–Langevin, Grenoble, France

Introduction. Our project aims to develop a new medical imaging modality able to overcome the limitations of existing imaging techniques and to combines their advantages. Gamma-MRI introduces the spatial resolution of MRI, the sensitivity of nuclear medicine (PET and SPECT) and possible clinical benefits of xenon isotopes [1,2]. At the same time, it eliminates drawbacks of the above-mentioned techniques. Our team is at present working on a proof-of-concept experiment [1].

Methods. Gamma-MRI is based on the detection of asymmetric γ-ray emission of long-lived polarized nuclear states in the presence of magnetic fields [2]. The nuclei used in our study are long-lived nuclear isomers of Xe isotopes: ^{129m}Xe ($T_{1/2}$ = 9 d),^{131m}Xe ($T_{1/2}$ = 12 d) and ^{133m}Xe ($T_{1/2}$ = 2 d) produced at the ILL high flux reactor in Grenoble or at ISOLDE facility at CERN [3]. The isomers of Xe are then hyperpolarized via collisions with laser-polarized rubidium vapor (Spin Exchange Optical Pumping) [4]. Once polarized and placed inside a magnetic field, they emit γ-rays whose direction of emission depends on the degree of spin polarization. This can be used to record the spins' response to rf pulses in gradient magnetic field, which is up to 10^5 more sensitive than usual signal pick-up in rf coils. They are acquired with CeGAAG crystals coupled to Si photodetectors and readout electronics compatible with strong magnetic fields, which are able to support very high count-rates.

Results and discussion. The experimental setups needed for the proof-of-concept experiment have been tested and verified. The polarization of Rb was achieved at the saturation level of about 50%. In addition, the production of ^{133m}Xe was tested at CERN and satisfying yields of ^{133m}Xe release were obtained.

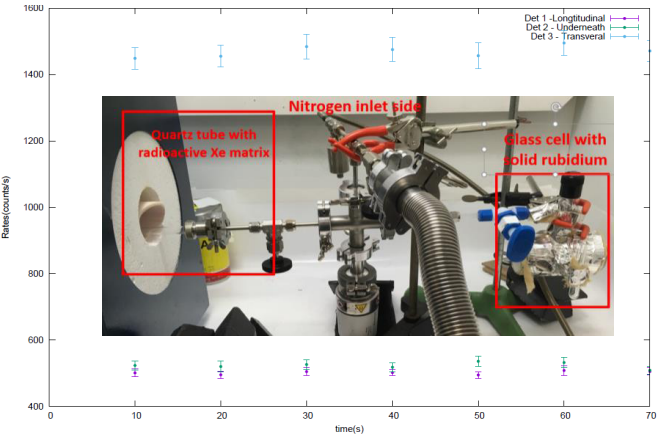

Figure 1. The setup used for the preparation of the mixture of gases: Xe, N_2 and Rb. The plot represents the count rate of γ-rays characteristic for ^{133m}Xe in presence of the laser and the magnetic field. The measurement was acquired with three detectors placed in longitudinal and transversal planes, with reference to the applied magnetic field.

Conclusion. The production of radioactive Xe isotopes: ^{129m}Xe and ^{131m}Xe at ILL is scheduled for June 2019. The aim of the experiment is to optimize the degree of polarization for both isomers after changing different experimental parameters, such as partial pressure of Xe and N_2. RF pulses will be further used to recor
This contribution will present the principle and status of the gammaMRI project and the latest results.

References:

[1] R. Engel, Master thesis 2018, https://cds.cern.ch/record/2638538.
[2] Y. Zheng et al., Nature 537, 652 (2016).
[3] M. Kowalska et al., Letter of Intent, CERN-INTC-2017-092 / INTC-I-205 (2017).
[4] T. G. Walker and W. Happer, Rev. Mod. Phys. 69, 629 (1997).

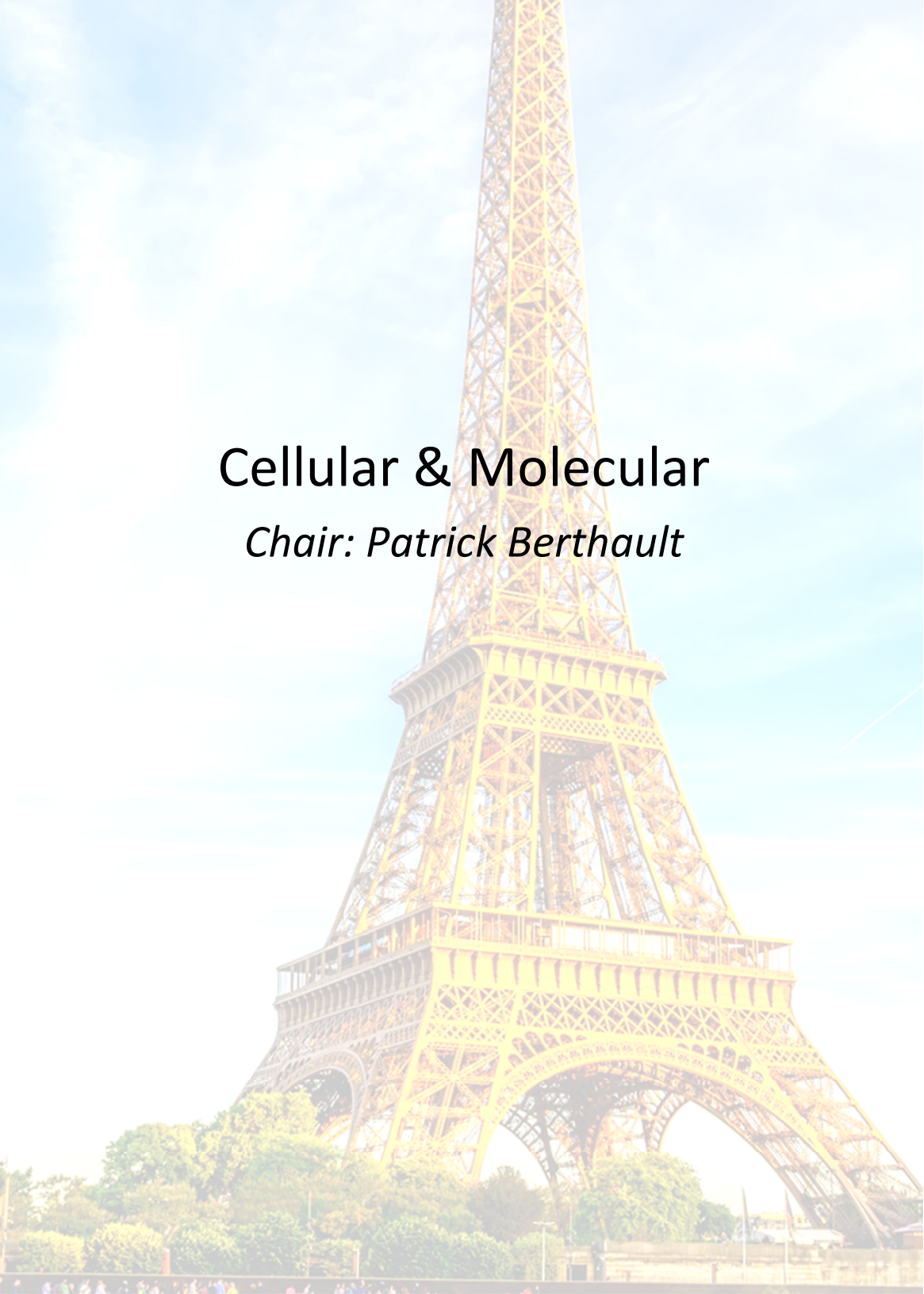

Cellular & Molecular

Chair: Patrick Berthault

Real-time in vivo MRI tracking of single cells and nanoparticles

Cornelius Faber
Clinical Radiology, University Hospital Münster, Münster, Germany

Non-invasive imaging of defined population or even individual cells is gaining increasing attention in basic biomedical research and also in the context of cellular therapies in patients. Labeling cells with super paramagnetic iron oxide nanoparticles (ION) provides strong contrasts and excellent detection sensitivity for the tracking of individual cells in vivo. Real-time tracking of slowly moving or migrating cells, however, requires sufficient temporal resolution to perform time-lapse MRI. We have shown that it is feasible to detect single cells in sequential acquisitions with an effective temporal resolution of one minute for the whole mouse brain in vivo. Simulations of image contrast showed that cells with velocities of roughly 1 μm/s can be detected, while faster moving cells did not give rise to sufficient image contrast. This velocity range is perfectly suitable to differentiate between slowly patrolling immune cells in healthy mice from faster moving cell after an immune response has been triggered. In different animal models we have triggered an immune response, which can be detected with high sensitivity before disease symptoms become evident. However, a quantitative assessment of ION-labelled cells in the body is not straight forward, due to processing of nanoparticles in vivo. For this purpose, we have employed ^{57}Fe-ION and combined MRI with ex vivo elemental mass spectrometric imaging by LA-ICP-MS. This approach allows to unambiguously identify labelled cells, follow their migration, assess biodistribution of the administered iron and study metabolization of ION. A different contribution to relaxivity depending on the physiological processing of ION was revealed, confirming both relaxation theories and models of iron metabolization.

A Novel MRI Technique for Quantifying Myelin in Mice Brain White Matter

E. Wilczynski, E. Sasson, U. Eliav, U. Nevo, G. Navon
Tel-Aviv University, Tel-Aviv, Israel

Introduction: *In-vivo* imaging of myelin could provide a tracking tool for demyelination disorders and facilitating the development of new therapeutic agents[1]. In this work we propose to use a recently reported MRI sequence, MEX, that measures a signal linearly dependent on the myelin protons fraction in the tissue[2], and uses a simple analysis procedure that can be applied in a clinical setup. The MEX sequence includes selective suppression of the water magnetization, by RF pulses and spoiling gradients, followed by a variable period (t_{LM}) in which magnetization recovery occurs[2]. Two processes dominate the observed signal: magnetization transfer between protons associated with lipid-protein molecules (myelin) and protons in the aqueous surrounding, and spin-lattice relaxation (T_1). The analysis of the image intensity dependence on t_{LM}, yields the percentile fraction of the myelin in the tissue (F), the exchange time (τ_{exc}) and T_1.

Methods: Cuprizone is a frequently used model for demyelination in mice[3]. Seven mice, fed with cuprizone and, four, fed with standard food, were imaged *in-vivo*. Animals were scanned using the proposed MEX sequence (Fig.1), on a 7T Bruker BioSpec scanner. The preparation MEX block was calibrated to ensure maximal water saturation at $t_{LM} = 10\ \mu s$, using hermite pulses adjusted to 3.3-3.7 watt, ensuring a good suppression. Following the recovery period, a standard gradient-echo imaging module was implemented. Ten different values of t_{LM} delays ranging 2.5-2500 ms were used to acquire two slices with TE/TR=3.5/3000 ms. The images were normalized by the longest t_{LM} scan, and fitted to Eq.1 using non-linear least squares in MATLAB (MathWorks, MA), assuming fast exchange.

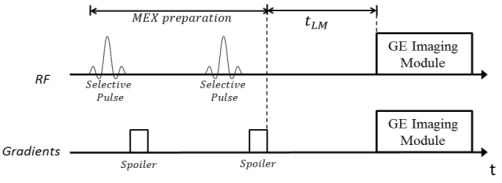

Fig. 1: MEX pulse sequence. Two selective pulses are applied at the water resosnance, each followed by a spoiler. The delay time, t_{LM}, is varied between repetitions.

$$M_{zw}(t_{LM}) = M_{ZW}^{eq}\left(F\left(1 - e^{t_{LM}/\tau_{exc}}\right) + (1-F)\left(1 - e^{t_{LM}/T_1}\right)\right) \qquad \text{Eq. 1}$$

Three regions of interest (ROI's) were segmented: white matter (WM) in the Corpus Callosum (CC) and Internal Capsule (IC), and gray matter in the cortex (GM). The signals of the pixels within the ROI's were summed and fitted to Eq.1, obtaining fit of R^2>0.999.

Results: The signal obtained from the scans show inversion of contrast along the t_{LM} scale, where in short delays WM/GM value is greater than one, and in long delays the ratio reverts. The maps obtained the fitted parameters show significant differences in the CC between the cuprizone fed mice and the control group (fig. 2). F is reduced by 25% (P<0.05), and T_1 is higher by 37% (P<0.01). The expected effect of the cuprizone model on myelin in the CC support these results of the F values[4]. In the IC and GM we cannot detect any significant decrease in the F values, resulting in a disappearance of contrast in the brain (not shown) [3], [5].

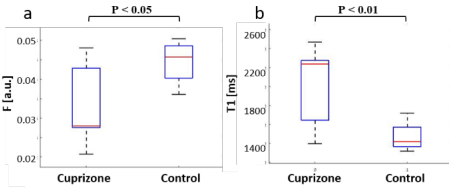

Fig. 2: (a) F, (b) T_1 parametrs for all cuprizone and control mice, averaged over the whole CC.

Conclusions: The results provide quantitative measure of demyelination in brain white matter, as demonstrated by the cuprizone model. The values of F show decreased content of myelin in the CC in cuprizone fed mice, and no changes in the in other white matter regions of the brain (IC) or in GM.

References: [1] Stikov Neuroimage(2015). [2] Eliav NMR Biomed.(2017). [3] Torkildsen, Acta Neuro. Scand.(2008). [4] Hibbits, ASN Neuro.(2012). [5] Matsushima, Brain Pathol.(2006).

Metabolic specificity analysis of CEST techniques at high and ultra-high magnetic fields

J.R. Krug[a], *S. Bardin*[b], *H. Lambers*[c], *H. Van As*[a], *A.H. Velders*[a], *C. Faber*[c], *F. Boumezbeur*[b], *L. Ciobanu*[b]

[a]Wageningen University & Research, Wageningen, The Netherlands, [b] Neurospin-CEA, Gif-Sur-Yvette, France, [c]University Hospital Münster, Münster, Germany

Introduction: Chemical Exchange Saturation Transfer (CEST) imaging enhances the sensitivity of metabolites by detecting them via the rapid chemical exchange between a group of labile protons and bulk water, hence allowing their spatial distribution mapping. Advantages of using high and ultra-high field strengths for CEST include increased SNR, longer T_1-relaxation times for more efficient saturation periods and larger chemical shift dispersion. Yet, an important challenge using CEST methods is the selectivity towards the metabolite of interest, due to overlapping resonance peaks. In this study, we investigated CEST's selectivity by parameter optimization for various metabolites of interest and at two field strengths B_0.

Methods: CEST-PRESS experiments were performed on 17.2 T and 7 T Bruker BioSpec preclinical scanners using four phantoms with the following solutions: i. 40 mM lactate, ii. 20 mM glutamate, iii. 20 mM glucose and iv. a mix of i.-iii. at identical concentrations. All samples had pH=7 and were scanned at room temperature. In addition, glu-and glucoCEST-experiments with PRESS and RARE were performed on a cherry tomato (*S. lycopersicum*).

Results and Discussion: Using parameter optimization, the CEST-contrast can be tuned to the metabolite of interest, i.e. its contribution to the asymmetric Magnetization Transfer Ratio (aMTR) can be maximized. As shown by the *in vitro* Z-spectra obtained at 17.2 T, it is possible to maximize the contribution of glutamate to aMTR at the saturation chemical shift of 3 ppm (Fig 1A) while reducing the glucose contribution to 26% using optimal parameters. In comparison, the specificity of aMTR decreases at 7 T presenting a 32% glucose contribution and a lower resolution of the individual metabolites (Fig 1B). At both magnetic fields, there was no significant lactate contribution to the gluCEST signal when saturating at 3 ppm. By changing the B_1-field intensity used for saturation, a shift in the maximum aMTR contrast from the glucose chemical shift (1.2 ppm) to the glutamate chemical shift (3 ppm) was observed (Fig 1C) on a voxel in the tomato outer pericarp. A stark difference between the gluco- and gluCEST images can be readily observed (Fig. 1D) stemming, most likely, from the different distributions of glutamate and glucose in the tomato. As expected, lower values were observed for glucoCEST contrast compared to gluCEST.

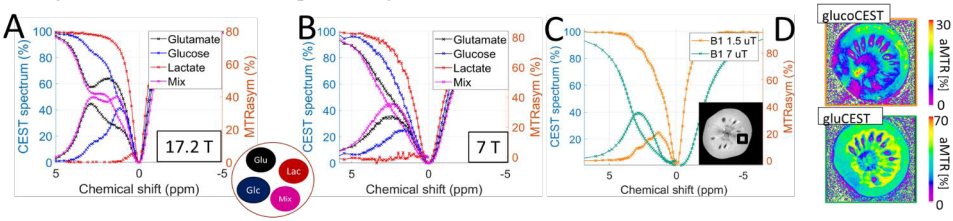

Fig. 1: Z-spectra acquired on the four solutions (see scheme) at A) 17.2 T and B) 7 T using a B_1-field strength of 7 µT. C) Z-spectra of a tomato pericarp at 17.2 T at B_1-field strengths of 1.5 µT (glucoCEST) and 7 µT (gluCEST). D) glucoCEST and gluCEST contrast images acquired with a CEST-RARE sequence (resolution 156µm x 156µm x 1mm; CEST T_{sat} 1.7s).

Conclusion: By carefully optimizing the CEST parameters, we can partially select for a compound of interest, i.e. glutamate or glucose. However, more sophisticated acquisition strategies and/or modelling approaches are necessary for the complete disentanglement of the different metabolite contributions (e.g. [1-2]).

References: [1] Yadav et al. Mag. Reson. Med. (2012) [2] Friedman et al. J. Am. Chem. Soc. (2010)

Probing displacements within and exchange among tissue microenvironments using static gradient spin echo diffusion and DEXSY NMR

N. H. Williamson[a], R. Ravin[a,b], D. Benjamini[a,c], H. Merkle[d], M. Falgairolle[d], M. J. O'Donovan[d], D. Blivis[d], D. Ide[e], T. X. Cai[a], R. Bai[f], P. J. Basser[a]

[a] NICHD, NIH, Bethesda, MD, USA; [b] Celoptics, Rockville, MD, USA; [c] CNRM, HJF, Bethesda, MD, USA; [d] NINDS, NIH, Bethesda, MD, USA; [e] NIMH, NIH, Bethesda, MD, USA; [f] College of Biomedical Engineering and Instrument Science, Zhejiang University, Hangzhou, China

Introduction: In systems with microscopic fluid compartments that communicate on timescales similar to the diffusion encoding time, resolution of pulsed gradient spin echo (PGSE) NMR is limited by the maximum gradient strength and the gradient pulse duration. Spin echoes acquired in a large static magnetic field gradient break this microstructural resolution limit and probe nanoscale structures in sub-millisecond timescales [1]. Under a static gradient g, the signal attenuation regime is determined by the restriction length l_s relative to the free diffusion length $l_D = \sqrt{2D_0\tau}$ and the dephasing length $l_g = (D_0/\gamma g)^{1/3}$ [2]. Diffusion EXchange SpectroscopY (DEXSY), both in a full [3] and a rapid approach [4], probes the exchange of water between these restricted environments. New methods to clear lipid membranes from tissue [5] provide a means to interrogate how water in distinct tissue microenvironments migrates within them and exchanges among them, providing a new window on tissue microstructure and microdynamics.

Methods: NMR measurements were performed at 13.79 MHz and g=15.3 T/m (l_g=800nm) on a PM-10 NMR MOUSE with a Kea2 spectrometer (Magritek). A double-wrapped solenoid RF coil (39 turns, 2mm ID, 1.3cm length) and circuit board were built in-house to maximize filling factor and SNR. The coil was glued within a chamber, specially built to maintain vitality of live specimens and to control temperature (7–37°C range). Experiments were performed on isolated spinal cords of newborn Swiss Webster wild type mice fixed in 4% paraformaldehyde. Static gradient spin echo 1-D diffusion (43 points, $\tau = 0.2 \rightarrow 6.55$ms) [6] and 2-D DEXSY ($21 \times 21$ points, $\tau_1, \tau_2 = 0.2 \rightarrow 3.3$ms, written in-house, 8-step phase cycle) experiments with CPMG acquisition (2000 echoes, TE=25μs, 400μm slice, TR=2s) were used to probe cellular and subcellular membrane components and water exchange between them.

Results and Discussion: About 25% of the signal arises from restricted water pools. About 5% of the signal is from restricted water with l<800nm. Water exchanges between restricted and free environments with a rate of roughly 100 1/s. Clearing lipids with 10%wt. Triton X surfactant shows membranes to be the origin of 99% of the water restriction.

Conclusion: Large static gradients provide a means to probe nano and microscale tissue components and the exchange between them. Exchange rates indicate that standard PGSE methods cannot resolve such components. The sensitivity of diffusion NMR to tissue microstructure is almost entirely due to membranes.

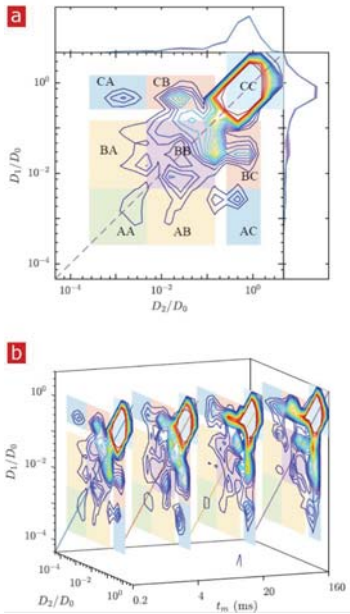

Fig. 1: DEXSY distributions for a fixed spinal cord sample (a) at mixing time t_m = 0.4ms and (b) at increasing t_m showing the build-up of exchange (off-diagonal) components and decay of the non-exchange (on-diagonal) components.

References: [1] Kimmich, J. Mag. Reson. 91 (1991). [2] Hurlimann, J. Mag. Reson. 113 (1995). [3] Callaghan, J. Chem Phys. 120 (2004). [4] Cai, J. Mag. Reson. 297 (2018). [5] Leuze, Neuroimage 156 (2017). [6] Rata, J. Mag. Reson. 180 (2006).

Erwin Hahn Lecture:

Echoes: A circle from the past to the future

Bernhard Blümich
Institut für Technische und Makromolekulare Chemie, RWTH Aachen University,
Aachen, Germany

While NMR spectroscopy can largely do without echoes, other manifestations of NMR cannot. The primary ones are NMR imaging and NMR relaxometry. Both are central topics of the International Conference on Magnetic Resonance Microscopy. The spectroscopic echo has been discovered by Erwin Hahn and interpreted in terms of time reversal limited by entropy. Echoes are partially blurred mirror images of the past, whereby the irreversible blurring arises from random thermal motion. This lecture echoes personal encounters with echoes generated by nonlinear interference of the response to continuous random excitation, with echoes to probe rotational molecular motion in solids, with solid echoes for line narrowing in spectroscopy, and with gradient echoes for space and flow encoding in MRI. Moreover, echoes enable NMR with simple magnets that do not provide homogeneous magnetic fields. These magnets can be made small, so that the discovery of the echo has led to the miniaturization of NMR magnets and eventually to mobile and to compact NMR instruments. Today's compact NMR spectrometers will become even smaller so that the discovery of the echo has stipulated the development of miniature chemical NMR sensors capable of functioning without echoes.

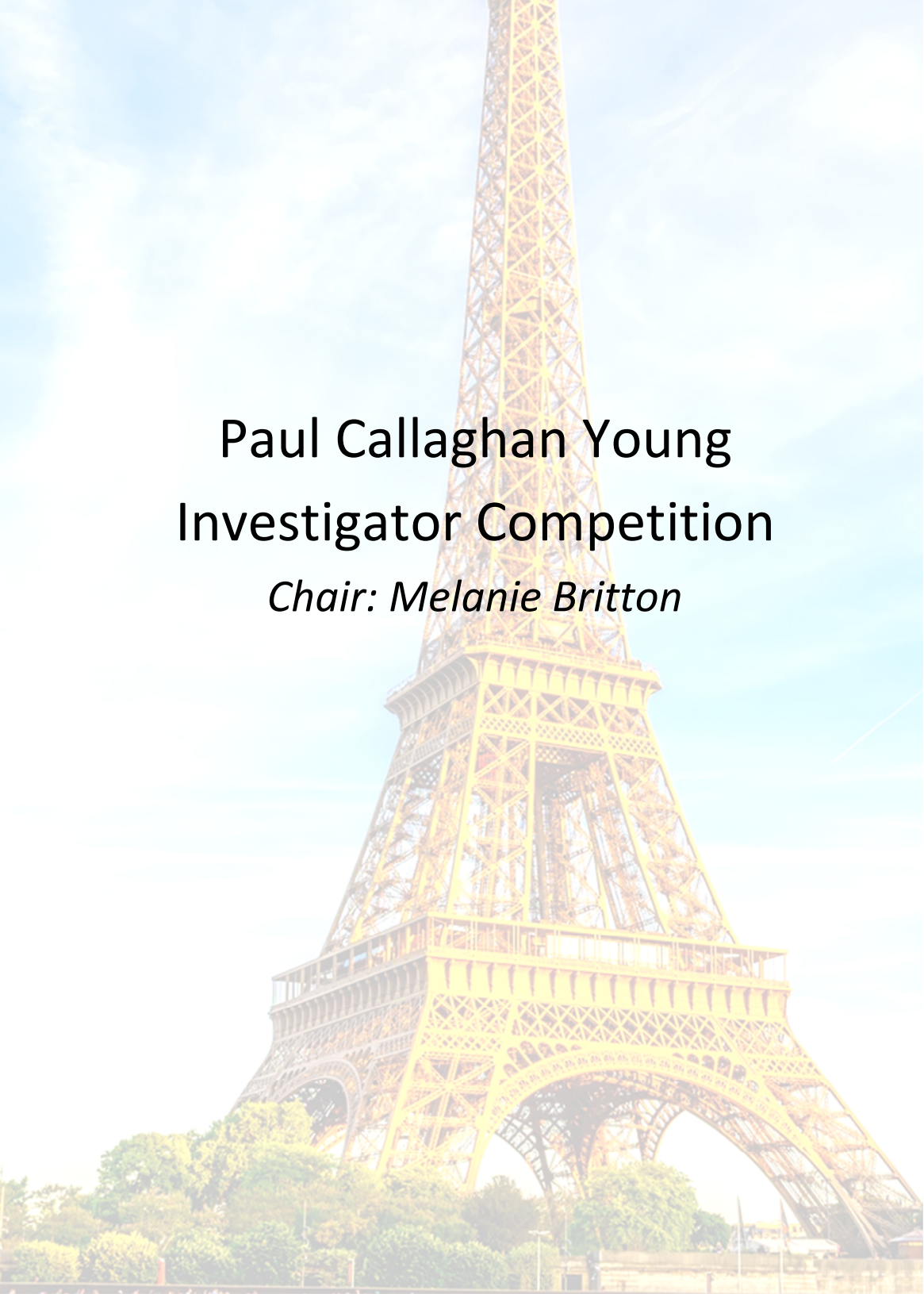

Paul Callaghan Young Investigator Competition

Chair: Melanie Britton

Para-Hydrogen Induced Polarization – Production of highly concentrated metabolite precursors and long polarization storage over 10s of minutes

S.Glöggler[a]
[1]Max Planck Institute for Biophysical Chemistry, Göttingen, Germany

Introduction: Nuclear magnetic resonance (NMR) comes with the drawback of inherently low sensitivity. In order to improve detection sensitivity and enhance signals of certain compounds, hyperpolarization techniques have been developed.[1-6] Among these methods, para-hydrogen induced polarization (PHIP) is a rapid approach that generates hyperpolarized molecules within seconds.[3] At the conference, I am going to present the most recent advances that have enabled us to generate highly concentrated (50 mM) solutions of metabolites and their precursors (P_{13C} > 50%) with particular applicability for in vivo experiments in the future.[6-9] Furthermore, we show our recent progress in polarizing a library of ^{15}N-enriched compounds in which the hyperpolarized signal can be stored for 10s of minutes enabling the design of long traceable contrast agents.[10,11]

Results and Discussion:
All of our hyperpolarization experiments were performed with our recently introduced pulsed polarization transfer sequence termed ESOTHERIC (Efficient Spin Order Transfer via Relayed Inept Chains).[6,7] This sequence allows for near unity transfer of para-hydrogen spin order to ^{13}C spins. It was optimized to compensate for radiation damping effects which occurred in utilized 7T and 1T spectrometers once concentrations above 1 mM were attempted to be polarized.[9] Applying the new sequence allowed us to achieve more than 50% ^{13}C polarization in 50 mM concentrated solutions of acetate precursors (figure 1). As the developed sequence only requires weak coupling conditions, we have managed to incorporate it into a low field spectrometer at 1T and demonstrate similar polarization results on the acetate precursor. We have subsequently synthesized a variety of metabolite precursors including pyruvate and amino acids and demonstrate their polarization as well as cleavage of the precursor into the respective metabolite.[6-8]

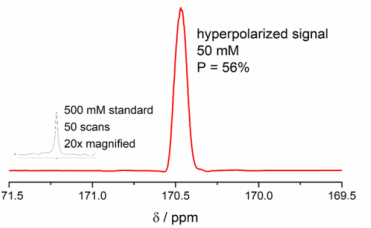

Fig. 1: Hyperpolarized ^{13}C-signal of a highly concentrated acetate precursor.

In addition to the designed metabolite precursors, possibilities to store hyperpolarization for tens of minutes have been investigated in newly designed quaternary ^{15}N-enriched molecules.[11] A library of compounds will be presented and their applicability discussed for future applications. Hyperpolarization of the ^{15}N-nuclei has partly been achieved by utilizing newly designed nanocatalysts and the transfer sequence described above.[10]

Conclusions:
Overall, we have introduced an approach to quickly generated hyperpolarized metabolites and compounds with long polarization storage times. The applicability of this approach in low field systems increases portability and cost efficiency of the shown method.

References:
[1] Walker, Happer, Rev. Mod. Phys. 69, 629 (1997). [2] Larsen et al., PNAS 100, 10158 (2003) [3] C. R. Bowers, D. P. Weitekamp, Phys. Rev. Lett. 57, 2645 (1986). [4] R. W. Adams et al., Science 323, 1708 (2009). [5] F. Reineri et al., Nat. Commun. 6, 5858 (2015). [6] S. Korchak et al. ChemistryOpen 7, 344 (2018). [7] S. Korchak et al. ChemistryOpen 7, 672 (2018). [8] L. Kaltschnee et al. submitted (2019). [9] S. Korchak et al. in preparation (2019). [10] J. McCormick et al. Angew. Chem. Int. Ed. 130, 10852 (2018). [11] A. Jagtap et al. submitted (2019).

Ferroelectric Composite Ceramic Probe for MRM

M. A.C. Moussu[1,2], S. Glybovski[3], E. Nenasheva[4], R. Abdeddaim[1], S. Enoch[1], L. Ciobanu[5]
[1]Aix Marseille Univ, Marseille, France, [2]Multiwave Innovation, Marseille, France, [3]ITMO University, Saint-Petersburg, Russia, [4]Ceramics Co.Ltd, Saint-Petersburg, Russia, [5]CEA/DRF/NeuroSpin, Gif-sur-Yvette, France

Introduction: In Magnetic Resonance Microscopy (MRM), losses inherent to the probe and its interactions with the sample fundamentally limit the achievable Signal-to-Noise Ratio (SNR) and hence the spatial resolution. The reference volumetric probe is the solenoid, for which the imaging performance is limited by the electric field induced in the conductive biological sample [1]. To overcome this limitation, a novel MRM probe is proposed, exploiting the first resonant mode of a ceramic ring resonator to reduce the electric field level in the sample [2].

Methods: The design of the prototype ring resonator was based on a self-developed analytical model and consisted in a specially created 50/50 low-loss composite of $BaTiO_3/SrTiO_3$ with Mg additives [3], with the following geometrical parameters: OD 18 mm, ID 5.5 mm, H 10 mm. The composite properties, measured at ambient temperature, were: real relative permittivity 536 and loss tangent 8.10-4. During MR experiments at 17.2 T, the first transverse electric mode was excited with a loop (ID 1 cm) placed close to the resonator. The latter was tuned to 730 MHz by imposing its temperature to be 21.8°C using a circulating water pad. The reference solenoid coil, built for comparison, had a similar internal volume and was designed to maximize the SNR according to Ref. [4] (4 turns, D 5.5 mm, L 12 mm, 1.5 mm thick copper wire).

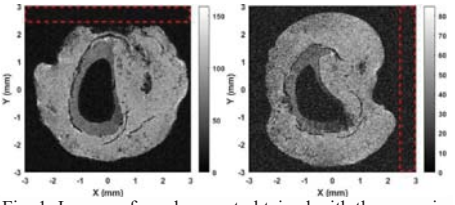

Fig. 1: Images of a red currant obtained with the ceramic ring (left) and the solenoid (right). Acquisition parameters: gradient echo sequence, flip angle 15°, TE 6 ms, TR 33 ms, spatial resolution 23 µm isotropic, acquisition time 35 min.

Results and discussion: Selected slices from 3D images of a red currant, acquired with the two probes using identical acquisition parameters, are shown in Fig. 1. The standard deviation of the noise, computed within the red boxes and averaged over the entire sample length in the signal-less area, had similar values for the two probes: 6.34 and 6.36 for the ceramic ring and the solenoid, respectively. However, as illustrated by the voxel intensity histograms in Fig. 2, the image quality for the ceramic probe is superior to that of the solenoid, with no overlap between the signal and the noise histograms. From the histograms in Fig. 2, we can also infer the SNR obtained with the ceramic probe which is 1.9 times higher than that of the solenoid. The B1 homogeneities of the two probes were similar (data not shown).

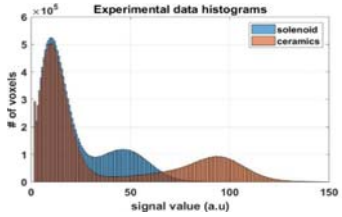

Fig. 2: Voxel intensity histograms of the data sets acquired with the two probes.

Conclusion: We report the design and construction of a novel ceramic MRM probe, which enables a two-fold SNR gain over the traditional solenoidal coil.

References: [1] Park, J. Magn. Res. (2009). [2] Webb, Concepts Magn. Reson. B (2011). [3] Nenasheva, Ferroelectrics. (2017). [4] Minard, Concepts Magn. Reson. (2001).

Acknowledgements: This project received funding from the European Union's Horizon 2020 research and innovation program (grant agreement No. 736937) and from the Russian Foundation for Basic Research (grant No. 18-32-20115).

NMR Relaxation Measurements of Solid-Solid Phase Transitions in Complex Lipid Systems

Madison L. Nelson[1], *Sarah L. Codd*[2], *Jonathan L. Cape*[4], *Christopher D. Craig*[4] *and Joseph D. Seymour*[3]

[1]Physics, [2]Mechanical and Industrial Engineering, [3]Chemical and Biological Engineering, Montana State University, Bozeman MT, USA, [4]Lonza Pharma & BioTech, Bend OR, USA

Lipids are complex macromolecular mixtures with interesting and complicated solid polymorphic crystal states. Understanding and creating techniques to explore these systems, which are crucial components in pharmaceutical drug delivery, food science and membrane biology, will improve understanding of material properties and their relation to material function. Nuclear magnetic resonance (NMR) is uniquely qualified to study these complex structures in real time without disturbing the microstructural domains. A universal method for detecting transitions between solid-solid or solid-liquid configurations is differential scanning calorimetry (DSC), in which the temperature of a system is changed, as the heat capacity is measured. However, this method can be invasive, in melting certain domains, and dependent on the rate of temperature change. Solid state ^{13}C NMR has been implemented to probe the dynamics with temperature to obtain information about transitions between and mixing of polymorphic domains[1].

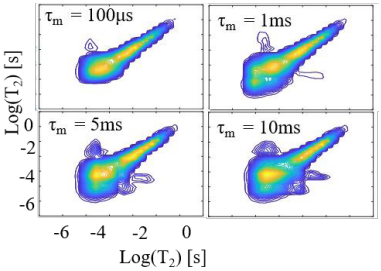

Fig. 1: T_2-T_2 exchange plots of beeswax at 50˚C for increasing τ_m times.

It is also well established that multidimensional relaxometry is useful to characterize exchange with mass transport between domains[2-4]. In systems with no mass transfer, solid state methods, using spin diffusion magnetization exchange during an evolution period after selection based on dipolar coupling, are well established for characterizing domain size in polymer[5] and lipid[6] systems with domains of varying T_2 relaxation. The influence of spin diffusion, or flip-flop secular dipolar interactions, on T_2-T_2 experiments were indicated by Hills and coworkers for aqueous protein gels[7] and Washburn for kerogen in shales[8]. Here, NMR relaxometry is used to characterize temperature dependent solid-solid phase transitions in terms of relaxation distributions and magnetization exchange for lipid systems.

The two complex lipid systems in this work, beeswax and glyceryl behenate, exhibit exchange without mass transport. Data for T_1-T_2 correlation experiments, T_2-T_2 exchange experiments and T_2 distribution dispersion (varying echo time τ) experiments[9] are presented. The measured exchange times between domains, shown for beeswax in Fig. 1, are of the order of 0.1-100 ms, consistent with spin diffusion of the order of 10^{-16} to 10^{-18} m^2/s with average domain separations 0.1-10 nm[5,10]. The complexity and variability in a natural product like beeswax makes association of specific domains with T_2 more complicated. The glyceryl behenate system allows reproduceable deconstruction in terms of its triglycerides. In doing so, we determine domain sizes, the partitioning of mono-, di-, and tri- components within the domains. This is done through T_2 distribution dispersion measurements. Decomposing the triglyceride provides an in-depth analysis of the relaxation distribution properties of glyceryl behenate, the base of many drug delivery techniques, extending the ability of NMR relaxometry to characterize lipid systems.

References:

[1] Kameda, T., J. Phys. D, (2005). [2] Washburn, K. et al., PRL (2006). [3] Song, Y. Q.et al., PRL (2014). [4] Williamson, N. et al., PRL (2019). [5] Buda, A et al., Solid State Nucl Mangn Reson (2003). [6] Huster, D. et al., JACS (2001). [7] Venturi, L et al. Appl Magn Reson (2008). [8] Washburn, K. E et al., JMR (2017). [9] Hills, B., et al., Macromolecules (1991). [10] Nelson, M. et al., To be submitted PCCP (2019).

Real-time imaging of granular dynamics

Alexander Penn[1,2], *Christopher M. Boyce*[2,3], *Klaas P. Pruessmann*[1], *Christoph R. Müller*[2]
[1]Institute of Biomedical Engineering, ETH Zurich and University of Zurich, Zurich, Switzerland
[2]Department of Mechanical and Process Engineering, ETH Zurich, Zurich, Switzerland
[3]Department of Chemical Engineering, Columbia University, New York, NY, USA

The dynamics of granular materials govern natural phenomena ranging from earthquakes, to avalanches to landslides and are critical for a variety of industrial applications. Our fundamental physical understanding of granular dynamics, however, is still incomplete. One major challenge towards a better understanding of granular dynamics is the difficulty to obtain spatially and temporally resolved measurements of particle dynamics from the interior of 3D granular systems. Magnetic resonance imaging (MRI) is able to measure a variety of relevant system properties, however, one of the largest limitation so far has been the rather low temporal resolution. Here we report our recent developments, an MRI methodology that increases the temporal resolution of phase contrast velocity encoded imaging of granular dynamics by more than four orders of magnitude, effectively advancing MRI of granular dynamics from temporally averaged to real-time imaging [1]. The advances are enabled by an interplay of engineered MR signal sources, time-efficient single shot readouts and radiofrequency (RF) hardware developments and provide insight into hitherto unknown facets of dynamic granular behavior (Fig.1). We are confident that the methodology will be useful for studying a variety of dynamic granular systems in the fields of process engineering, granular physics and geophysics.

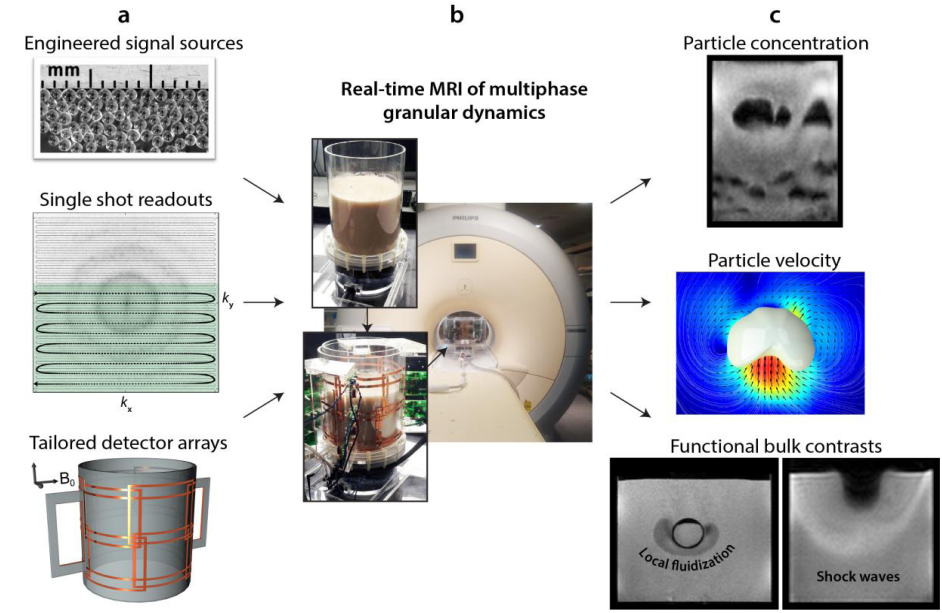

Figure 1. (a) Real-time MRI of granular dynamics is enabled by a concerted interplay of granular signal source engineering, time-efficient single-shot pulse sequence design and array detection using custom-build RF detector arrays. (**b**) A fluidized bed model system (diameter 190 mm) was placed inside the RF detector array and inserted into the bore. (**c**) The methodology has been used to acquire instantaneous snapshots of local particle concentration and particle speed. Moreover, it was used to produce MR contrast based on fluidization and shock waves in granular materials.

References:

[1] A. Penn, T. Tsuji, D. O. Brunner, C. M. Boyce, K. P. Pruessmann, and C. R. Müller, Sci. Adv. **3**, e1701879 (2017).

MRI of the Interplay between Fluid Dynamics and Heat Transfer

ME Skuntz[a], *JD Seymour*[b], *R Anderson*[a], *and SL Codd*[a]
[a]Montana State University, Bozeman, United States

Introduction:
MRI is a proven method for investigating convection in complex fluid systems [1, 2]. Its noninvasive nature allows time and space dependent changes to flow and structure to be captured without disruption to sensitive systems. This research investigates the interplay of fluid dynamics and heat transfer through Rayleigh-Bénard convection (RBC) with and without porous media packing. Figure 1a is a diagram of the flow cell, with a dashed blue box outlining the imaging region. In RBC, an adverse density-gradient is induced across the sample by heating the contained fluid from below. The stability of RBC is controlled by the Rayleigh number (*Ra*) of the flow and container aspect ratio (Γ = radius/depth). *Ra* is the ratio of the buoyancy forces to dissipation from thermal diffusion and viscosity in the fluid [3]. Therefore at low *Ra*, dissipation prevents fluid motion and heat flow is purely diffusive. The critical Rayleigh number (Ra_c) is the point at which buoyancy initiates convection. Above Ra_c, the fluid organizes itself into convective cells. As *Ra* is increased further, the flow spontaneously bifurcates, reorganizing itself into different flow patterns. Research here is focused on cylindrical containers of low-aspect ratios (Γ = 3/50) where fluid properties can change with height, wall effects are substantial [4] and industrial applications are often found (such as beer pasteurization or processing of canned foods). The study of bulk fluid RBC provides template velocity data for comparison to RBC in porous media which is difficult to study using other methods.

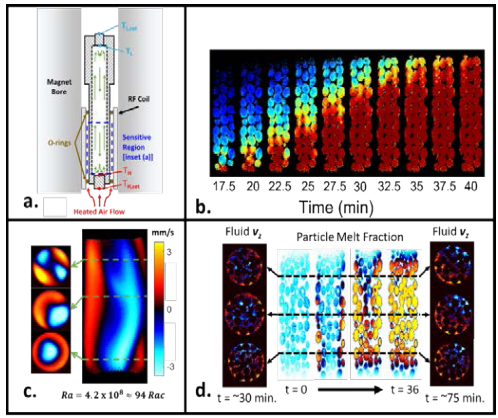

Fig. 1: (a.) A cross-sectional diagram of the flow cell with the sensitive region of the imaging coil outlined in blue. (b.) Forced convection melting of encapsulated wax. (c.) $\mathbf{v_z}$ velocity images of RBC convection show three different flow patterns in the transverse images over a 40 mm axial span. (d.) Change in preferential flow pattern after melting of wax at left and right. Central sequence shows melting starts at circumference edge.

Methods: To study heat transfer in packed beds, the solid packing and pore filling fluid were chosen to be chemically distinct, preventing signal interference between the two domains. The pore-space was filled with a fluorinated heat-transfer fluid. At various stages of heating, PGSE experiments were performed at the ^{19}F frequency to measure spatially resolved velocity maps and non-spatially resolved distributions of average and fluctuating velocity for the pore fluid. For the solid packing, particles composed of wax micro-encapsulated into plastic spheres and agglomerated into larger particles (d = 3.5 mm) were chosen. The solid and liquid states of wax can easily be distinguished with MRI. At the ^{1}H frequency, the MSME sequence provided complementary MRI of particle-wax melt-fraction which could be interpreted as a temperature front [5].

Results and Discussion: Data on a forced convection system, the results of which are shown in figure 1b [5] established the methodology. Intra-particle melting, melt-front and coupling of fluid motions to particle heating were visualized in the experiments. RBC is more complicated due to complex flow cells where hysteresis has a strong effect, as previously determined [6]. It was found that circulation patterns were strongly dependent on height in the fluid column (figure 1c). During experiments on RBC in porous media, the effects of heat transfer on flow pattern formation were observed. The preferential flow pattern depended on the wax particles absorption and emission of energy (figure 1d).

Conclusions: The selection of packed bed components, which are chemically distinct, allows MRI visualization of the coupling of heat transfer to fluid flow. The use of phase change materials as temperature indicators in fluid systems provides a robust temperature front mapping method for a range of investigations.

References: [1] Blümich, "NMR imaging of materials." (2004). [2] Callaghan, "Principles of nuclear magnetic resonance microscopy." (1993). [3] Koschmieder, "Bénard cells and Taylor vortices" (1993). [4] Charlson, Int. J. Heat Mass Trans. (1971). [5] Skuntz, Chem. Eng. Sci. (2018). [6] Hof, Phys. Fluids. (1999).

SPatiotemporal ENcoding (SPEN) 3D Diffusion Tensor Imaging of *in vivo* mouse brain at ultra-high fields and ≤ 100µm isotropic resolutions

M. Yon[1], Q. Bao[1], R. Henriques[2], N. Shemesh[2] and L. Frydman[1]

[1] Department of Chemical and Biological Physics, Weizmann Institute, Rehovot, Israel
[2] Champalimaud Neuroscience Programme, Centre for the Unknown, Lisbon, Portugal

Introduction: Echo Planar Imaging (EPI) remains a key component in a wide range of applications requiring fast MRI without using a train of refocusing pulses, including functional MRI and Diffusion Weighted / Diffusion Tensor Imaging (DWI / DTI). EPI, however, faces known challenges when targeting heterogeneous tissues, when operating at high magnetic fields, or in other instances where field inhomogeneities become important. Spatiotemporal Encoding (SPEN) has been shown to be a robust alternative to deal with these challenges.[1-3]
I intend to present the features of the SPEN sequence which induce this robustness and how it can be used to perform *in vivo* 3D DTI of mice brains at 15.2T at a spatial resolution down to 75 µm isotropic. I will also show how the zooming ability of the SPEN sequence allows reaching such high resolution which has never been achieved *in vivo* with the EPI sequence.

Methods: All experiments were performed on a Bruker 15.2 Tesla preclinical MRI scanner with a surface ^{1}H quadrature transmit/receive surface coil MRI CryoProbe. The SPEN package (running on Paravision® 6 environment), is available for download.

Results and discussion: The non-b-weighted and color-coded main diffusion direction SPEN and the SE EPI images exhibit similar morphological details. SPEN images have a lower SNR than EPI due to their longer echo times and higher effective b-values induced by the SPEN imaging gradient[4]; still, the SPEN images also show reduced B0 and B1 inhomogeneities artifacts – particularly in the olfactory bulb region.

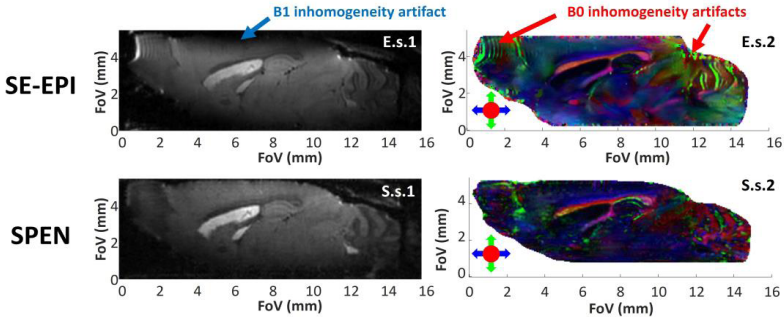

Fig. 1: Non-b-weighted and Color-coded main diffusion directions (MDDs) sagittal images extracted from 3D *in vivo* brain images obtained by interleaved SPEN and SE-EPI with double sampling in two hours exhibiting a resolution of 120 µm isotropic.

Conclusion: SPatiotemporal ENcoding is shown to be much more resilient to B0 and B1 inhomogeneities compared to SE EPI and allow preclinical micro-DTI, functional MRI, and real-time acquisitions at very high magnetic fields with high resolution and robustness.

References:
[1] Seginer, Magn. Reson. Med. (2014). [2] Schmidt, Magn. Reson. Med. (2016). [3] Bao, Proc. Intl. Soc. Mag. Res. Med. 1021 (2018). [4] Solomon, J. Magn. Reson. (2013).

Stimulated Hahn Lecture:

Pre silicon-age NMR: a look back in time

Eiichi Fukushima (ABQMR)

Imagine magnetic resonance experiments without Fourier transforms, signal averaging, and even the ability to digitally record the data. We will take a short nostalgic(?) journey into the era of pre-silicon NMR when, in retrospect, an amazing quality of experimental results and insights into magnetic resonance were realized.

Engineering & Materials

Chair: Vincent Sarou-Kanian

LAOS Rheo-NMR

Joseph D. Seymour
Chemical and Biological Engineering, Montana State University, Bozeman MT USA

Material property characterization often uses rheology, which involves measuring the material response to deformation and flow, since the processing and function of many materials depend on their behavior under deformation or flow. Soft matter physics in general deals with systems that are complex due to the scale of the polymers, colloids, particulates or multiple phases of which they are composed [1,2]. Soft matter materials underlie many systems encountered in daily life from food to health and personal care products. The dissipative, heterogeneous and non-equilibrium nature of the microscale dynamics in most soft matter systems impact the macroscale material response, generating rheological responses that depend on microstructure. In many processing and application environments large amplitude and oscillatory shear forces are applied to materials. This has led to development of large amplitude oscillatory shear (LAOS) rheometry methods [3,4]. Using NMR and MRI velocimetry, spectroscopy and relaxometry to study materials under shear is well established and termed Rheo-NMR [5]. Here the application of Rheo-NMR methods during LAOS in a Couette flow cell is demonstrated and a means of analysis considered, using fluids exhibiting a range of rheological responses, *i.e*. Newtonian viscous, yield stress, shear thinning, thixotropic [5].

References: [1] Pierre-Gilles de Gennes, "Soft matter–Nobel Lecture", Reviews of Modern Physics **64**(3) 645-648 (1992).
[2] Sidney R. Nagel, "Experimental soft-matter science", Reviews of Modern Physics **89** 025002 (2017).
[3] K. Hyun *et al*. "A review of nonlinear oscillatory shear tests: Analysis and application of LAOS", Progress in Polymer Science **36**(12) 1697-1753 (2011).
[4] Simon Rogers, "Large amplitude oscillatory shear: Simple to describe, hard to interpret", Physics Today **71**(7) 34-40 (2018).
[5] P.T. Callaghan, "Rheo-NMR: nuclear magnetic resonance and the rheology of complex fluids, Reports on Progress in Physics **62** 599-670 (1999).
[6] J.S. Jayaratne, T.I. Brox, *et al*. "LAOS Rheo-NMR" to be submitted Journal of Rheology (2019).

Fast ultrafiltration characterization by compressed sensing MRI

S. Schuhmann[a], *N. Schork*[a], *J. W. Simkins*[c], *S. L. Codd*[c], *J. D. Seymour*[c], *M. Heijnen*[d], *G. Guthausen*[a,b]

[a]Institute for Mechanical Process Engineering and Mechanics, KIT, Karlsruhe, Germany
[b]EBI, Chair of Water Chemistry and Water Technology, KIT, Karlsruhe, Germany
[c]Chemical & Biological Engineering Department and & Mechanical & Industrial Engineering Department, MSU, Bozeman, U.S.A.
[d]inge GmbH, Greifenberg, Germany

Introduction: Ultrafiltrations enable the production of germ and bacteria free drinking water. During filtration, fouling (accumulation of matter on the membrane wall) reduces the filtration efficiency, which means that the membrane has to be backwashed with high energy costs. Since the investigated membrane is filtrated from the inside to the outside, it is difficult to characterize the filtration process optically. It is still unknown if the feed channels of multichannel membranes are filtrated evenly or if there are some differences. MRI can be used as a tool to answer this question and to quantify the performance of the single feed channels. Fast MRI measurements are necessary because the filtration process is highly time-dependent. Therefore, compressed sensing MRI methods are explored.

Methods: Ultrafiltrations were characterized by compressed sensing (CS) MRI methods. Sodium alginate was used as model for extracellular polymeric substances (EPS), which are discussed as the main cause of fouling in waste water treatment. The fouling mechanism can be changed by adding $CaCl_2$ to the aqueous alginate solution. As a result the fouling layer behaves like a gel instead of a concentration polarization. In order to achieve a better T_2-contrast between fouling layer and feed solution, the superparamagnetic magnetite alginate is used as contrast agent. CS MR intensity and velocity images were measured during filtration and reconstructed with a l_1 non-linear conjugate gradient method [1].

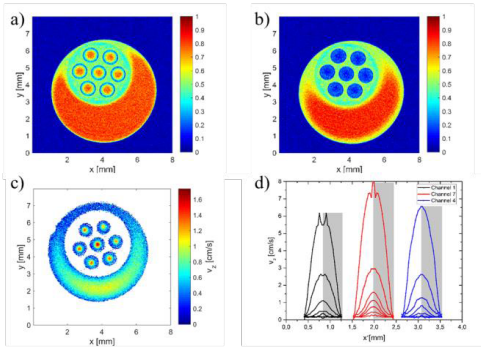

Fig. 1: a) Intensity image of a multichannel membrane at the beginning of the filtration: no deposits in the feed channels. b) after 50 min of alginate filtration the deposits appear with low intensities c) velocity image during filtration. d) flow profiles in the different feed channels were extracted from the velocity images [2].

Results and discussion: Intensity and velocity images were measured during the filtration of alginate (aqueous solution). Fouling layer and flow fields were measured and analyzed. The outer channels of the multichannel membrane perform evenly except for the channel in the center. The velocities and volume flows are slightly higher. The Poiseuille equation describes the data well for the filtration with Ca^{2+}. The flow profiles for the filtration without Ca^{2+} deviate from the Poiseuille profile due to the concentration polarization.

Conclusion: Ultrafiltrations were characterized by CS MR intensity and velocity measurements. Different fouling mechanisms were identified and analyzed.

References:

[1] M. Lustig, Compressed Sensing MRI Resources, Software (2016).
[2] S. Schuhmann et al., J. Membrane Sci. (2019), 570, 472.

Opencage: RF coil with an adjusted current distribution

Anton Nikulin[1], Benoit Larrat[2], Kylian Haliot[2], Abdelwaheb Ourir[1], Julien de Rosny[1]
[1]Institut Langevin, ESPCI Paris, CNRS, PSL University, 1 rue Jussieu, 75005 Paris, France, [2]CEA, DRF, JOLIOT, NeuroSpin, UNIRS, Université Paris-Saclay, 91191 Gif-sur-Yvette Cedex, France

Introduction: The main volume RF coil used in MRI is the birdcage one which provides a homogeneous signal in the whole volume under study [1]. A birdcage is a circular metallic ladder closed on itself, the magnetic field being generated by the current circulating in the legs. In certain applications the birdcage coil is inconvenient due to a short distance between neighbor legs. Here it is proposed to solve this issue by breaking the periodicity of ladder distribution in order to open a wide access to sample under study. The proposed design is called opencage [2], it has been tested numerically and experimentally for proton imaging of small animals at 7T.

Methods: The design of an opencage coil is based on the metacage analysis. In general, a metacage is made of a metasurface composed of transmission line unit cells. Consequently, a birdcage can be interpreted as a particular metacage where all the unit cells are identical. By adjusting the properties of each unit cell, an original field distribution can be obtained. Here, this approach is used to increase the distance between two neighbor legs on the top of a metacage. The opencage is composed of six legs where four legs are separated by 45° and the two other ones by 90°. The unit cells are designed in order to induce phase shifts that corresponds to the geometrical angle. Beside the phase shift, the Bloch impedance of all the unit cells are identical to avoid reflections due to unmatched impedance.

Results and discussion: The results of calculations have been verified using commercial software CST Studio Suite 2018. Since the coil has been optimized, the prototype has been assembled and tested both with phantom and in-vivo in the preclinical MRI scanner Bruker PharmaScan 7T. An original sequence is used to map the B_1^+ field [3]. The results of phantom and in-vivo imaging have been compared with the conventional birdcage coil of the same size (radius = 35 mm; length = 40mm). The opencage demonstrates suitable homogeneity of signal in the bottom half of the phantom. The relative standard deviation is 8.8% for the opencage versus 8.3% for the birdcage. SNR is comparable for both images 1865 for the opencage versus 1752 for the birdcage coil.

Conclusion: The metacage approach has been used to design an original opencage coil that provides a wide access to the ROI. The coil has been tested for a preclinical imaging of small animals at 7T. It is shown analytically and numerically that the proposed coil achieves suitable homogeneity and SNR. The experimental demonstration of the opencage in the preclinical MRI scanner has validated our approach. Furthermore, the tests of the opencage coil in clinical MRI at 7T are ongoing.
This project has received funding from the European Union's Horizon 2020 research and innovation program under grant agreement No 736937. This work is supported by LABEX WIFI (Laboratory of Excellence within the French Program "Investments for the Future") under references ANR-10-LABX-24 and ANR-10-IDEX-0001-02 PSL.

References: [1] Cecil E. Hayes, William A. Edelstein, John F. Schenck, Otward M. Mueller, Matthew Eash, An Efficient, Highly Homogeneous Radiofrequency Coil for Whole-Body NMR Imaging at 1.5 T, Journal of Magnetic Resonance, vol. 63 (3), p. 622-628, 1985.
[2] A. Nikulin, J. de Rosny, K. Haliot, B. Larrat, and A. Ourir, Opencage Radio Frequency Coil for Magnetic Resonance Imaging, Applied Physics Letters, vol 114 (5), 053503, 2019.
[3] Kay Nehrke, On the steady‐state properties of actual flip angle imaging (AFI), Magnetic Resonance in Medicine, vol. 61, pp. 84–92, 2009.

Rheological NMR to study polymer dynamics and protein aggregation

B. Kohn[1], V. Körber[1], E. Stündel[1], E. Walinda[2], K. Sugase[3], D. Morimoto[3], P. Galvosas[4], U. Scheler[1]

[1]Leibniz-Institut für Polymerforschung Dresden e.V, Dresden, Germany, [2] Department of Molecular and Cellular Physiology Kyoto University, Kyoto, Japan, [3] Department of Molecular Engineering, Kyoto University, Kyoto, Japan, [4]School of Chemical and Physical Sciences, Victoria University of Wellington, Wellington, New Zealand

Introduction: Rheo NMR has been applied to investigate the effect of external shear on the aggregation of proteins [1-2] and on the chain dynamics of polymers [3], where under shear enhanced polymer dynamics is observed instead of shear-induced chain ordering. Most commonly a Couette geometry is applied for such studies. To get further insight two modifications of this are investigated here, where (i) the rotating part in the Couette cell is placed off center and (ii) apply oscillating rotation instead of continuous rotation as applied usually [4].

Methods: Experimenst have been performed on a 300 MHz Bruker AvanceIII spectrometer with a Micro2.5 microimaging accessory and an in-house built rheo NMR system based on a servo motor , avoiding any vibrations. For the oscillatory shear a crank mechanism has been introduced between the motor and the drive of the Couette rotor.

Results and Discussion: Measuring the flow profiles is crucial in both modifications discussed above. In particular for low-viscosity liquids like dilute solutions or lower molecular weight polymers flow pattern deviating from the expected linear velocity gradient are observed. Around the turning point in the oscillatory shear counterflow is observed which leads locally to a shear rate larger than the gap averaged shear rate applied when the angular velocity is at its peak value. For a rotor off the center a counter rotating flow is seen as well in the wider part of the cell.

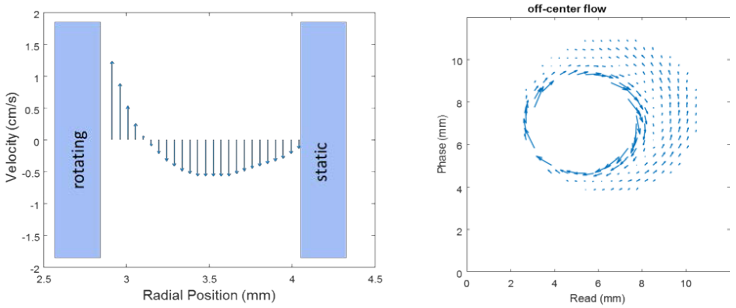

Figure 1: Flow profiles measured combining PFG NMR with imaging. Left: radial flow profile in oscillatory motion in a centered coquette cell just after the turning point exhibiting the counterflow. Right: Two-dimensional flow profile for the cell with the rotor off centered.

Conclusions: Rheo NMR proving very detailed insight in the molecular response to external shear. In addition NMR imaging enables measuring flow profiles in the exact system applied for the investigation of molecular parameters, which is crucial for the interpretation of shear effects in a more complex experimental setup.

References: [1] Ohgo et.al. JACS (2008). [2] Morimoto et. al., Analytical Chemistry (2017). [3] Kohn et. al. Polymer(2018) [4] Kuczera et. al., Langmuir, 2018

Magnetic resonance imaging to assess transport properties of porous media due to dissolution and precipitation processes

A.Pohlmeier[1], J. Poonoosamy[2], S. Haber-Pohlmeier[3], M. Klinkenberg[2], D. Bosbach[2], G. Deissmann[2]

[1]Research Center Jülich, IBG-3, Jülich, Germany.
[2]Research Center Jülich, IEK-6, Jülich, Germany.
[3]RWTH Aachen University, ITMC, Aachen, Germany,

Introduction: Precipitation/dissolution processes often occur in engineered systems in the subsurface such as mineral mining, at interfaces in concrete structures and rocks, or due to carbon dioxide sequestration. Thus, pore space is modified and flow and transport processes are strongly affected leading to dynamic changes in porosity-permeability. 3D non-invasive imaging is mandatory for the understanding and theoretical description of these processes. In this work we conducted flow-through column experiments – according to the experimental concept of Poonoosamy et al. [1, 2]- to investigate the effect of barite precipitation following dissolution of celestine and consequential permeability changes: $SrSO_4(s) + BaCl_2(aq) \rightarrow SrCl_2(aq) + BaSO_4(s)$.

Methods: The relaxation properties of the original and reacted materials were determined by CPMG and IR relaxometric imaging at high field, as well as by 2-dimensional T_2-T_2 correlation experiments at low field using a Magritek tomograph at B_0 = 0.6 T to gain information about the pore connectivity. For monitoring the pore space changes due to barite precipitation, a flow-through column of 1.5 cm diameter was placed in the Bruker scanner with a WB insert at B_0 = 4.7T and scanned under continuous flow from bottom to top, with simultaneous monitoring of the pressure increase. We determined T_2 as well as T_1 maps by multi-echo multi-slice and an IR-single echo multi-slice sequence with normalization on a reference image, respectively [3].

Results and Discussion: The longitudinal relaxation time in both, barite and celestine compartments of (2.6 ± 0.1) s was identical to that of bulk water, meaning that the pore walls have no influence on T_1 despite of the relative small pore size of 10 to 100 µm. In contrast, T_2 decreased unambiguously from 13 to 10 ms during the precipitation and additionally showed a distinct dependence on the echo time. This indicates that the relaxation is controlled by diffusion in internal gradients, not by surface relaxivity changes. The T_2 map showed a homogeneously progressing front of barite in the celestine packing over a period of 5 weeks, characterized by short T_2, and constant T_1.

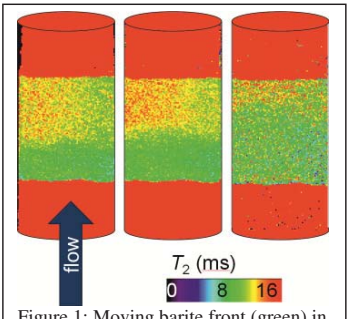

Figure 1: Moving barite front (green) in the celestine packing (yellow-orange).

Conclusion:
NMR relaxometry and MRI allows the detailed characterization of the distribution of precipitates forming in porous media and associated changes in pore geometry. In combination with pressure monitoring the image series allows the derivation of realistic porosity-permeability relations, which can be used in reactive transport simulations.

References: [1] Poonoosamy J., et al. J. Contam. Hydrol. (2015), [2] Poonoosamy et al. Geochim. Cosmochim. Acta (2016),[3] Haber-Pohlmeier et al. Wat. Res. Res. (2017)

Development of a versatile fluidic 3D printed device for NMR and MRI studies: application on hyperpolarized xenon studies

C. Boutin[1], G. Carret[2], E. Léonce[1] and P. Berthault[1]

[1]NIMBE, CEA, Gif-sur-Yvette, France ; [2]Cortecnet, Gif-sur-Yvette, France

Introduction: NMR suffers from weak sensitivity and as hyperpolarization is a non-equilibrium state, the effective dissolution and/or fast delivery of hyperpolarized species in the NMR detection area is a key step. We have developed a series of devices combining fluidics and micro-detection in this purpose. We present here three different applications of it and the corresponding methods to laser-polarized xenon.

Methods: Two families of fluidic devices have been built using a 3D printer. They are both based on a microsized NMR detection associated with a bubble pump which allows a circulation of the sample. The first version is installed on a commercial microimaging NMR product [1], the second one is more versatile and is inductively coupled with the NMR probe. [2]

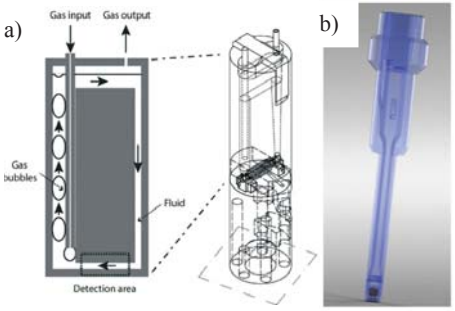

Fig. 1: 3D printed devices based on a bubble pump. a) plugged on a commercial microimaging NMR probehead, b) inductively coupled to the NMR probehead.

Result and discussion: First, the devices have been characterized: ^{1}H velocimetry experiments have given information on the speed of the liquid in the detection region and the dissolution efficiency of hyperpolarized xenon has been estimated. Then the interaction between hyperpolarized xenon and a cage-molecule has been studied.
Biocompatibility of the devices for cell culture is obtained thanks to parylene coating. The effect of this coating has been assessed by cell culture assays of mammalian cells and the ability to made dynamic studies using hyperpolarized xenon has been validated by the addition of toxic on yeasts.
Finally, the device has been modified in order to study of the interaction between gases and powders. The dynamic of the interaction between hyperpolarized xenon and some porous materials has been investigated.

Conclusion: This work demonstrates the possibility to use these versatile devices based on a bubble pump, fluidic channels and micro detection with hyperpolarized species and open a wide range of applications.

References: [1] Causier *et al.*, 3D-printed system optimizing dissolution of hyperpolarized gaseous species for micro-sized NMR, Lab on a chip. (2015) 15 (9), 2049-2054. [2] Carret *et al.*, Inductive Coupling and Flow for Increased NMR Sensitivity, Anal. Chem. (2018) 90 (19), 11169–11173.

T_1-T_2* Relaxation Correlation – Speciation in Solid-Like Materials

B. Balcom[1], *B. MacMillan*[1], *R. Enjilela*[1], *F. Marica*[1], *A. Afrough*[1]
[1]University of New Brunswick, Fredericton, Canada,

Introduction: Low field MR analyses most commonly rely on T_2 lifetime measurements. Modification of the T_2 measurement to include a T_1 dimension has made the T_1-T_2 measurement a very powerful analytical technique. The T_1-T_2 measurement is uniquely well suited to characterization of the pore size distribution in porous materials and speciation of ^{1}H bearing fluids in a wide variety of materials including foods [1-2]. However, in a wide range of materials the T_2 lifetime is too short to permit T_1-T_2 measurement.

In such cases a T_1-T_2^* measurement is a useful analog to the T_1-T_2 experiment. T_1-T_2^* measurement enables one to differentiate species as a function of T_2^* in one dimension and T_1 in the other dimension. The T_1-T_2* measurement permits speciation of ^{1}H in solid-like materials. Monitoring changes of the T_1-T_2^* coordinate, and associated signal intensity changes, reveals structural changes in samples monitored as a function of time.

Methodology: The measurement is a conventional bulk inversion recovery or saturation recovery measurement with full sampling of the resulting FID. The 2D distribution function $f(T_1, T_2^*)$ is recovered by inversion of the data set via a 2D Fredholm equation of the first kind, more commonly known as a 2D inverse Laplace transform.

The method is tested by monitoring change in the water environment and water population of initially dry but well cured 0.45 w/c mortars undergoing imbibition. The measurement may be spatially resolved through adiabatic inversion with slice selection as described by Vashaee [3] for a local T_1-T_2 measurement.

Results: The results of Fig. 1 show two water environments in a 0.45 w/c ratio mortar. The shorter lifetime T_1-T_2* population is assigned to interlayer water. The longer lifetime T_1-T_2* population is assigned to pore water. The minimum transverse lifetime observable is limited by the RF probe deadtime, which is significantly shorter than the minimum echo time in most instruments. The sampling time is dramatically less for T_1-T_2* being limited by the dwell time as opposed to the echo time for the T_1-T_2 measurement.

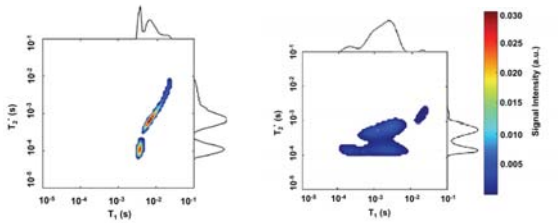

Fig. 1: Water population and environment change revealed by T_1-T_2* relaxation correlation measurement of an initially dry 0.45 w/c mortar imbibing water for 8 hours (left) and 132 hours (right).

The water populations and water environments change dramatically with imbibition of water as shown at 8 hours and 132 hours of imbibition. The permeability of such mortars is well known to change dramatically at times intermediate between these values [4]. As suggested by these results, there is a pore level change in morphology which reduces permeability.

Conclusion: The mortar imbibition example illustrates clearly the potential of this simple method to monitor change in population and environment of ^{1}H species in short signal lifetime systems inaccessible to T_1-T_2 measurement. The approach may however be generalized to many industrially significant solid-like systems where one seeks to determine composition.

References: [1] Song et al, JMR 2002. [2] Song, Prog NMR Spec 2009 [3] Vashaee et al, JMR 2018. [4] Taylor et al, J. Mat. Sci. Lett. 1999.

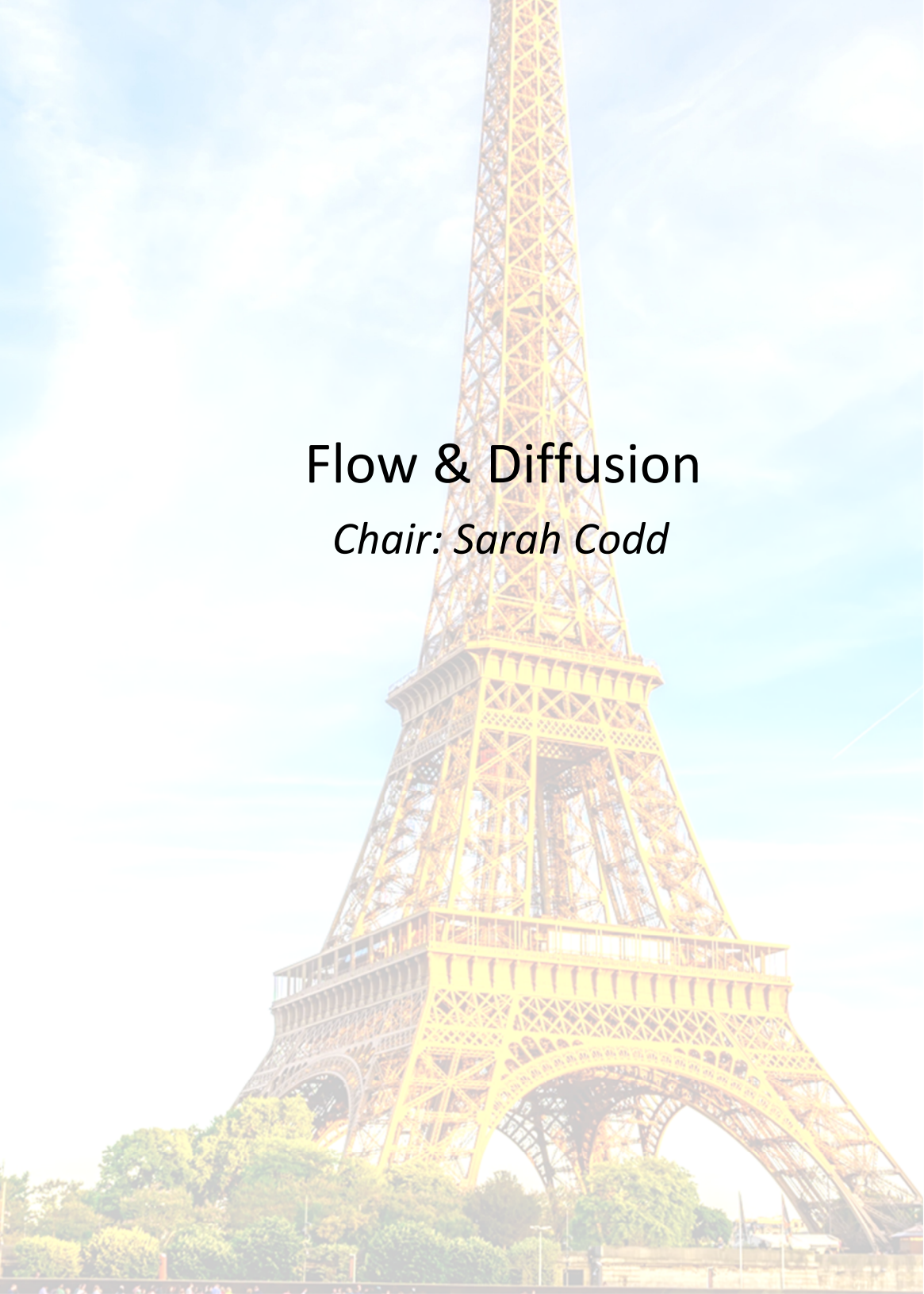

Flow & Diffusion

Chair: Sarah Codd

Magnetic resonance methods for studying reactions in trickle bed reactors at operando conditions

Q. Zheng, J. Williams, L.R. van Thiel, C. Terenzi, M.D. Mantle L.F. Gladden and A.J. Sederman

Magnetic Resonance Research Centre, Department of Chemical Engineering and Biotechnology, University of Cambridge, UK

Trickle bed or packed bed reactors are widely used for heterogeneous catalytic process. Improving the performance of the reaction process remains a long-standing challenge because of the difficulty in measuring the actual conditions and concentrations at the scales of both the reactor and catalyst pellet. The motivation for this work is to use magnetic resonance (MR) to measure and understand what is happening inside the pore space of catalyst pellets operating in a trickle bed reactor at realistic conditions (220°C and 36 bar). This work focusses on the application of MR methods to Fischer-Tropsch synthesis which is particularly challenging because of the large number of chemically-similar products that will exist within the reactor. These cannot be separated by 1D ^{1}H spectroscopy due to susceptibility induced line broadening and so other MR methods must be used to obtain information on product distributions. Experiments have been used to spatially map product evolution and the characteristic molecular diffusion coefficients of molecular species within the bed. Figure 1 shows how the spatial distribution of liquid products varies between 2 and 4 days of time on stream. Identification of the composition of those products has been made with diffusion measurements - since all products formed in the Fischer-Tropsch synthesis are hydrocarbons, there is a relationship between the distribution of diffusion coefficients and the distribution of hydrocarbons in the product. From high resolution spatially resolved diffusion measurements, and through suitable calibration, it is possible measure inter and intra pellet product distribution. We show that the product distribution in the pellets is significantly different from that extracted at the outlet of the reactor, which has implications for future reactor design and operation.

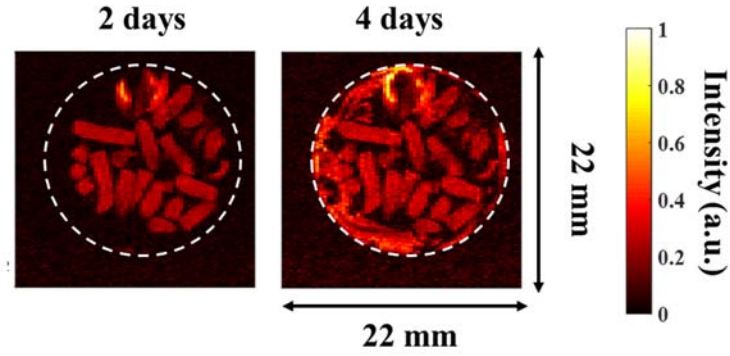

Figure 1. Spatial distribution of products during Fischer-Tropsch synthesis after 2 and 4 days of reaction. Individual catalyst pellets can be seen in the images and the reactor wall is identified by the dashed white line.

Measuring the velocity of gas and particles in and around a single bubble in a 3D fluidised bed

Nick Rice[1], *Chris M. Boyce*[2], *Andrew J. Sederman*[1], *Lynn F. Gladden*[1], *Daniel J. Holland*[3]
[1]Department of Chemical Engineering and Biotechnology, University of Cambridge, Cambridge, United Kingdom
[2]Department of Chemical Engineering, Columbia University, New York, USA
[3]Department of Chemical and Process Engineering, University of Canterbury, Christchurch, New Zealand

Introduction: The flow of gas and particles in gas-solid fluidised beds determines the performance of the process, but is not yet well understood. In this paper, we investigate some of the classical models of fluidised beds using MRI measurements of the velocity of both the gas and solid phases.

Methods: Measurements were performed using a novel 11-interval phase encoded velocity imaging sequence [1]. In order to obtain sufficient signal from the gas phase, sulphur hexafluoride gas was used at a pressure of 7.5 barg; poppy seeds were used for the particulate phase. Even with this gas at pressure, MRI measurements of the velocity are still slow. Therefore, a system was developed to inject single, isolated bubbles reproducibly into an incipiently fluidised bed, analogous to a method previously used to study flow inside droplets [2]. Images of the flow of gas and solid are then obtained by averaging measurements from ~16 000 bubbles.

Results and discussion: Figure 1 shows an example of the velocity maps obtained for the gas phase (a) and the particle phase (b). The images clearly show a recirculation pattern in the gas phase that is consistent with the potential flow solution of Davidson and Harrison [3], for these group D particles. From the gas velocity field it is also possible to estimate the through-flow of gas through the bubble and show that this is consistent with the estimate of three times the minimum fluidisation velocity, U_{mf}., as expected. The velocity of the gas in the particulate phase is found to be less than expected in the classical theory owing to the net downward velocity of the particles relative to the rise velocity of the bubble. If the particle velocity is used to correct the expected gas velocity, it is in good agreement with the estimated interstitial velocity U_{mf}/ε_{mf}, where ε_{mf} is the voidage at minimum fluidisation.

Conclusions: This work presents the first measurements of the gas and particle velocity inside single bubbles in a gas-solid fluidised bed. The measurements have been used to investigate fundamental theories of gas-solid fluidisation. In the future, these measurements will be used to help develop new models of the fluid-particle interaction.

References: [1] Boyce, Rice, Sederman, Dennis, Holland, J. Magn. Reson. (2016). [2] Han, Stapf, Blümich, Phys. Rev. Lett. (2001) [3] Davidson, J.F., Harrison, D. Fluidised particles. (1963).

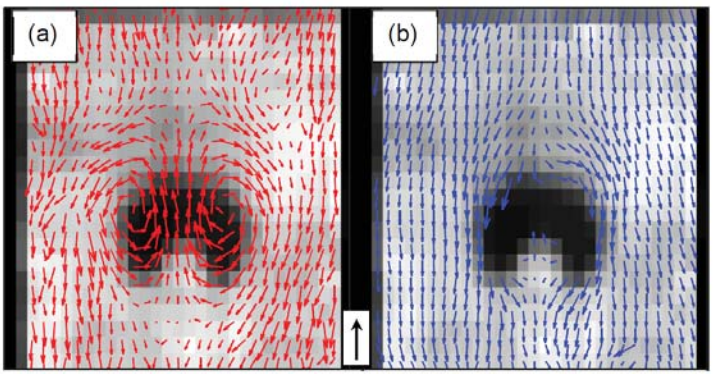

(in blue vectors) shown on an intensity image for the particle phase to illustrate the location of the bubble. The velocity fields are shown relative to the bubble reference frame. The scale of the vector field is shown in the arrow, which for the gas represents a velocity of 0.2 m s^{-1} and for the particles a velocity of 0.1 m s^{-1}. The field-of-view is 60 mm × 60 mm with a slice thickness of 2 mm.

Impact of Fluctuation Induced Asymmetric Propagators on the Accuracy of Phase Contrast Velocimetry.

Haitham F.I. Al-Mubarak[1,2], Antoine Vallatos[1,3],Victor Rodin[1], William M. Holmes[1]

1) Glasgow Experimental MRI Centre, University of Glasgow, UK. 2) Physics department, University of Misan, Iraq. 3) Centre for Clinical Brain Sciences, University of Edinburgh.

Introduction: Phase contrast velocimetry (PCV) is widely used to image velocity fields non-invasively. An often overlooked assumption in the theory of PCV, which may not be met in complex or unsteady flows, is that the intravoxel displacement distributions (propagators) are symmetric. We have shown that higher moments of the displacement distribution (variance, skewness and kurtosis) can significantly impact the accuracy of PCV [1], with phase error,

$$\varphi_{error}(\boldsymbol{r}) = tan^{-1}\left(\frac{-\frac{q^3}{3!}Skew(P_\Delta(R,r))}{1-\frac{q^2}{2!}Var(P_\Delta(R,r))+\frac{q^4}{4!}Kurt(P_\Delta(R,r))}\right)$$

Here, we present pipe flow measurements up to the transition to turbulence, where rapid intravoxel velocity fluctuations can produce broad, asymmetric displacement distributions and PCV errors.

Materials and Methods: PCV and Fourier Flow Imaging (FFI) were performed on water flow (1 g/L CuSO4) through a straight pipe of 3mm diameter. PCV measurements used a flow compensated gradient echo sequence [Bruker Flowmap, Te = 5 ms , Tr = 20 ms, matrix 64 x 64, FOV 1.0 cm x 1.0 cm, slice thickness 1mm]. Corresponding high-resolution FFI was achieved by acquiring 64 q-values. Measurements were made for a range of flow rates and q values.

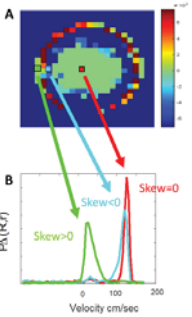

Results and discussion Figure 1a shows example skewness map from FFI (flowrate 508ml/min). b) velocity distribution from selected voxels. The inner wall voxel (green) shows positive skewness and high variance. The second ring closer in (Blue) shows negative skewness and high variance. The central voxel (Red) shows zero skewness and low variance.

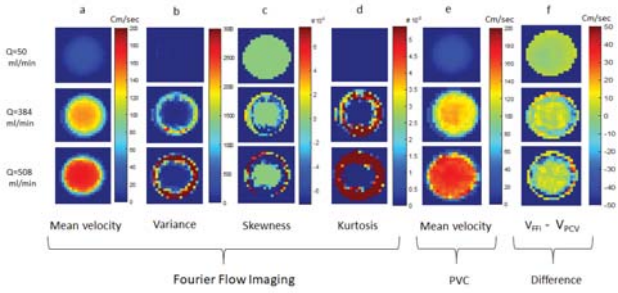

Figure 2, shows FFI and PCV results for three different pipe flow rates. For each FFI voxel the moments of the displacement distribution were calculated, giving spatial maps of the mean (a), variance (b), skewness (c) and kurtosis (d). Column (e) show mean velocity measured by PCV. Column (f) difference/error (FFI-PCV).

- $P_\Delta(\boldsymbol{R},\boldsymbol{r})$ high positive skewness and high variance – **PCV underestimates velocity**
- $P_\Delta(\boldsymbol{R},\boldsymbol{r})$ high negative skewness and high variance – **PCV overestimates velocity**
- $P_\Delta(\boldsymbol{R},\boldsymbol{r})$ zero skewness – PCV accurate velocity

Conclusion. We show that rapid fluctuations in the velocity field, can produce broad asymmetric intravoxel displacement distributions, which can result in an underestimation or an overestimation of the true mean velocity, in agreement with our theoretical analysis [1].

References: [1] Vallatos A, Mubarak H, Holmes W. Journal Magnetic Resonance. 2018; 296:121-129.

Localization regime in diffusion MRI: theory and experiments

N. Moutal[1], K. Demberg[2], D. S. Grebenkov[1], T. A. Kuder[2]
[1] Ecole Polytechnique – CNRS, IP Paris, Palaiseau, France,
[2] German Cancer Research Center (DKFZ) and Heidelberg University, Heidelberg, Germany

Introduction: In 1991, Stoller *et al.* predicted the emergence of the localization regime at high gradients g when the transverse magnetization is localized near boundaries of the sample and the signal E exhibits an unusual stretched-exponential decay: $-\ln(E) \propto g^{2/3}$[1]. We investigated this phenomenon for diffusion of xenon-129 gas inside cylinders and outside an array of rods.

Methods: PGSE experiments were conducted with hyperpolarized xenon-129 gas in 3D-printed phantoms (see [2] for details). Numerical computations of the signal and the magnetization for cylinders were performed with the matrix formalism [3].

Results and discussion: Figure 1(top) shows the signal attenuation inside a cylinder of diameter 2R=3.8 mm. Experimental points are in perfect agreement with the exact solution [3], while its high-gradient behavior is accurately captured by the first two eigenmodes of the Bloch-Torrey operator [4,5], from which we derive:

$$E \approx C \exp\left(-|a_1|\frac{\ell_\delta^2}{\ell_g^2} - \frac{\ell_\delta^2}{R^{1/2}\ell_g^{3/2}} + \frac{\sqrt{3}\,\ell_\delta^2}{2|a_1|R\ell_g}\right) \qquad \text{Eq. 1}$$

where $|a_1| \approx 1.02$, $\ell_g = (\gamma g/D_0)^{-1/3}$, $\ell_\delta = (D_0\delta)^{1/2}$, and C is a slowly decreasing function of g computed numerically from the eigenmodes. This stretched-exponential behavior results from localization of the magnetization near the boundary points at which the gradient is orthogonal to the boundary, see Fig. 1(bottom). Similar behavior was observed for hindered diffusion outside an array of rods [6].

Conclusion: We showed the emergence of the localization regime for both confined and hindered diffusion at gradients as small as 10 mT/m and bD_0 above 4. The high-gradient decay of the signal is reproduced by the asymptotic formula (1) containing no fitting parameters. Our results imply that this behavior is a generic feature of diffusion MRI that can be observed in most scanners. Even though the localization regime is yet poorly understood and exploiting its potential advantages is still challenging, the high sensitivity of the signal to the microstructure at high gradients is a promising avenue for creating new experimental protocols.

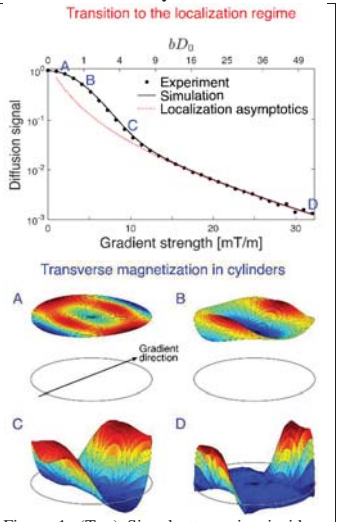

Figure 1: (Top) Signal attenuation inside a cylinder of diameter 2R=3.8mm, obtained with a PGSE sequence with pulse duration δ=6 ms, inter-pulse time Δ=9.34 ms, and gradient strength g ranging from 0 to 32 mT/m. With the estimated free diffusion coefficient $D_0 \approx (3.7 \pm 0.2) \cdot 10^{-5}$ m^2/s, the diffusion length $\ell_\delta = (D_0\delta)^{1/2} \simeq 0.5$ mm, while the gradient length $\ell_g = (\gamma g/D_0)^{-1/3}$ varies from 0.8 mm to 0.25 mm with g. The b-value is $b = \gamma^2 g^2 \delta^2 (\Delta - \delta/3)$. (Bottom) As the gradient increases (four plots correspond to g=2, 5, 10, and 32 mT/m), simulated magnetization is getting more localized near two boundary points.

References: [1] S. D. Stoller, W. Happer, and F. J. Dyson, Phys. Rev. A **44**, 7459–7477 (1991).
[2] K. Demberg, et al., Phys. Rev. E **95**, 022404 (2017).
[3] D. S. Grebenkov, Rev. Mod. Phys. **79**, 1077-1137 (2007).
[4] D. S. Grebenkov and B. Helffer, SIAM J. Math. Anal. **50**, 622–676 (2018).
[5] Y. Almog, D. S. Grebenkov, and B. Helffer, J. Math. Phys. **59**, 041501 (2018)
[6] N. Moutal, K. Demberg, D. S. Grebenkov, T. A. Kuder (submitted to J. Magn. Reson; available online at ArXiv 1904.10877).

Phase error correction to velocity-encoded single-point-imaging measurements using a sawtooth gradient waveform

A. Adair, B. Newling
University of New Brunswick, Fredericton, NB, Canada

Introduction: Pure phase encoding imaging sequences can be modified to include motion-sensitisation by superimposing bipolar pulsed field gradients (PFG) during the encoding intervals. In particular, motion-sensitised SPRITE has been shown to be an effective tool for measuring the flow field in fast, turbulent, and two-phase flows [1, 2]. Rapidly-switching, large-amplitude magnetic field gradients introduced by the bipolar PFG produce significant eddy currents. Therefore, the sample experiences an undesired gradient waveform, resulting in k-space and phase errors (image artefacts and incorrect velocity values).

Existing methods for correcting these errors can result in considerable additional measurement time [3]. We propose a motion-sensitised, pure phase encoding SPI measurement with a simple, repeating sawtooth gradient waveform [Fig.1]. Sequence timing is chosen such that the sample experiences a linear gradient ramp during the phase encoding interval, thus eliminating the k-space and phase errors prior to data acquisition, unlike motion-sensitised SPRITE.

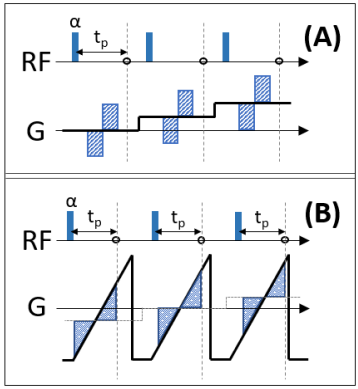

Fig. 1: (A) SPRITE pulse sequence with superimposed bipolar PFG for motion-sensitisation (B) Motion-sensitised SPI sequence with a sawtooth gradient waveform. The linear gradient ramp gives PFG with triangular lobes (as shown). Different k-space points are selected by changing the start time of the phase-encode interval t_p relative to the start of the linear ramp.

Methods: A water sample flowed through a pipe constriction placed in a 4.7 T superconducting magnet. The motion-sensitised SPRITE measurement was repeated with different amplitudes of the PFG. Velocity maps were created from these data for three cases: (i) no eddy current correction, (ii) correction using images of stationary fluid, and (iii) correction by adjustment of the relative areas of the bipolar PFG lobes ("trimming") [2, 3]. A measurement was then performed using the motion-sensitised sawtooth gradient waveform sequence with the same flow parameters. Different q-space points were acquired by varying the slope of the linear gradient ramp.

Results and discussion: Velocity maps of water flowing through the pipe constriction show expected results. When no eddy current correction is used, the velocity values are nonsensical due to the phase errors. Motion-sensitised SPRITE with stationary data correction and trimming correction gives velocity values that agree with theoretical expectations (although both require significant additional measurement time). Motion-sensitised SPI with the sawtooth waveform produces velocity maps, which are compared with the trimmed measurements.

Conclusions: Significant eddy currents produced during motion-sensitised SPRITE measurements cause the sample to experience an undesired magnetic field gradient waveform, resulting in k-space and phase (velocity) errors. A linear gradient ramp during the phase-encoding interval ensures that the bipolar PFG is balanced about the midpoint of the phase-encoding interval, thus mitigating k-space and phase errors. Velocity maps created using a sawtooth gradient waveform are presented.

References: [1] Sankey, et al., J. Magn. Reson. (2009). [2] Adair, et al., Magn. Reson. Imaging (2018). [3] Adair, et al., J. Magn. Reson. (2019).

Intact Plant MRI: up and down during 40 years

Henk Van As
Laboratory of Biophysics, Wageningen University, Wageningen, the Netherlands

Introduction: Modern plant breeding needs to increase agricultural productivity under changing climate conditions while decreasing the ecological footprint. Therefore, there is a strong need to characterize plant genotypes in relation to dynamic environmental (stress) conditions based on photosynthesis, water use efficiency and plant performance. Xylem and phloem transport in plants (Fig. 1) are considered key traits for such phenotyping [1]. Several methods are available to measure parameters related to plant water status [1,2]. PFG-MRI propagator measurements are the most powerful, both for xylem and phloem flow.
Intact plant (mobile) MRI hardware and methods have been developed during the last 40 years that allow to measure long distance transport in relation to the study of photosynthesis and plant water status in an integrative way [1].

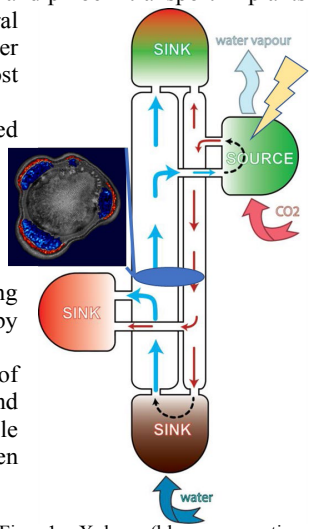

Fig. 1: Xylem (blue, connecting uptake and transpiration) and phloem (red, from source leaves to growing/storage tissues, the sinks) transport in plants. In the cross-sectional image of the stem xylem and phloem flow is overlaid on a proton-density image.

Methods: Propagator measurements in the stem of intact plants by PFG-STE-RARE. Exchange between flowing water and non-flowing water can (strongly) affect the results [3] and has been tested by varying big delta values.
Dedicated lab-based MRI systems (with control/monitoring of microclimate parameters, light intensity, temperature, humidity) and (low field) portable NMR/MRI systems for *in situ* use are available since then 80s [4,5] and have further been developed in the last ten years [6-8].

Results: Long distance flow has been studied as a function of light intensity, photoperiod, fruit pruning, drought stress (tomato plants) and developing strong sinks (tubers) in the root part (potato genotypes with different phloem area), flooding (anoxic root condition that limits sucrose uptake from phloem, Ricinus) reveals that xylem velocity and flux scales with transpiration, but phloem flux is regulated by varying the flow conducting area, not the velocity [9]. At the same time the sucrose content of phloem varied (at higher B_0 reflected in the T_2 of phloem sap), and thus the viscosity. This may stimulate exchange between flowing water and non-flowing water in companying cells. Since propagators and flow results were independent of big delta values (50-150 ms), flow conducting area and velocity were not affected by exchange [9].

Conclusion: MRI can be used for in depth plant phenotyping, eg based on transport traits. Phloem flux is limited by the phloem conducting area present in plants, and can inhibit photosynthesis under optimal photosynthetic conditions! Breeding should include optimizing maximum phloem conducting area in relation to optimizing photosynthesis efficiency. MRI can be of help.
MRI at higher field strengths (2 a 3 T or higher) allows to relate phloem flow characteristics and phloem sap sucrose content in relation to photosynthetic activity. Portable MRI becomes available for phenotyping *in situ*. Due to the low B_0 no info on phloem sucrose is available by such systems.

References: [1] Van As & van Duynhoven, J Magn Reson (2013). [2] Van As, J Exp Bot 2007. [3] Homan et al, Phys Chem E (2010). [4] Reinders et al, J Exp Bot (1988). [5] Van As et al, J. Exp Bot (1994). [6] Windt and Blümler, Acta Hort (2013). [7] Nagata et al, J Magn Reson (2016). [8] Sidi-Boulenouar et al, J Sensors & Sensor Systems (2018). [9] Prusova, PhD thesis Wageningen (2016).

France Life Imaging

The French network of in-vivo imaging

The **France Life Imaging** – FLI – network was launched in 2012 to ensure high technological innovation in biomedical imaging and to offer an open access to the academic, clinician and industrial community to state-of-the-art in-vivo imaging technologies and integrated services. FLI's mission is to increase the French visibility in Europe and worldwide. This infrastructure is coordinated by the CEA (French Alternative Energies and Atomic Energy Commission)

With a 37 **million euros funding over 8 years**, FLI more specifically aims at:

- **Coordinating methodological, preclinical, translational and clinical research in in-vivo imaging at the French level**,
- Developing and enhancing the service offering in in-vivo Imaging in France,
- **Developing partnerships between academic laboratories, clinicians and industries,**
- **Reinforcing the visibility of the French imaging facilities in Europe and internationally**
- **Promote the training** of the staff of the facilities and the students.

RESPORE is the Ile-de-France network in porous solids science. It brings together world-class teamsin the fields of physics, chemistry, engineering, biology, health, mod elling and characterization of materials.

By bringing together communities from different families of porous solids, Respore wants to generate new scientific breakthroughs at the interface of the disciplines represented, and to create added value to meet the current societal challenges.

The Ile-de-France Region has a policy of supporting research networks in targeted areas: these are the Areas of Major Interest (DI

M). The objective of DIMs is to strengthen the scientific influence of the Ile-de-France region and to make of it one of the most attractive regions on a European and international scale.

Electrochemical

Chair: Michael Johns

In situ nuclear magnetic resonance microscopy of batteries and supercapacitors

C.E. Dutoit,[a,b] G. Oukali,[a,b] M. Tang,[a,b] E. Raymundo-Piñero,[a,b] V. Sarou-Kanian,[a,b] M. Deschamps[a,b] and E. Salager[a,b]

(a) CNRS-CEMHTI UPR3079, Univ. Orléans, Orléans, France
(b) Réseau sur le Stockage Electrochimique de l'Energie (RS2E), FR CNRS 3459, Amiens, France

Lithium-ion batteries and supercapacitors are complex composite storage devices. Batteries store energy through redox reactions in the electrodes while supercapacitors function through the reorganization of the ionic charges in the electrolyte soaking nanoporous carbon electrodes. *In situ* measurements are essential to capture and understand their current limitations in terms of power and stored energy.

In some cases, the signals of the components of the battery/supercapacitor overlap in *in situ* measurements. The combination of spectroscopy and imaging can give access to localized chemical information on the components of interest, but their short dephasing times makes it challenging. Classical methods (such as standard chemical shift imaging) based on echoes do not detect those relevant components in the device.

We develop and apply approaches to circumvent those issues. We managed to record[1] *in situ* the ^{7}Li signal in the thick electrodes of a lithium-ion battery with a resolution of 100 µm. Limitations during fast charge were identified and characterized thanks to those localized measurements. For supercapacitors we also managed to obtain the 1D concentration profiles of the electrolytic ions in the porosity of the electrodes.[2] Those measurements bring insight into the parameters that influence the charge mechanism.

[1] M. Tang, V. Sarou-Kanian, P. Melin, J.-B. Leriche, M. Ménétrier, J.-M. Tarascon, M. Deschamps, E. Salager, *Nat. Commun.* **2016**, *7*, 13284.
[2] G. Oukali et al., *submitted* **2019**.

Quantitative T_1 Imaging for Battery Characterisation

Claire L. Doswell[1], Yasmeen M. AlZahrani[1], Melanie M. Britton[1]
[1]School Of Chemistry, University of Birmingham, Birmingham, UK

Introduction: Current lithium-ion batteries have problems with sustainability and safety [1], hence new battery technologies are being sought which can address these issues. As a consequence, new electrodes and electrolytes are being developed. However, in addition to new materials, new characterisation techniques are also required that enable *in situ*, real time monitoring of chemical processes across the electrode and electrolyte. Nuclear magnetic resonance (NMR) methodologies offer non-invasive characterisation of the chemical compositions of such materials, which can then be spatially-resolved using magnetic resonance imaging (MRI) [2,3]. Using MRI, we have been investigating novel ionic liquid (IL) battery electrolytes. By using the NMR relaxation time of the IL, we are able to map the distribution of chemical species within the IL enabling *in situ* visualisation of battery chemistry [4]. However, the variation in relaxation times can sometimes be small and, therefore, it is important to maximise the signal-to-noise ratio (SNR) to reduce the T_1 standard deviation (σ) and enable quantitative and accurate determination of relaxation times. A systematic study has been undertaken to investigate and optimise the influence of experiment type, signal averaging, and echo summation on the SNR. These techniques have been employed to quantitatively map the composition of ILs for novel battery applications.

Methods: ^{1}H and ^{19}F MRI T_1 maps of a series of $CuSO_4$ concentrations and an IL respectively were acquired using a RARE pulse sequence with either saturation recovery or inversion recovery methods, and analysed by summing the echo images or using the first echo image. The average T_1 and σ values were determined for each different solution as a function of experimental parameters.

Results and Discussion: By comparing the T_1 maps for a series of $CuSO_4$ concentrations, it was demonstrated that inversion recovery resulted in a lower σ than saturation recovery. As expected, signal averaging improves the SNR, and decreases the σ, but increases the experiment time. However, by summing multiple echoes it was possible to increase the SNR, and decrease the σ, without increasing the experiment time. When the optimised methodology was applied to observe the absorption of water in an IL, the change in T_1 became observable on a timescale sufficiently rapid to detect the ingress of water.

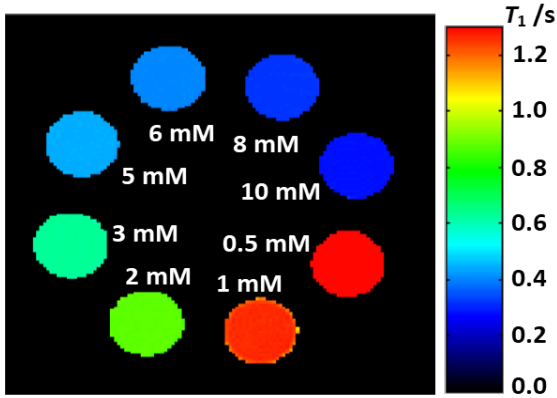

Fig. 1: ^{1}H T_1 map of the $CuSO_4$ phantom determined using an inversion recovery experiment.

Conclusion: A systematic study exploring methods for reducing noise in T_1 maps has been performed. It was found that the SNR can be improved, and the standard deviation decreased, by increasing signal averages. However, this comes at a cost of increased experimental time. An alternative method was to sum the echo images, which does not result in an increase in experimental time.

References: [1] Grey, Nat. Matter. 16 (2016) 45. [2] Britton, Chemphyschem, 15 (2014) 1731. [3] Bray, Angew. Chem. Int. Ed. Engl. 55 (2016) 9394. [4] Britton, J. Phys. Chem. Lett. 4 (2013) 3019.

Current Density Imaging in Lithium-Ion Batteries

I. Serša[1], U. Mikac[1]
[1]Jožef Stefan Institute, Ljubljana, Slovenia

Introduction: Development of new and more efficient batteries is one of the main priorities worldwide. With the introduction of lithium-ion batteries, batteries became lighter, had higher energy density and less memory effects than most previous types of batteries. However, with lithium batteries there are still several unsolved problems, among which growth of dendrites is the one that severely impedes further development of the batteries. Growth of dendrites on lithium metal electrodes poses a great risk of fire in the batteries. Consequently, lithium metal, which would be an ideal anode material and would enable much better battery capacity, is not in use. In this study, MR microcopy is used to study: a) conditions under which dendrites grow in a lithium symmetric cell, and b) how the dendrites influence the flow of electric currents in the cell.

Methods: A symmetric lithium cell as a lithium battery model system [1] was made of 8 mm thick block of peek plastic into which a cubic hole with dimensions 16 x 4 mm^2 was machined. In argon atmosphere, the cell was assembled by filling it with $LiPF_6$ in EC/DMC electrolyte and then sealing it on both sides with a sandwich of a lithium metal foil (electrode), a thin copper wire (electric contact), silicon rubber and a peek plastic side that was screwed on the block. The cell was then inserted into a 9.4 T NMR magnet in an orientation with the electrodes parallel to both B_0 and B_1 magnetic fields thus ensuring optimal reception of the MR signal [2]. The cell was repeatedly scanned with the regular 3D spin-echo and 3D current density imaging (CDI) sequence [3], both at parameters: field of view, 20 x 10 x 5 mm^3, imaging matrix, 128 x 64 x 32, TE/TR, 22/2000 ms. To induce growth of dendrites, between each pair of in total 11 scan blocks, electric charge needed for a transfer of 5 % electrode mass was flown at current densities ranging from 4 A/m^2 to 40 A/m^2 (in different experiments). In the CDI sequence currents of 5 mA were induced in the *xy* plane between the electrodes and then used to calculate current density from the magnetic field change B_{c_z} using the relation $(j_x, j_y) = \left(\partial B_{c\_z}/\partial y, -\partial B_{c\_z}/\partial x\right)/\mu_0$.

Results and discussion: Magnitude and the corresponding current density (CD) images in Fig. 1 clearly show growth of dendrites and how they influence current pathways. In the experiments it was found that the amount of formed dendrites is not dependent only on the transferred electric change, but also correlates with the applied current density. CD images were calculated from just one component of magnetic field change, which is sufficient under assumption that the electric currents are planar. Measured geometry of dendrites enables also simulation of current density distribution and its comparison with the measured one.

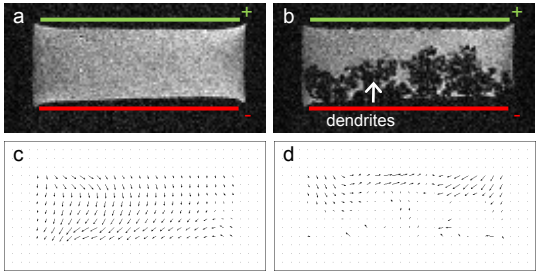

Fig. 1: Central slice ^1H images of the plane between the electrodes (up and down) shown by magnitude images a,b and the corresponding measured vector fields of current density distribution c,d of a fresh cell a,c and after the charge transfer of 50 As at 40 A/m^2 that induced dendrite growth.

Conclusion: In the study it was demonstrated that CDI can be applied also to study current distribution in a model battery and thus enable studying of various current-related phenomena in different battery configurations.

References: [1] Ilott, PNAS (2016). [2] Serša, JMR (2018), [3] Scott, JMR (1992).

In Operando Visualization of Sodium Battery Chemistry by Magnetic Resonance Imaging

Joshua M. Bray[1], Galina E. Pavlovskaya[2], Claire L. Doswell[1], Heather Au[3], Hande Alptekin[3], Maria-Magdalena Titirici[3], Thomas Meersmann[2], Melanie M. Britton[1]

[1] School of Chemistry, University of Birmingham, Edgbaston, Birmingham, B15 2TT, UK. [2] Sir Peter Mansfield Imaging Centre, School of Medicine, University of Nottingham, Nottingham, NG7 2RD, UK. [3] Department of Chemical Engineering, Imperial College, Kensington, London, SW7 2AZ, UK

Introduction: In recent years, there has been increasing interest in sodium ion batteries (SIBs) as a promising alternative to lithium ion batteries (LIBs). In particular, SIBs offer advantages in cost and sustainability over current LIBs, while still providing high energy density. However, despite increased research intensity, SIBs still face significant challenges preventing their commercialisation, which is driving the development of new SIB materials. In parallel with the demand for new SIB materials, there is an equal demand for new *operando* analytical techniques [1-3] to facilitate the identification of optimised electrolytes and electrode materials, and fundamental understanding of the factors controlling the composition and stability of the solid-electrolyte interphase (SEI) and the formation of dendrites. ^{23}Na MRI offers a valuable opportunity by which SIBs can be investigated and optimised, as it is possible to visualise the structure and distribution of the electroactive species directly. *In operando* ^{1}H and ^{23}Na nuclear magnetic resonance (NMR) spectroscopy and imaging (MRI) experiments are reported, which identify Na species and map their distribution in the electrode and electrolyte during charge cycling and galvanostatic plating.

Experimental: ^{1}H and ^{23}Na NMR imaging, combined with ^{23}Na NMR spectroscopy, were performed, during galvanostatic cycling and plating in a model sodium-ion battery comprising sodium metal and amorphous carbon electrodes with a 1 M sodium hexafluorophosphate in 1:1 ethylene carbonate:dimethyl carbonate electrolyte.

Results and Discussion *In operando* ^{23}Na nuclear magnetic resonance (NMR) spectroscopy and imaging (MRI) experiments enabled the identification of Na species and map their distribution in the electrode and electrolyte during charge cycling and galvanostatic plating [4]. The formation and evolution of sodium dendrites were observed by ^{23}Na NMR spectroscopy and MRI and the formation, growth and microstructure of these dendrites were visualised by three-dimensional (3D) ^{1}H MRI of the electrolyte.

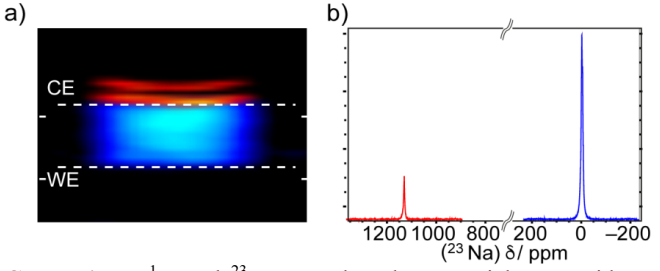

Fig. 1a) 2D ^{23}Na MRI of sodium in Na metal (red) counter electrode (CE) and electrolyte (blue). The position of the CE and carbon working electrode (WE) are indicated with dashed lines. b) ^{23}Na NMR spectra for Na in the electrolyte (blue) and Na metal electrode (red).

Conclusions: ^{1}H and ^{23}Na MRI has the potential to provide a step change in understanding of performance and failure mechanisms in SIBs.

References: [1] Britton *Prog. Nucl. Magn. Reson*. Spec. **101** (2017) 51 [2] Britton, et al. *J. Phys. Chem. Lett.* **4** (2013) 3019 [3] Bray et al. Angew. Chem. 55 (2016) 9394 [4] Bray et al. *under revision.*

Cell Casing Design for *in situ* Nuclear Magnetic Resonance Imaging on Electrochemical Systems

Roland Balbierer [a], *Gisela Guthausen* [a, b]

[a] Institute of Mechanical Process Engineering and Mechanics, KIT, 76131 Karlsruhe, Germany

[b] EBI, Chair of Water Chemistry and Water Technology, KIT, 76131 Karlsruhe, Germany

Introduction: MRI was successfully applied to study Li^+ concentration gradients developing under an applied electric current [1]-[3]. Ion transport properties can be extracted and impact modeling of migration and diffusion processes of a battery. Essential for MRI experiments is a proper cell design in order to rely on genuine electrolyte properties. Assembly remains a critical factor, due to possible side products occurring during electrode formation or residual moisture leading to Li^+ loss.

Methods: A cell casing was developed, providing sufficient chemical resistance by using polyether ether ketone (PEEK) and perfluorocarbon rubber (FFPM) sealing. Electrical connectivity was realized with standard terminals and micro spring connector. The presented approach intended to avoid metallic lithium or artificial electrodes and the parts were constructed such that requirements for re-usability are fulfilled. 1D and 2D spin-echo and gradient-echo MRI techniques were used to image the electrolyte volume (700 µL of 1 M EC/EMC = 50/50 (v/v) with 11 x Whatman GF/B separators) of a working lithium-ion battery (LIB) with Graphite (C) as anode material and different cathodes, i.e. Lithium-Manganese-Oxide (LMO) and Lithium-Nickel-Manganese-Cobalt (NMC).

Results and discussion: The concentration gradient was generated by constant current charging and investigated by 1D spin-echo ^{7}Li MR imaging. Adequate potential ranges for the materials were applied. With a variation of an automated processing method [4] the electrolyte and ion distribution between NMC/C electrodes along *z* was analyzed. The electrolyte distribution in the axial plane was investigated by ^{1}H MRI and demonstrates gas locks or other impurities due to assembly.

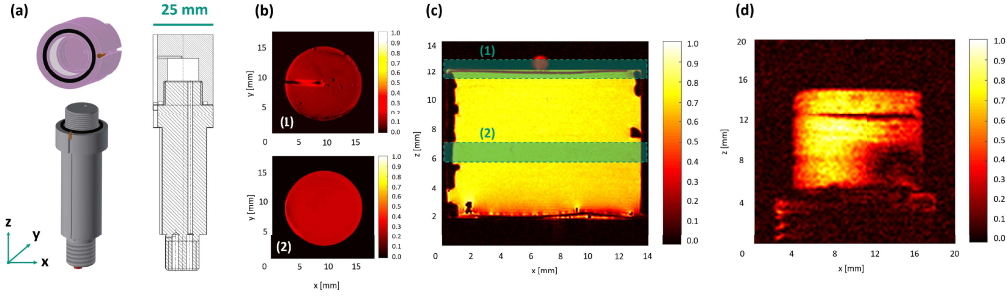

Fig.1: **(a)** Schematic drawing of the cell casing **(b)** Axial ^{1}H MR intensity images (2D MSME) of a working LMO/C battery cell revealing current collector contact by Cu-wire on top (1) and a homogeneous electrolyte distribution in separator stack (2). **(c)** Coronal slice indicating the location of the axial slices between the electrodes C on top and LMO at the bottom **(d)** ^{7}Li MRI (2D FLASH) coronal slice of the NMC/C battery cell with an artefact at the bottom right.

Conclusion: Electrochemical characterization of the cell and concentration profiles were measured within the presented design. The electrode diameter and electrolyte volume are adjustable by variation of screwable counterpart and hence readily applicable.

References:

[1] Klett M. et al., J. Am. Chem. Soc. (2012), 134:14654, DOI: 10.1021/ja305461j
[2] Krachkovskiy S. et al., J. Phys. Chem. Lett. (2013), 4:3940, DOI: 10.1021/jz402103f
[3] Klamor S. et al., J. Phys. Chem. Lett. (2015), 17:4458, DOI: 10.1039/c4cp05021e
[4] Balbierer R. et al., J. Mater. Sci. (2019), 54:5682, DOI: 10.1007/s10853-018-03253-2

LIST OF POSTERS

POSTER LIST

Odd numbers will be presented on Monday. August 19th.
Even numbers will be presented on Tuesday, August 20th.

Posters with a ★ participate in the poster competition.

MR Microscopy

P01 | Artifacts in UTE images reflect the differences in the eddy-current compensation between changing the applied shim currents versus shifting the rf frequency
Yang Xia, Farid Badar, Dieter Gross, Thomas Oerther

P02 | ★ Design of a lamellar phantom for validation of in vivo diffusion MRI methods
Hong Jiang

P03 | Diffusion tensor distribution imaging of in vivo mouse brain at ultra-high magnetic field using spatiotemporal encoding
Daniel Topgaard, Maxime Yon, Lucio Frydman

P04 | Ultra high-field (17.6T) magnetic resonance microimaging reveals dysfunction of the circadian master clock in Alzheimer´s disease brain
Alia Alia, U Roy, S Roßner

P05 | Multicomponent T2 relaxation analysis in the muscles of Zebrafish
Muhamed N.h. Eeza, N Nowik, Y Ding, Z Zuberi, J Matysik, H.p. Spaink, Alia Alia

P06 | Identification of water compartments in spinal cords by deuterium double quantum-filtered NMR *Uzi Eliav, Hadassah Shinar, Gil Navon*

P07 | An in vivo Continuous Sequential 3D MRM Study of Honey Bee Metamorphosis
Ales Mohoric, Jani Božič, Kaja Tušar, Yining Ye, Ana Sepe, Ursa Mikac, Igor Serša

P08 | Minimally invasive implantable NMR microcoil for in vivo MRS and MRI in submicroliter volumes *Yannick Crémillieux, Vi Thi Thuy Pham, Noël Pinaud, Alan Wong*

P09 | 3D MR Microscopy with 6D Diffusion-Relaxation Distributions
Linn Thrane, Daniel Topgaard, Hong Jiang

P10 | Spatial encoding magnetic resonance imaging using quadratic gradients
Sina Marhabaie, Geoffrey Bodenhausen, Philippe Pelupessy

P11 | Wine Cork Evolution during Aging: Insights from MRI Measurements
Jeffrey Walton, Annegret Cantu, Michael Mackay, Greg Hirson, Andrew Waterhouse

Cellular & Molecular

P12 | Temperature dependence of T2 relaxation times in fresh tomato pericarp
Rodolphe Leforestier, Maja Musse, François Mariette

P13 | Site-resolved distribution and molecular dynamics of water within fibril aggregates: from plant cell-wall scale to atomistic resolution
Camilla Terenzi, Pan Chen, Jakob Wohlert, Lars A. Berglund, István Furó

P14 | Using biological magnetization as a tool for bacterial imaging
Raymond Borg

P15 | In-situ NMR highlights structural change during apple heating
Sylvie Clerjon, Alexandre Leca, Catherine Reanrd, Jean-Marie Bonny, Amidou Traore

Engineering & Materials

P16 | Nuclear Magnetic Resonance Multi-Phase Flowmeter & Fluid Analyzer
Feng Deng, Shiwen Chen, Guanhong Chen, Huabing Liu, Lizhi Xiao

P17 | Deposit layer formation during protein filtration by 1D inverse Abel-transformation MRI
Nicolas Schork, Sebastian Schuhmann, Hermann Nirschl, Dieter Gross, Gisela Guthausen

P18 | Deposit layer formation during skim milk protein filtration by MRI
Nicolas Schork, Sebastian Schuhmann, Estelle Amling, Hermann Nirschl, Gisela Guthausen

P19 | A low-cost, miniature Halbach magnet with adjustable homogeneity designed for accurate and immediate detection of blood glucose
Qing Yang, Yi Chen, Rongsheng Lu, Zhonghua Ni, Hong Yi

P20 | Passive radiofrequency shimming for rat head imaging at 17.2 Tesla
Marc Dubois, Tania S. Vergara Gomez, Camille Jouvaud, Abdelwaheb Ourir, Julien De Rosny, Frank Kober, Redha Abdeddaim, Stefan Enoch, Luisa Ciobanu

P21 | Superhydrophobic Surfaces – Examination of the Chemical Composition of Sessile Droplets during Evaporation
Jonas Kind, Christina Thiele

P22 | NMR relaxation and oxygen permeation studies on protein-sugar matrices conditioned at different humidities
Jens Meissner, Nikolaus Nestle, Emma Thompson, Eduard Schreiner, Mireia Subinya Albrich, Fangfang Chu

P23 | A solid echo T1-T2 method for enhancing hydrogen-containing solid NMR signal in hydrated cement paste
Zhengxiu Wu, Xiaowen Jiang, Rongsheng Lu, Zhonghua Ni, Zonghai Xie

P24 | Generation of nuclear magnetic resonance logging curves using Bi-directional LSTM
Li Bo

P25 | Magnetic Resonance Imaging as a Non-Destructive Method for the Characterization of Silicone Elastomer Chemistry In-Situ,
April Sawvel, *Harris Mason, Jennifer Knipe, Sarah Chinn, Elizabeth Glascoe, James Lewicki, Robert Maxwell*

P26 | Exploring the Origins of Diffusive Diffraction behavior in Bottlebrush Polymers
Velencia Witherspoon, *Michal Komlosh, Dan Benjamini, David Vaccarello, Peter Basser*

P27 | Can the coagulation process of cellulose be studied by MRI?
Maria Gunnarsson, Jenny Bengtsson, Leo Svenningsson, Diana Bernin

P28 | Improving magnetic resonance imaging through 3D printing,
Hanne Vanduffel, Dimitrios Sakellariou, Rob Ameloot

P29 | In Situ Magnetic Resonance Imaging of Pharmaceutical Tablet Dissolution
Bruce Balcom, Bryce Macmillan, Heather Frericks-Schmidt, Mark Zell

Hardware

P30 | NMR of chemical reactions at elevated process conditions
Hilary Fabich, Stephen Altobelli, Partha Nandi, Hans Thomann, Mark Conradi

P31 | Design of main control system for nuclear magnetic resonance LWD tool
Xu Yangyang

P32 | A New LWD Magnetic Resonance Imaging Tool
Zhe Sun, Lizhi Xiao, Guangzhi Liao, Yan Zhang, Sihui Luo, Feixue Gong, Zhihao Long

P33 | Study on Evaluation of Vector Matching Effect between B0 and B1
Feixue Gong, Lizhi Xiao, Guangzhi Liao, Yan Zhang, Zhe Sun, Sihui Luo, Zhihao Long

P34 | Circuit Design of NMR Logging While Drilling Device
Yao Wei

P35 | Study on RF coil design in LWD MRI tools with target field method
Zhihao Long, Guangzhi Liao, Lizhi Xiao, Yan Zhang, Zhe Sun, Sihui Luo, Feixue Gong

P36 | Matrix coil design based on target field method for Halbach magnet
Yajie Xu, Ya Wang, Xiaodong Yang

P37 | An open PXIe based scalable MRI console
Robin Dykstra, Sergei Obruchkov, Andrew Ang, Guang Yang

P38 | Q-Switch for Earth-Field NMR Systems
John Zhen, Michael Johns, Paul Stanwix, Einar Fridjonsson

Mobile & Low Feld

P39 | Inside-out NMR with concentric ring magnets
Shin Utsuzawa, Yi-Qiao Song

P40 | A radio frequency coil for non-invasive nuclear magnetic resonance detection of human finger blood glucose
Junnan Wang

P41 | Effect of Radial Vibration on Logging While Drilling NMR T2 Distribution
Hu Lynn

P42 | A Magnet Design of Low Gradient for NMR LWD
Yifan Wang

P43 | Studies of Biofilms in Yellowstone National Park and Violins of the Cremona Masters by Mobile NMR
Denis Jaschtschuk, Christian Rehorn, Michael Adams, Bernhard Blümich, Catherine Kirkland, Brent Peyton, Sarah Codd, Joseph Seymour, Claudia Invernizzi, Marco Malagodi, Valeria Gabrielli

P44 | The Frequency-switchable Transceiver Array with Inductive Decoupling,
Baosong Wu, Yonghyun Ha, Charles Rogers Iii, Kartiga Selvaganesan, Gigi Galiana, R. Todd Constable

P45 | Mini Inside-Out Nuclear Magnetic Resonance Sensor Design for Soil Moisture Measurements
Jiamin Wu, He Yucheng, Xu Zheng

P46 | NMR depth profiling as prerequisite for restauration and conservation of Cultural Heritage
Markus Kueppers, Max Gierth, Bernhard Bluemich

P47 | Toward Inexpensive Magnetically Compensated Materials
Andrew Mcdowell, Fred Mcdowell

P48 | A movable MRI system for brain imaging and its pre-clinical experiments
He Yucheng, Xu Zheng, Wu Jiamin, Tan Liang

P49 | CPMG measurement under motion
Shin Utsuzawa, Irfan Bulu, Tancredi Botto, Jeffrey Paulsen, Martin Hurlimann, Yi-Qiao Song

P50 | Profiling the temperature dependent frequency of a MOUSE® for outlab MRI
Amidou Traore, Rim Alouissi, Abdellatif Benmoussa, Guilhem Pages, Jean-Marie Bonny

P51 | Magnetic Particle Spectroscopy - MObile Universal Surface Explorer
Patrick Vogel, Martin A. Rückert, Thomas Kampf, Volker C. Behr

P52 | Low-field Magnet Assemblies for in operando NMR Studies
Rodrigo De Oliveira Silva, João Marreiros, Arthur Gustavo Araujo-Ferreira, Everton Lucas-Oliveira, Patrick Judeinstein, Willian Trevizan, Jean-Marc Zanotti, Tito José Bonagamba, Rob Ameloot, Dimitrios Sakellariou

Biomedical

P53 | Should we still fit quantitative MRI data to mathematical models in the age of AI?: A case study comparison of deep learning versus the Tofts model
Peter Lee, Alessandro Guida, Thomas Trappenberg, Chris Bowen, Steven Beyea, Jennifer Merrimen, Cheng Wang, Sharon Clarke

P54 | An Image Quality Metric Based Heuristic for Accurate Pharmacokinetic Parameter Recovery using Quantitative MRI
Allister Mason, Nathan Murtha, James Rioux, Sharon Clarke, Chris Bowen, Steven Beyea

P55 | Study on Electrical Properties under Magnetic Resonance with High Field
Xiaonan Li, Guoqiang Liu, Zilong Yuan, Jianfeng Qiu

P56 | Sub-10µm Resolution µMRI Study of Rabbit Cartilage
Yang Xia, Syeda Batool

P57 | Spatially resolved relaxation analysis in bovine and human articular cartilage
Siegfried Stapf, Carlos Mattea, Andrea Cretu, Oleg Petrov

P58 | MRI characterization of long-term brain damage induced by low dose irradiation at two different exposure ages in the mouse
Laura Mouton, Olivier Etienne, Elodie Peres, David Barrière, Fawzi Boumezbeur, François Boussin, Denis Le Bihan

P59 | Estimates of Blood Plasma Water Content Using Portable NMR Relaxometry
Sophia Fricke, Joseph Pourtabib, John Madsen, Shahab Chizari, Johnny Phan, Nam Tran, Matthew Augustine

P60 | PVA Phantom for MRI Study of Myocardial Viability
Victor Rodin, Tom Anderson, Maurits Jansen, Gillian Gray, William Holmes

Hyperpolarization

P61 | Toward in vivo pH Sensing using Hyperpolarized 129Xe MRI
Patrick Berthault, Estelle Leonce, Jean-Pierre Dognon, Delphine Pitrat, Jean-Christophe Mulatier, Thierry Brotin

P62 | Dual Modality Imaging of Powdered Diamond: Optics and Room Temperature Hyperpolarized MRI
Xudong Lv, Fei Wang, Danila Barskiy, Emanuel Druga, Alessandra Aguilar, Benjamin Safvati, Priyanka Raghavan, Tommy Mcknelly, Raffi Nazaryan, Ben Han, Carlos A. Meriles, Jeffrey A. Reimer, Dieter Suter, Jeffrey H. Walton, Ashok Ajoy, Alexander Pines

P63 | A Low-field NMR detector for probing in situ SABRE hyperpolarization
Fraser Hill-Casey, Kieran Marsh, Matheus Rossetto, Meghan Halse

Porous Media

P64 | A new method to correct the effect of saturated hydrocarbon to nuclear magnetic resonance (NMR) T2 distribution in tight porous media
Xiao Liang, Zhang Wei, Xie Xiuhong

P65 | Analysis of 3-site T2- T2 exchange NMR
Yang Gao, Bernhard Blümich

P66 | In-situ CH4-CO2 Dispersion Measurements in Rock Cores
Ming Li, Sarah Vogt, Eric May, Michael Johns

P67 | Using NMR to determine gas storage in shale formation
Boqin Sun

P68 | Characterization of fluid flow through wormholes created by acidification of carbonate rocks: a phase contrast imaging study
Bernd Foerster, Mariane Andreeta, Elton Montrazi, Carlos Speglich, Tito Bonagamba, Fernando Paiva

P69 | Studying molecular diffusion in heterogeneous catalysts on different length scales simultaneously *Emma Thompson, Nikolaus Nestle, Matthias Kellermeier, Hannah Schreyer, Katja Graf, Max Pokrandt*

P70 | Field-dependent effect of clays on NMR T2 relaxation of sedimentary rocks by direct two-scale simulation
Yingzhi Cui, Igor Shikhov, Christoph Arns

P71 | Identification of physical properties governing relaxation process in saturated rocks by matching experimental T2 distributions and CT-image based NMR simulation through surrogate-assisted particle swarm optimization
Rupeng Li, Igor Shikhov, Christoph Arns

P72 | Spatially-resolved T2 distribution mapping in heterogeneous rock model with phase encode MRI *Yushi Cui*

P73 | Data Processing and Software Research of Nuclear Magnetic Resonance Logging While Drilling
Dong Yu

P74 | Characterization of Kerogen and Spent Shale Maturation by Solid State 13C and 1H NMR Spectroscopy
F. Panattoni, P. C. M. M. Magusin, J. Mitchell, E. J. Fordham, C. P. Grey

P75 | Correlation of magnetic resonance imaging and high-resolution X-ray tomography to characterise pore size distributions in polymeric open – cell sponges
Gabriele M. Cimmarusti, Melanie Britton, Abhishek Shastry, Matthieu Boone, Veerle Cnudde

P76 | Study on the molecular interaction of pore surface in tight sandstone by NMR
Hanlin Liu, Guangzhi Liao, Lizhi Xiao, Yan Zhang

P77 | 2.5D spatially resolved 3D Laplace NMR for porous media
Yan Zhang

P78 | Investigation of high-permeability channels using computational fluid dynamics and magnetic resonance imaging
Gustavo Solcia, Bernd Foerster, Mariane Andreeta, Tito Bonagamba, Fernando Paiva

P79 | MRI and NMR Studies of a Seawater Spray Ice Formation
Grant Wilbur, Bryce Macmillan, Igor Mastikhin

P80 | Water diffusion pore imaging on a 14.1 T spectrometer using glass capillary phantoms and strong gradients
Dominik Ludwig, Frederik Bernd Laun, Karel D. Klika, Peter Bachert, Tristan Anselm Kuder

P81 | The bending of 17th century panel paintings induced by moisture
Leo Pel

P82 | T2 Analysis using Artificial Neural Networks
Tristhal Parasram, Dan Xiao

P83 | Setting of geopolymer binders studied by NMR
Nikolaus Nestle, Jan Philip Merkl, Quang Hung Nguyen, Jean-Baptiste D'espinose

P84 | Homogenisation in high-level radioactive waste bentonites probed at submicroscopic length-scales using 2D μ-MRI
Galina Pavlovskaya, Frank Scotti, Sean Rigby, Thomas Meersmann, Katherine Daniels, Antony Milodowski, Jon Harrington

P85 | Liquid specific changes in magnetic susceptibility induced internal gradients during displacement experiments in porous media
Henrik Nicolay Sørgård, John Georg Seland

P86 | Investigation of the Structure of Geopolymer Based Cements with NMR Cryoporometry and Relaxation Exchange Spectroscopy
Sarah Mailhiot, Jing Li, Hari Sreenivasan, Anu Kantola, Paivo Kinnunen, Ville-Veikko Telkki

P87 | Monitoring Gas Hydrate Formation/Dissociation with Magnetic Resonance Imaging in a Metallic Core Holder
Bruce Balcom, Armin Afrough, Mojtaba Shakerian, Sarah Vashaee, Florin Marica, Yuechao Zhao

Electrochemical

P88 | In situ Magnetic Resonance Spectroscopy and Imaging of Li-plating onto and Diffusion within Anodes of Li-Ion Batteries
Sergey A. Krachkovskiy, Kevin Sanders, Andres Ramirez Aguilera, Bruce J. Balcom, Gillian R. Goward

Flow & Diffusion

P89 | The Clinical Application of Diffusion-Weighted Image for Differentiating Myeloma From Bone Metastasis in the Extremities
Seul Ki Lee

P90 | Multi-Region Models for Predicting Features of T1-T2 Experiments
James Maneval, Madison Nelson, Linn Thrane, Joseph Seymour

P91 | Improved one-dimensional and two-dimensional permeability NMR models
Lin Wang, Lizhi Xiao, Yan Zhang, Guangzhi Liao, Wenzheng Yue

P92 | Good statistics from noisy multidimensional distributions
Alexis Reymbaut, Paolo Mezzani, João P. De Almeida Martins, Daniel Topgaard

P93 | Benchtop NMR spectroscopy and diffusion measurements to characterize enzymatic hydrolysis online and at-line
Evan Mccarney, Kate Washburn Washburn, Robin Dykstra

P94 | Probing surface-to-volume ratio in anisotropic media
Nicolas Moutal, Ivan Maximov, Denis Grebenkov

P95 | Quantifying the mitochondrial content with diffusion MRI
Nicolas Moutal, Denis Grebenkov, Sylvie Clerjon, Guilhem Pages, Jean-Marie Bonny

P96 | Method improvements for diffusion tensor imaging of turbulent fluids
Amy-Rae Gauthier, Noah Stocek, Ben Newling

P97 | How MRI can assist Rheology?
Maude Ferrari, Mathieu Jenny, Sebastien Kiesgen De Richter, Sébastien Leclerc, Christel Métivier, Xiao Zhang, Philippe Coussot

P98 | Flow imaging in a model fractured porous media at low magnetic field
Marc Fleury, Nicolas Gland

P99 | MRI flow cell development to monitor in-situ and in-real time dissolution of porous food products
Gjw Goudappel, Theo Blijdenstein, Adrian Voda

P100 | New spatial encoding strategy for systems with ultra-short transverse relaxation times
Vincent Sarou-Kanian

P101 | 3D Imaging of flow pattern in soil – plant systems
Sabina Haber- Pohlmeier, Jie Wang, Andreas Pohlmeier, Petrik Galvosas

P102 | MR signal for powdered specimens
Magnus Herberthson, Cem Yolcu, Hans Knutsson, Carl-Fredrik Westin, Evren Özarslan

P103 | Characterization of Anomalous Jet and Bubble Interaction in a Fluidized Bed
Chris Boyce, Alexander Penn, Maxim Lehnert, Klaas Pruessmann, Christoph Müller

P104 | Monitoring slow motion in porous media using 3D propagator mapping
Jie Wang, Sabina Haber- Pohlmeier, Andreas Pohlmeier, Kira Pitman, Martin Markwitz, Audrey Chan, Petrik Galvosas

P105 | The limits of flow detection with PGSE MRI
N. H. Williamson, M. E. Komlosh, D. Benjamini, P. J. Basser

P106 | Phase-Encoded MRI: A Valuable Tool for Sediment Characterization and Process Monitoring
B. Zhao, W. Cha, J.C. Santamarina

P107 | Ultrafast diffusion exchange measurement
Otto Mankinen, Vladimir Zhivonitko, Anne Selent, Susanna Ahola and Ville-Veikko Telkki

LIST OF PARTICIPANTS

LIST OF PARTICIPANTS *(as per 4th of July 2019)*

- **Afrough Armin**, Technical University of Denmark, DENMARK
- **Alia Alia**, Leiden Institute of Chemistry, Leiden University, NETHERLANDS
- **Appel Matthias**, Shell Global Solutions, NETHERLANDS
- **Badea Alexandra**, Duke University Medical Center, USA
- **Balbierer Roland**, Karlsruhe Institute of Technology, GERMANY
- **Balcom Bruce**, University of New Brunswick, CANADA
- **Bardin Solène,** NeuroSpin/CEA-Saclay, FRANCE
- **Basser Peter**, NIH/NICHD, USA
- **Behr Volker**, University of Würzburg, GERMANY
- **Benjamini Dan**, Center for Neuroscience & Regenerative Medicine, NIH/USUHS, USA
- **Bentouaf Ali**, Dr. Mouay Tahar University of Saida, ALGERIA
- **Bernin Diana**, Chalmers University of Technology, SWEDEN
- **Berthault Patrick**, CEA, FRANCE
- **Beyea Steven**, Dalhousie University, CANADA
- **Blümich Bernhard**, RWTH Aachen University, GERMANY
- **Bnaiahu Natalie**, Tel Aviv University, ISRAEL
- **Bonny Jean-Marie,** INRA - Unité QuaPA, FRANCE
- **Borg Raymond**, UC Santa Barbara, USA
- **Boumezbeur Fawzi**, NeuroSpin/CEA-Saclay, FRANCE
- **Boutin Céline**, CEA, FRANCE
- **Boyce Christopher**, Columbia University, USA
- **Britton Melanie**, University of Birmingham, UK
- **Budker Dmitry**, Helmholtz Institute Mainz and UC Berkeley, GERMANY
- **Carret Guillaume**, CortecNet, FRANCE
- **Cimmarusti Gabriele Michele**, University of Birmingham, UK
- **Ciobanu Luisa**, NeuroSpin/CEA-Saclay, FRANCE
- **Codd Sarah**, Montana State University, USA
- **Cremillieux Yannick**, ISM-Université de Bordeaux, FRANCE
- **Cui Yingzhi**, UNSW, AUSTRALIA
- **de Almeida Martins João Pedro**, Lund University, SWEDEN
- **de Kort Daan**, University of Cambridge, UK
- **de Oliveira Silva Rodrigo**, KU Leuven, BELGIUM
- **Doswell Claire**, University of Birmingham, UK
- **Dubois Marc**, Institut Fresnel, CRMBM, AMU, FRANCE
- **Duckett Simon**, University of York, USA
- **Dykstra Cameron**, Resonint Limited, NEW ZEALAND
- **Dykstra Robin**, Victoria University of Wellington, NEW ZEALAND
- **Faber Cornelius**, University Hospital Muenster, GERMANY

- **Fabich Hilary**, ABQMR Inc., USA
- **Ferrari Maude**, Université de Lorraine, FRANCE
- **Fleury Marc,** IFP Energies Nouvelles, FRANCE
- **Fournet Gabrielle**, Boost.rs, FRANCE
- **Fricke Sophia**, University of California Davis, USA
- **Fukushima Eiichi**, ABQMR, USA
- **Galvosas Petrik,** Victoria University of Wellington, NEW ZEALAND
- **Gao Yang**, China University of Petroleum-Beijing, China
- **Gauthier Amy-Rae**, University of New Brunswick, CANADA
- **Glöggler Stefan**, MPI for Biophysical Chemistry, GERMANY
- **Goudappel Gert-Jan**, Unilever, NETHERLANDS
- **Grebenkov Denis**, CNRS - Ecole Polytechnique, FRANCE
- **Green Derrick**, Green Imaging Technology, CANADA
- **Haber-Pohlmeier Sabina**, RWTH Aachen University, GERMANY
- **Halse Meghan**, University of York, UK
- **Han Songi**, University of California Santa Barbara, USA
- **Hashem Eeza Muhamed Nour**, Leipzig University, GERMANY
- **He Yucheng,** Chongqing magnetway electronic technology co. LTD, CHINA
- **Herberthson Magnus**, Linköping University, SWEDEN
- **Hill-Casey Fraser**, University of York, UK
- **Holmes William**, University of Glasgow, UK
- **Hoult David**, David Hoult Consulting Ltd., CANADA
- **Huang Shaoying**, Singapore University of Technology and Design, SINGAPORE
- **Hürlimann Martin**, Schlumberger, USA
- **Jiang Hong**, Physical Chemistry of Lund University, SWEDEN
- **Johns Michael**, University of Western Australia, AUSTRALIA
- **Karlsons Kaspars**, University of Cambridge, UK
- **Kind Jonas**, Technische Universität Darmstadt, GERMANY
- **Komlosh Michal**, HJF/NIH, USA
- **Krug Julia R.**, Wageningen University & Research, NETHERLANDS
- **Kuethe Dean**, ABQMR, USA
- **Kulesz Karolina**, CERN, SWITZERLAND
- **Küppers Markus**, RWTH Aachen University, GERMANY
- **Lambers Henriette**, University Hospital Muenster, GERMANY
- **Lee Seul Ki**, St. Vincent s Hospital, SOUTH KOREA
- **Leforestier Rodolphe**, IRSTEA, FRANCE
- **Lehmann Volker**, Bruker BioSpin GmbH, GERMANY
- **Li Rupeng**, University of New South Wales, AUSTRALIA
- **Liang Xiao**, China University of Geosciences Beijing, CHINA

- **Liu Huabing**, Beijing Limecho Ltd., CHINA
- **Lu Bing**, NIUMAG, CHINA
- **Ludwig Dominik**, German Cancer Research Center DKFZ, GERMANY
- **Luo Sihui**, China University of Petroleum-Beijing, CHINA
- **Madelin Guillaume**, New York University, USA
- **Mailhiot Sarah**, University of Oulu, FINLAND
- **Maneval James**, Bucknell University, USA
- **Mankinen Otto**, NMR Research Unit University of Oulu, FINLAND
- **Marhabaie Sina**, ENS, FRANCE
- **Mastikhin Igor**, University of New Brunswick, CANADA
- **McCarney Evan**, Korimako Chemical Ltd., NEW ZEALAND
- **McDowell Andrew**, NuevoMR LLC, USA
- **Mohoric Ales**, University of Ljubljana Faculty of Mathematics and Physics, SLOVENIA
- **Moussu Marine**, Multiwave Innovation, FRANCE
- **Moutal Nicolas**, CNRS - Ecole Polytechnique, FRANCE
- **Mouton Laura**, NeuroSpin/CEA Saclay, FRANCE
- **Navon Gil,** Tel Aviv University, ISRAEL
- **Nelson Madison**, Montana State University, USA
- **Nestle Nikolaus**, BASF SE, GERMANY
- **Nevo Uri**, Tel Aviv University, ISRAEL
- **Newling Ben**, University of New Brunswick, CANADA
- **Nikulin Anton**, PSL CNRS ESPCI, FRANCE
- **O'Reilly Thomas**, C.J. Gorter, Center for High Field MRI, LUMC, NETHERLANDS
- **Oerther Thomas**, Bruker BioSpin, GERMANY
- **Özarslan Evren**, Linköping University, SWEDEN
- **Panattoni Francesco**, University of Cambridge, UK
- **Pavlovskaya Galina**, University of Nottingham, UK
- **Penn Alexander**, ETH Zurich, SWITZERLAND
- **Petiet Alexandra**, ICM, FRANCE
- **Pohlmeier Andreas**, Research Center Jülich, GERMANY
- **Quettier Lionel**, CEA, FRANCE
- **Reymbaut Alexis**, Lund University, SWEDEN
- **Rodin Victor**, University of Glasgow, UK
- **Rongsheng Lu**, Southeast University, CHINA
- **Sakellariou Dimitris**, KU Leuven, BELGIUM
- **Salager Elodie**, CNRS, FRANCE
- **Sarou-Kanian** Vincent, CNRS, FRANCE
- **Sawvel April**, Lawrence Livermore National Laboratory, USA
- **Scheler Ulrich**, Leibniz Institute for Polymer Research, GERMANY

- **Schork Nicolas**, KIT, GERMANY
- **Schuhmann Sebastian**, KIT, GERMANY
- **Sederman Andy,** University of Cambridge, UK
- **Seland John**, University of Bergen, NORWAY
- **Serial Maria Raquel**, Wageningen University & Research, NETHERLANDS
- **Sersa Igor**, Jozef Stefan Institute, SLOVENIA
- **Seymour Joseph**, Montana State University, USA
- **Skuntz Matthew**, Montana State University, USA
- **Song Yiqiao**, Schlumberger-Doll Research, USA
- **Stapf Siegfried**, TU Ilmenau, GERMANY
- **Sun Boqin,** Chevron Inc., USA
- **Svyatova Alexandra**, International Tomography Center, RUSSIA
- **Terenzi Camilla**, Wageningen University, NETHERLANDS
- **Thompson Emma**, BASF, GERMANY
- **Thrane Linn**, Lund University, SWEDEN
- **Utsuzawa Shin**, Schlumberger-Doll Research, USA
- **Van As Henk**, Wageningen University, NETHERLANDS
- **Vanduffel Hanne**, KU Leuven, BELGIUM
- **Vogel Patrick,** University of Würzburg, GERMANY
- **Wald Lawrence**, Massachusetts General Hospital, USA
- **Walton Jeffrey**, University of California, USA
- **Wang Jie**, Victoria University of Wellington, NEW ZEALAND
- **Wang Junnan**, Southeast University, CHINA
- **Washburn Kathryn**, Nofima, NORWAY
- **Westrick Nicole**, Procter & Gamble Co., USA
- **Wilczynski Ella**, Tel Aviv University, ISRAEL
- **Williamson Nathan**, NIH, USA
- **Witherspoon Valencia**, NIH/NICHD, USA
- **Wu Baosong**, Yale University, USA
- **Wu Zhengxiu**, Southeast University, CHINA
- **Xia Yang**, Oakland University, USA
- **Xiao Dan**, University of Windsor, CANADA
- **Xu Yajie**, SIBET, CHINA
- **Yang Qing**, Southeast University, CHINA
- **Yon Maxime**, Weizmann Institut of Science, ISRAEL
- **Zamiri Mohammad Sadegh**, University of New Brunswick, CANADA
- **Zhang Yingli**, Niumag Corporation, CHINA
- **Zhen John**, University of Western Australia, AUSTRALIA
- **Zick Klaus**, Bruker BioSpin, GERMANY